Juggled Interferometer for Gravitational Wave Detection

（重力波検出のためのジャグリング干渉計の開発）

Bin Wu

Supervisor: Prof. Seiji Kawamura

Department of Physics
Nagoya University

This dissertation is submitted for the degree of
Doctor of Philosophy

Nagoya University September 2023

I would like to dedicate this thesis to my loving parents.

Declaration

I hereby declare that except where specific reference is made to the work of others, the contents of this dissertation are original and have not been submitted in whole or in part for consideration for any other degree or qualification in this, or any other university. This dissertation is my own work and contains nothing which is the outcome of work done in collaboration with others, except as specified in the text and Acknowledgements.

Bin Wu
September 2023

Acknowledgements

During my time at Nagoya University, I have been blessed with countless invaluable experiences, and it is all thanks to the unwavering support and encouragement of the people around me.

First and foremost, I am sincerely grateful to my supervisor, Professor Kawamura. To have crossed paths with such an exceptional teacher is a great luck for me. Not only has he provided me with immense academic guidance, but he has also shown genuine care for my personal well-being, akin to that of a caring elder. His passion for research and insatiable curiosity have deeply touched me, inspiring me to relish the process of exploration and discovery.

I extend my heartfelt appreciation to my fellow labmates: Yamada-san, Watanabe-san, Ishikawa-kun, Iwaguchi-kun, Shimizu-kun, Kawasaki-kun, Umemura-san, and Tsuji-kun. Working and learning alongside them has been an absolute delight. I am grateful for the lively discussions during group meetings and their patience in listening to my broken Japanese. I would like to give special thanks to Ishikawa-kun, who gave invaluable ideas on the data readout method. A special mention also goes to Shimizu-kun and Umemura-san and Iwaguchi-kun, whose joint efforts in the experiment have been invaluable.

My sincere thanks go to Nishimura-san, Kobayashi-san, and the other dedicated staff members in Technical Center of Nagoya University. Their exceptional efficiency and commitment have significantly contributed to my experiments.

I would like to thank my co-authors, Dr. Yokoyama and Dr. Michimura. Their insightful feedback and meticulous revisions have imparted invaluable knowledge and skills to me. Especially, I learned a lot about the theory of primordial black holes from Dr. Yokoyama and got quite useful comments from Dr. Michimura about the experiment design.

I also wish to express my gratitude to the other teachers and students in the Uxg Laboratory. The atmosphere within the lab brims with vitality, and I will forever cherish the memories of those “Omiyage” on the desk in our office. Nakazawa-sensei and Mitsuishi-sensei have not only provided invaluable comments and suggestions on my research, but they have also been warmhearted and approachable in our daily interactions.

I am grateful to the teachers and senior colleagues at Beijing Normal University, who have generously extended their guidance and support in my academic pursuits.

I want to express my love and thanks to Natsu-san, my first and best Japanese friend. Her boundless warmth and infectious cheerfulness have brought immense solace and joy to my life.

To my dear friends in the SONOYAMA community, I cannot thank you enough. It is through your presence and support that my life in Japan has been illuminated with countless cherished memories and shared laughter.

I want to extend my thanks to my friends in China, despite the distance that separates us. Your care, constant presence, and shared experiences have bridged the gap and made me feel cherished, even amidst the prolonged absence from my homeland.

In closing, I reserve my deepest appreciation for my beloved family. Their love and support have been the cornerstone of my journey. Without their presence and encouragement, none of my achievements would have been possible.

Abstract

The successful detection of gravitational waves has opened a new window for mankind to explore the universe. From the perturbations at the early universe to the orbiting of dense celestial bodies, a multitude of cosmic phenomena are all transmitting information about the universe via gravitational waves. The current earth-based interferometric gravitational wave detectors have a limited sensitivities at frequencies below $\sim$10 Hz due to seismic noise and suspension thermal noise, which are caused by the ground vibrations and the isolation system. To mitigate these two sources of noise is the key to improving the sensitivity of gravitational wave detection on earth.

Juggled Interferometer (JIFO) is a novel type of gravitational wave detector, which implements repeatedly free-falling test masses (mirrors). During the free-falling cycles, the mirrors are totally decoupled from the ground and there is no seismic noise or suspension thermal noise anymore.

This thesis presents the first detailed analysis of the data features of JIFO and develops a data readout and analysis method based on the data features. This method can obtain the mirror displacement signal of the interferometer without fringe locking and provides a stable Signal-to-Noise Ratio (SNR) regardless of the interference fringes. By evaluating the sensitivity curve of JIFO, promising science cases of a JIFO is studied, which include detecting quasi-normal modes of massive black holes, testing Brans-Dicke theory with black hole-neutron star binaries, and detecting gravitational waves originating from density fluctuations in the early stage of the universe, which provide a hint for the primordial black hole – dark matter scenario. These detections would not be possible on earth without the implementation of free-falling masses, which is the primary difference of JIFO from the other earth-based interferometric gravitational wave detectors.

Based on the concept of a "free-falling mirror", a prototype of JIFO was designed and built from scratch in a pioneering manner. Due to the uniqueness of this experiment, many devices were specifically designed, including but not limited to the linear stage used to realize the mirror release, the mirror holder capable of automatic realignment, and the vacuum tank which is made of acrylic for its transparency and low density. This experiment has achieved the mirror release successfully and maintained the stability to some extent. The disturbances of the prototype are characterized, and possible solutions are discussed, laying the foundation for future experiments.

Table of contents

List of figures xv

List of tables xix

1 Introduction 1

1.1 The theory of gravitational waves . . . 1

1.1.1 Einstein's prediction . . . 1

1.1.2 The scale of gravitational waves . . . 2

1.2 Gravitational wave sources and detection . . . 4

1.2.1 Gravitational wave sources . . . 4

1.2.2 The methods of gravitational wave detection . . . 5

1.2.3 Observations of gravitational waves . . . 6

1.3 Sensitivity limit of interferometric earth-based gravitational wave detectors 8

1.3.1 Current gravitational wave detectors . . . 8

1.3.2 Various noises of gravitational wave detection on earth . . . 9

1.3.3 Noises dominant at lower frequencies . . . 11

1.4 Methods to improve the sensitivity of a gravitational wave detector . . . 12

1.4.1 Upgrade the interferometric gravitational wave detector . . . 12

1.4.2 Novel type of interferometer . . . 12

2 Concept and characteristics of a Juggled Interferometer (JIFO) 15

2.1 Basic configuration . . . 15

2.1.1 Motivation . . . 15

2.1.2 JIFO compared with a standard gravitational wave detector . . . 17

2.2 Data features . . . 19

2.2.1 Discontinuous data . . . 19

2.2.2 Initial effect and its detrending . . . 19

2.3 Data readout method . . . 22

2.3.1 Mirror displacement signal from an interferometer 22
2.3.2 Pre-modulation 24
2.3.3 Phase reconstruction 25
2.3.4 Analog-to-digital conversion of JIFO readout 29
2.4 Effects of cyclic movement 30
2.4.1 Additional Newtonian noise 30
2.4.2 Signal upconversion 36

3 Promising science cases of a Juggled Interferometer (JIFO) 37
3.1 Sensitivity improvement of a JIFO compared with ET 37
3.2 Promising science cases 39
3.2.1 Detecting Quasi-normal modes of massive black holes 39
3.2.2 Testing Brans-Dicke theory 42
3.2.3 Primordial black holes research 45

4 Principle verification experiment 49
4.1 Overview of the experiment 49
4.2 Optical setup 51
4.2.1 Fiber coupling 51
4.2.2 Tilted end mirror 52
4.3 Free-falling system 53
4.3.1 Mirror tilt upper limit 53
4.3.2 Mirror holder design and test 57
4.3.3 Linear stage for mirror free falling 59
4.4 Details of other devices 62
4.4.1 Vacuum tank 62
4.4.2 Quadrant photon detectors 65

5 Main results and possible solutions for the disturbances 71
5.1 Linear stage movement 71
5.2 Mirror release 73
5.2.1 Mid-release method 73
5.2.2 Top-release method 74
5.3 Device performance characterizing 75
5.3.1 Testing without free-falling mirrors 75
5.3.2 Detecting transmitted and reflected light from a beam splitter 76
5.3.3 Vacuum level and mirror release 78

5.4 Main disturbances and possible solutions 78
  5.4.1 Linear stage vibration 81
  5.4.2 Mirror movement caused by release 82

6 Conclusions and future works **87**
6.1 Conclusions 87
6.2 Future works 89

References **91**

List of figures

1.1 Plus (h_+) and cross ($h_\times$) modes of gravitational waves 3
1.2 Scheme of a laser interferometric gravitational wave detector 6
1.3 Gravitational wave events 7
1.4 Worldwide network of earth-based gravitational wave detectors 8
1.5 Sensitivity of gravitational wave detectors and sources 9
1.6 Design noise level for Advanced LIGO 10
1.7 Quadruple-pendulum system to shield test masses from vibrations 11

2.1 Conceptual design of Einstein Telescope 16
2.2 Noise sources of ETLF (Einstein Telescope Low Frequency) 17
2.3 Conceptual design of a Juggled Interferometer (JIFO) 18
2.4 Mirror movement process of JIFO 18
2.5 Discontinuous data from JIFO before and after detrending 20
2.6 Gaussian noise after detrending 21
2.7 Michelson interferometer with and without laser modulation 23
2.8 Interfered intensity and modulation-demodulation signal changing with phase difference of two beams 23
2.9 Pre-modulated interferometer 26
2.10 Phase unwrapping from tangent $\phi(t)$ 27
2.11 Updated interferometer with two PD signals 28
2.12 Gravity force from the ceiling to the mirror 31
2.13 Mirror displacement data resulting from a resting mass 32
2.14 Mirror displacement spectrum peaks at 1 Hz and its harmonics 33
2.15 Spectrum of the Newtonian noise resulting from a range of masses at different distances 34
2.16 Mirror and a moving mass around 34
2.17 Mirror displacement spectrum resulting from a moving source around . . . 35
2.18 Two mirrors and a moving mass around 36

3.1 Sensitivity curves and main noise sources of ET and JIFO 38
3.2 Example of ringdown oscillation 40
3.3 Process of binary black holes merger 41
3.4 Central frequency of the Quasi-normal modes of black holes as a function mass 42
3.5 Quasi-normal modes for massive black holes and the sensitivity curves for ET and JIFO 43
3.6 Gravitational wave strain from NS-BH binaries and the sensitivity curves for ET and JIFO 44
3.7 Strain of PBH GW peaking at 1 Hz, together with the sensitivity curves of ET and JIFO with a one-year correlation 47

4.1 Overview of the experiment setup 50
4.2 Laser beam coupling into a fiber 51
4.3 Fiber connector and fiber 52
4.4 Interferometer with tilted end mirrors 53
4.5 Requirement on the mirror tilt to maintain interference 54
4.6 Interference of two tilted beams around the bright fringe 55
4.7 Interference intensity change as the arm length of the interferometer changes 56
4.8 Interference contrast changing with the mirror tilt 56
4.9 Mirror holder 57
4.10 Three sizes of mirror holders 58
4.11 Testing the stability of the mirror holder 59
4.12 Probability distribution plot of the beam spot positions 60
4.13 Three candidate materials for the mirror base 61
4.14 One cycle movement of the linear stage and the mirror 62
4.15 Illustration of the forces exerted on a mirror by air molecules 63
4.16 Residual gas noise under the Fluctuation-Dissipation Theorem 64
4.17 Vacuum tank and the platform 65
4.18 Operating circuit for QPD 67
4.19 Laser intensity spectrum measured with the four segments of the QPD . . . 68
4.20 Unidentified spikes from the QPD outputs 69

5.1 Linear stage trial run result 72
5.2 Target movement of the *mid-release* method for the mirror and linear stage to realize mirror free falling 73
5.3 Obvious tilt of the mirror using the *mid-release* method 73

5.4 Target movement of the *top-release* method for the mirror and linear stage to realize mirror free falling 74
5.5 Successfully released the mirrors with no obvious tilt using the *top-release* method 74
5.6 Directly incident laser beam on the QPD 76
5.7 Ringdown of the QPD output 77
5.8 Detecting transmitted and reflected light from a beam splitter 79
5.9 Reflected light intensity for each segment of the QPD as the linear stage moves 80
5.10 Variation of reflected light with the movement of the linear stage under different pressure conditions 80
5.11 Laser power fluctuation when linear stage is moving 81
5.12 Five QPDs used to obtain mirror tilt information 83
5.13 Tilt beams resulting from mirror tilt 83
5.14 Fringe intensity and modulation-demodulation signal changing with phase . 84

List of tables

3.1 ω_{BD} constraint results from different detectors 45

4.1 Standard deviations of beam spot position for different mirror holder sizes . 58
4.2 Standard deviations of beam spot position for different materials 59
4.3 Some designed parameters of the linear stage 61

5.1 Extraction of mirror tilt signal from QPD signals 85

Chapter 1

Introduction

More than 100 years ago, the existence of gravitational waves was predicted by Albert Einstein [1]. After generations of efforts, people finally succeeded in detecting them in 2015 [2], a century after Einstein's prediction. The direct detection of gravitational waves is an epoch-making achievement in astronomical observation, opening a new window for us human-beings to "see", or, to be more precise, "listen to", the universe, since the frequencies of the detected gravitational waves fell right in the range of human hearing. By analyzing the information carried by various gravitational waves passing through the Earth, we may have the chance to reveal the nature of gravity, the nature of dark matter, and the equation of state of dense celestial bodies and many other unknowns about the universe [3].

In this chapter, the importance of gravitational wave detection and the motivation of this thesis will be reflected. Firstly, the theory of gravitational waves will be briefly introduced in Sec. 1.1, then the detection of gravitational waves will be introduced in Sec. 1.2. This will be followed by some details about the sensitivity of the current gravitational wave detectors in Sec. 1.3 and the methods to improve detection sensitivity in Sec. 1.4.

1.1 The theory of gravitational waves

1.1.1 Einstein's prediction

Gravitational wave is one of the most important predictions of General Relativity [1]. The equation governing gravitational waves can be derived from Einstein field equations, where gravity is considered as a geometric effect and the curvature of spacetime depends on the local energy-stress tensor $T_{\mu\nu}$ [4, 5]:

$$G_{\mu\nu} = \frac{8\pi G}{c^4} T_{\mu\nu}, \tag{1.1}$$

where G is the Newton's gravitational constant and c is the speed of light in vacuum. $G_{\mu\nu}$ is the Einstein tensor showing the geometric features of the spacetime:

$$G_{\mu\nu} = R_{\mu\nu} - \frac{1}{2} g_{\mu\nu} R, \tag{1.2}$$

where $R_{\mu\nu}$ is the Ricci tensor, $g_{\mu\nu}$ is the metric tensor of spacetime and R is the curvature scalar. Considering the weak-field and linear approximation, the metric tensor of spacetime can be considered as the Minkowski metric ($\eta_{\mu\nu}$) with a small perturbation ($h_{\mu\nu}$):

$$g_{\mu\nu} = \eta_{\mu\nu} + h_{\mu\nu}, \;\; h_{\mu\nu} \ll 1, \; h_{\mu\nu} \ll \eta_{\mu\nu}, \tag{1.3}$$

Then we can obtain a wave equation from the Einstein field equations under the Transverse-traceless gauge (TT gauge):

$$(\bigtriangledown^2 \frac{1}{c^2} \frac{\partial^2}{\partial t^2}) h_{\mu\nu} = 0. \tag{1.4}$$

Thus, we find that the perturbation ($h_{\mu\nu}$) introduced in Eq. 1.3 is proved to be a kind of wave, which would propagate through the universe at the speed of light, and this is the gravitational wave predicted by Einstein a century ago. Gravitational waves have two independent modes: the plus mode (h_+) and the cross mode ($h_\times$), indicating two polarization directions that differ by 45 degrees [6].

1.1.2 The scale of gravitational waves

As mentioned in 1.1, the perturbation of the spacetime will propagate through the universe in the form of gravitational waves, then any event that occurs in the universe, as long as it is accompanied by a perturbation in spacetime, will generate gravitational waves. The intensity of gravitational waves is typically represented by a dimensionless parameter h [7]:

$$h = \frac{2\delta L_{gw}}{L}. \tag{1.5}$$

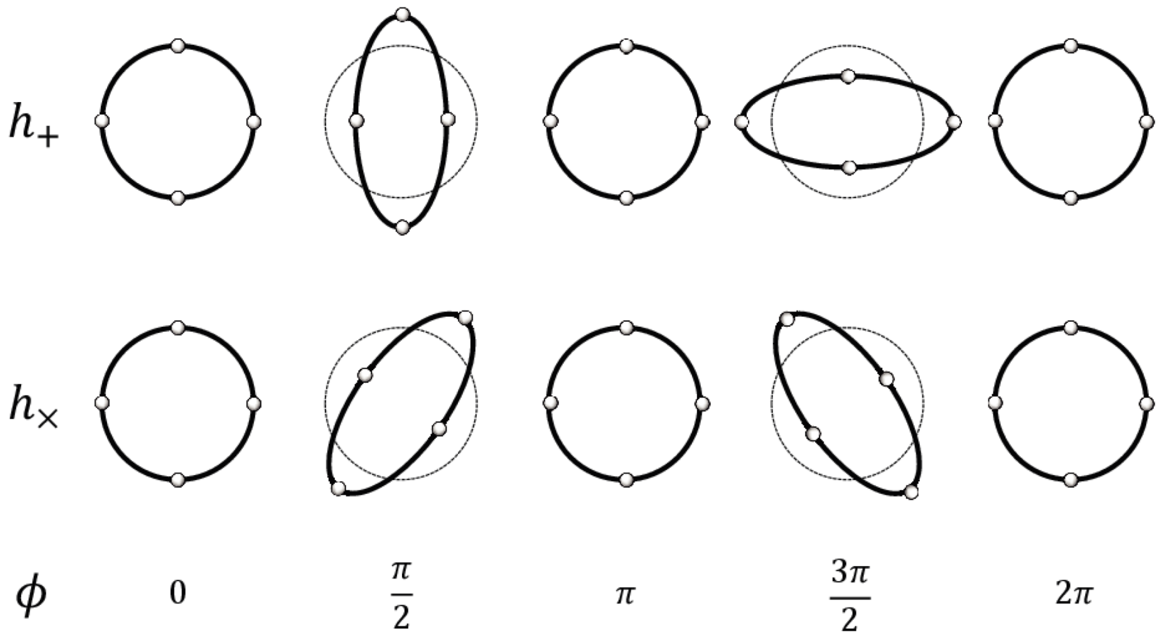

Fig. 1.1 Plus (h_+) and cross ($h_\times$) modes of gravitational waves [6]. The distances between test masses, uniformly distributed on a circle, will be periodically be squeezed or stretched with the arrival of gravitational waves.

where δL_{gw} represents the distance change caused by gravitational waves between two points originally separated by L. Assuming the simplest scenario of gravitational wave generation: two spherical masses with mass M separated by $2r_0$ rotating around their center of mass at a frequency f_{orb}, the dimensionless intensity of gravitational waves emitted by such a system can be expressed as [5] :

$$|h| = \frac{r_{s1} r_{s2}}{r_0 R}. \tag{1.6}$$

where r_{s1} and r_{s2} are the radii of the two spheres, and R is the distance from the source to the observer. In principle, it seems possible to generate and measure gravitational waves in the laboratory. However, in reality, the generated gravitational waves are extremely weak and cannot be detected. For example, two high-density spheres weighing one ton each, rotating at a frequency of 1 kHz and separated by 2 meters, would produce gravitational waves with a strain of only 9×10^{-39}, at a position comparable to its radiation wavelength.

Therefore, to study gravitational waves, we must turn our attention to the universe. Assuming that two neutron stars with masses approximately equal to the Chandrasekhar mass, $M = 1.4 M_\odot \approx 3 \times 10^{30}\,\mathrm{kg}$, and these two stars are very close to each other, e.g., $r_0 = 20\,\mathrm{km}$, with a rotation frequency of $f_{orb} \approx 400\,\mathrm{Hz}$, and a detector is $R = 15\,\mathrm{Mpc} \approx 4.5 \times 1023\,\mathrm{m}$

away, the dimensionless intensity of the gravitational waves is estimated to be $h \approx 1 \times 10^{-21}$. This is much bigger than what we can obtain in the lab but is still tiny, equivalent to a change of only one-thousandth of an atomic nucleus scale between points separated by several kilometers!

1.2 Gravitational wave sources and detection

1.2.1 Gravitational wave sources

Gravitational sources can be classified into four main categories: continuous, inspirals, burst, and stochastic sources [8].

Continuous sources mainly include the asymmetric rotation of dense celestial bodies, such as pulsars. The typical frequency of continuous sources is normally between 1 Hz and 1 kHz. Due to the influence of a high level of seismic noise, which will be introduced later in this chapter, the detection of gravitational wave signals in a frequency band below 10 Hz mainly relies on the space-based gravitational wave detectors or other cosmology methods.

Inspiral sources are related to the final stages of a binary system when the two objects orbit with each other and coalescence into one. In the process of inspiral, angular momentum is continuously lost and dissipated in the form of gravitational waves and even greater energy is released upon merger. Binary neutron star (BNS) mergers are considered to be one of the most valuable inspiral sources, as this process not only releases gravitational wave signals but also corresponding electromagnetic wave signals.

Burst sources release a significant amount of energy within a short period of time. Supernova explosions are one kind of the most important burst sources, and the gravitational wave signals released during the collapse of dense supernovae can help to study supernova explosion mechanisms and the formation process of compact celestial bodies. The frequency range of burst sources is between several hundred hertz and several kilohertz, which is the primary detection frequency band of current earth-based gravitational wave detectors.

Various gravitational wave sources in the universe overlap with each other, forming stochastic gravitational wave backgrounds. The backgrounds often have a certain amplitude over a broad frequency band. Since binary systems are the most common in the universe, they constitute a part of the stochastic backgrounds for sure. Another important stochastic gravitational wave source comes from the inflation and evolution of the universe, and the primordial gravitational waves are considered to be the most important one among them, which may trace back to 10^{-36} to 10^{-32} seconds after the birth of the universe.

1.2.2 The methods of gravitational wave detection

The first gravitational wave detector was the resonant bar invented by Joseph Weber [9]. When a gravitational wave arrives, the suspended resonant bar will be squeezed in one direction and stretched in the other direction, and the changes in stretching and shrinking vary with the frequency and amplitude of the gravitational waves. When the frequency of the gravitational wave is equal to the natural frequency (or eigenfrequency) of the bar, resonance would be excited. At this point, the sensor installed on the resonant bar may be able to sense and record this mechanical vibration, and this vibration can be converted into gravitational wave signals through subsequent data processing methods.

However, Weber bar did not ultimately succeed in detecting gravitational waves. But the scientists who worked on it accumulated a wealth of theoretical and experimental experience, laying an indelible foundation for the successful detection of gravitational waves afterwards.

As the resonant bar detectors faded out, the development of laser interferometric gravitational wave detectors flourished and became the mainstream for gravitational wave detection [10–12]. A laser interferometric gravitational wave detector is basically a Michelson interferometer, which uses laser interference to measure a small length change. In general, the amplitude of gravitational waves is extremely small and can only cause typical length changes in the interferometer arms on the order of 10^{-19} m for a kilometer-scale interferometer. In order to measure such small length changes, gravitational wave detectors have undergone many modifications and updates based on the standard Michelson interferometer design.

Taking the Laser Interferometer Gravitational wave Observatory (LIGO) as an example [13], the interferometer arms are 4 kilometers long, and each arm is a Fabry-Perot cavity, called an arm cavity. The test masses (cavity mirrors) are suspended, and the laser beam is reflected back and forth between the mirrors of the arm cavities, greatly increasing the effective arm length of the interferometer and resulting in the accumulation and amplification of the small length change caused by gravitational waves. A scheme of a laser interferometric gravitational wave detector is shown in Figure 1.2. Other improvements include, but are not limited to, power recycling and signal extraction technologies, which respectively increase the circulating power inside the cavity and widen the frequency bandwidth of the detection.

In addition to the aforementioned methods, there are several alternative approaches for detecting gravitational waves. Pulsar timing array (PTA) [15] is one such method that analyzes the impact of gravitational waves on the timing of millisecond pulsars. The detectable frequency range of PTAs typically lies within the range of $(10^{-7} \sim 10^{-9})$ Hz, depending on the duration of pulsar period recordings and the sampling rate employed. In order to extend observation durations and enhance sampling rates, the International Pulsar

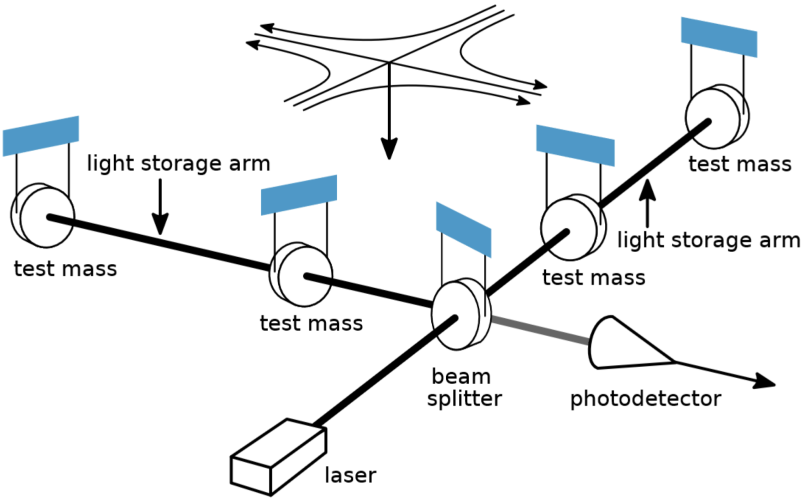

Fig. 1.2 The scheme of a laser interferometric gravitational wave detector [14].

Timing Array (IPTA) [16] initiative has consolidated pulsar timing projects worldwide, with promising prospects for forthcoming discoveries. Moreover, the indirect detection of primordial gravitational waves is believed to be possible by the analysis of the cosmic microwave background (CMB) [17–19], and the pursuit of very high-frequency gravitational waves has prompted the construction of diverse electromagnetic resonance systems by numerous research institutions [20–23].

1.2.3 Observations of gravitational waves

The first indirect evidence of the existence of gravitational waves was discovered through an analysis of the orbital decay of a close binary system named Hulse-Taylor binary pulsar (PSR1913+16) [24]. According to General Relativity, a binary system will lose orbital energy due to gravitational radiation, resulting in a shorter orbital radius and a shorter orbital period. The observation data of PSR1913+16 obtained by J.Taylor and R.Hulse perfectly matched the calculation results from General Relativity. R.Hulse and J.Taylor were awarded the Nobel Prize in Physics in 1993 for their discovery.

The first gravitational wave event was detected directly by LIGO on September 14th, 2015 [2]. This was a binary black hole (BBH) merger event that traveled from 13 billion light years away from the Earth. Two black holes weighing $36^{+5}_{-4}M_{\odot}$ and $29^{+5}_{-4}M_{\odot}$ merged into a Kerr black hole weighing $62^{+4}_{-4}M_{\odot}$, and the remaining $3M_{\odot}$ was radiated in the form of gravitational waves, where $M_{\odot}$ is the solar mass.

After the first detection of BBH gravitational waves, several more BBH gravitational waves were detected, resulting in many objective progresses in black hole research field.

Afterwards in 2017, the gravitational waves from a binary neutron stars (BNS) system, together with its electromagnetic counterparts, were observed [25]. This is a significant milestone for the multi-messenger astronomy since it was the first time that gravitational wave became one of the messengers in an astronomical observation, together with gamma-ray bursts and other electromagnetic waves. The observation of gravitational waves, together with their electromagnetic counterparts, provides a new method to constrain the Hubble constant [26, 27], independent of type Ia supernovae and CMB.

By the end of observation run 3 in 2020, up to 90 gravitational wave events had been detected [8, 28]. It is believed that more and more events will be detected in the near future with the detectors sensitivity keeping improving.

It is also worth mentioning that significant progress has recently been made in the study of gravitational waves using PTA. Research teams from four countries have independently discovered the evidence for a gravitational wave background by analyzing the pulsar timing data [29–32].

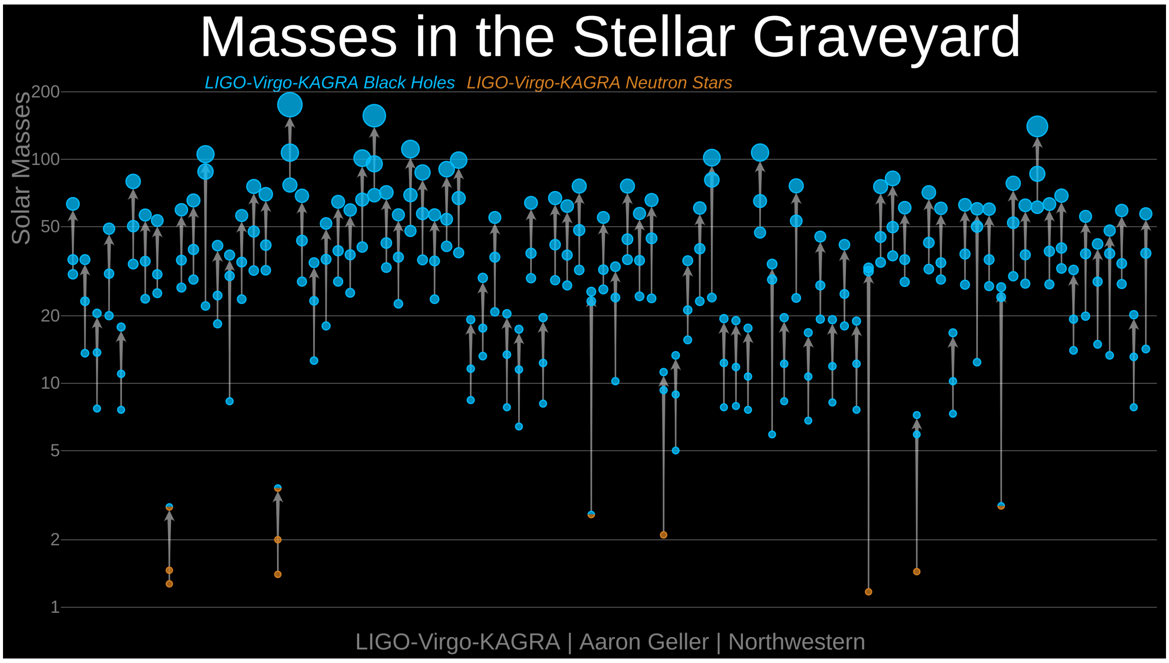

Fig. 1.3 Gravitational wave events [14]. The blue dots represent black holes, and the orange dots represent neutron stars. The mixed half-blue/half-orange dots are compact objects of unclear classification. The vertical scale indicates the mass as a multiple of the solar mass. The arrows show the merger from two objects into one.

1.3 Sensitivity limit of interferometric earth-based gravitational wave detectors

Gravitational wave detection poses a significant challenge due to the inherently small amplitudes. Thanks to the invention of the interferometer, the measurement of minute changes in length became relatively more accessible. Meanwhile, by incorporating sophisticated technologies such as Fabry-Perot cavities, power recycling, and signal recycling, gravitational wave detection entered the realm of scientific reality.

However, despite these remarkable achievements, the sensitivity of current gravitational wave detectors is still limited by an array of noise sources. Consequently, a thorough analysis and rigorous suppression of these noise sources represent paramount endeavors within the field of gravitational wave experiments.

1.3.1 Current gravitational wave detectors

In addition to the 4-kilometer detectors located in the United States (LIGO Livingston and LIGO Hanford), the current earth-based gravitational wave detectors include Virgo [33] in Italy with 3-kilometer-long arms and KAGRA [34] (Large-scale Cryogenic Gravitational wave Telescope) in Japan, also with 3-kilometer-long arms. Meanwhile, there is GEO600 [35] in Germany with an arm length of 600 meter and LIGO-India [36] with almost the same design as LIGO. Figure 1.4 shows a map of the worldwide network of earth-based gravitational wave detectors.

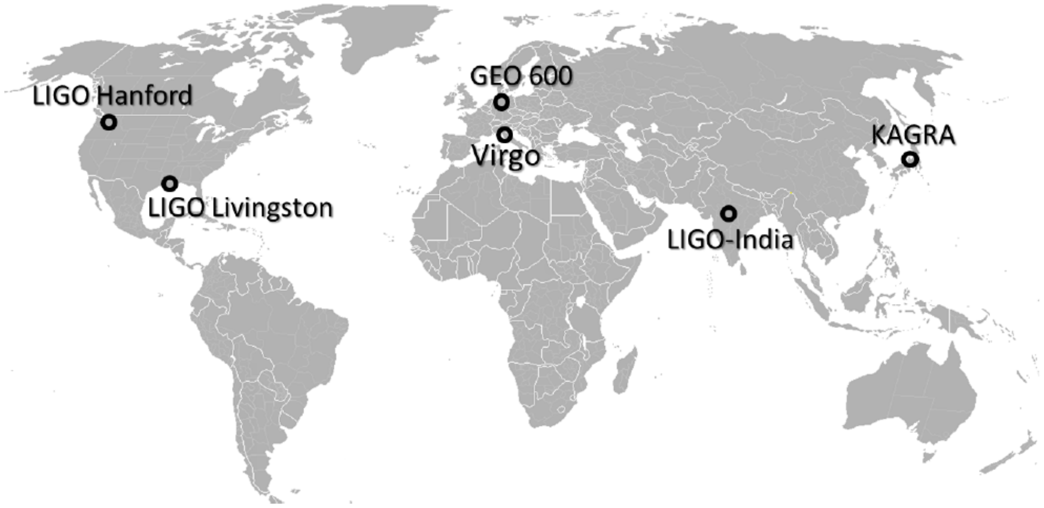

Fig. 1.4 Worldwide network of earth-based gravitational wave detectors [37].

With longer arm length and other improved technologies, the third generation of earth-based gravitational wave detectors such as Einstein Telescope (ET) [38], will increase the sensitivity by an order of magnitude. Furthermore, upcoming space-based laser interferometric gravitational wave detectors, such as LISA [39] (Laser Interferometer Space Antenna) in Europe, DECIGO (Deci-Hertz Interferometer Gravitational wave Observatory) in Japan [40], and *Taiji* [41] and *Tianqin* [42] in China, are expected to detect lower-frequency gravitational wave signals (Deci-Hertz$\sim$ mHz) in the near future. IPTA is in charge of detecting even lower-frequency gravitational waves. Figure 1.5 shows a summary of the gravitational wave detectors and their main target sources.

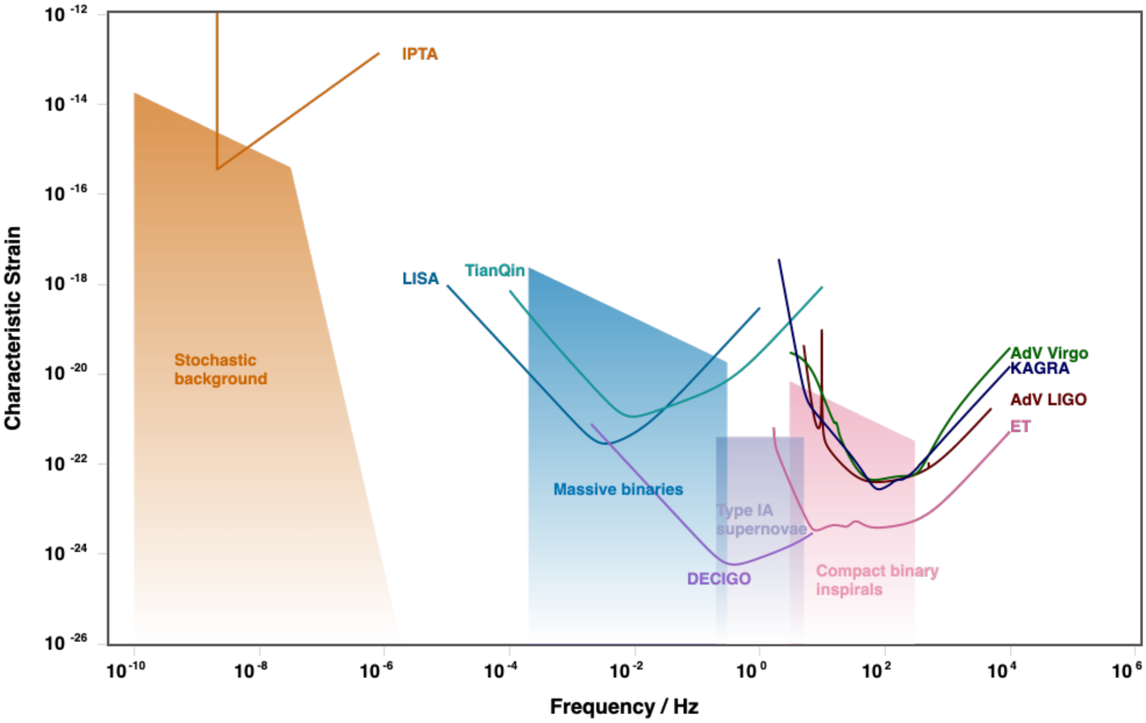

Fig. 1.5 Sensitivity of gravitational wave detectors and sources. This figure is plotted using the method described in ref. [43].

1.3.2 Various noises of gravitational wave detection on earth

There are a variety of noises that we need to be careful about for gravitational wave detection. In order to detect gravitational waves successfully, all these noises have to be comprehensively understand and mitigate to be smaller than the typical strain of gravitational waves.

Take the laser interferometric gravitational wave detector as an example. Anything that can couple to the optical path length change is considered as noise. Figure 1.6 shows the design noise level for Advanced LIGO [13], from which we can gain insights into some of the primary sources of noise in earth-based gravitational wave detectors. Here, the colored lines represent various types of noises, while the black line represents the cumulative sum of these noises. It can be observed that in the frequency range above 12 Hz, the sensitivity limit is primarily determined by quantum noise and coating Brownian noise.

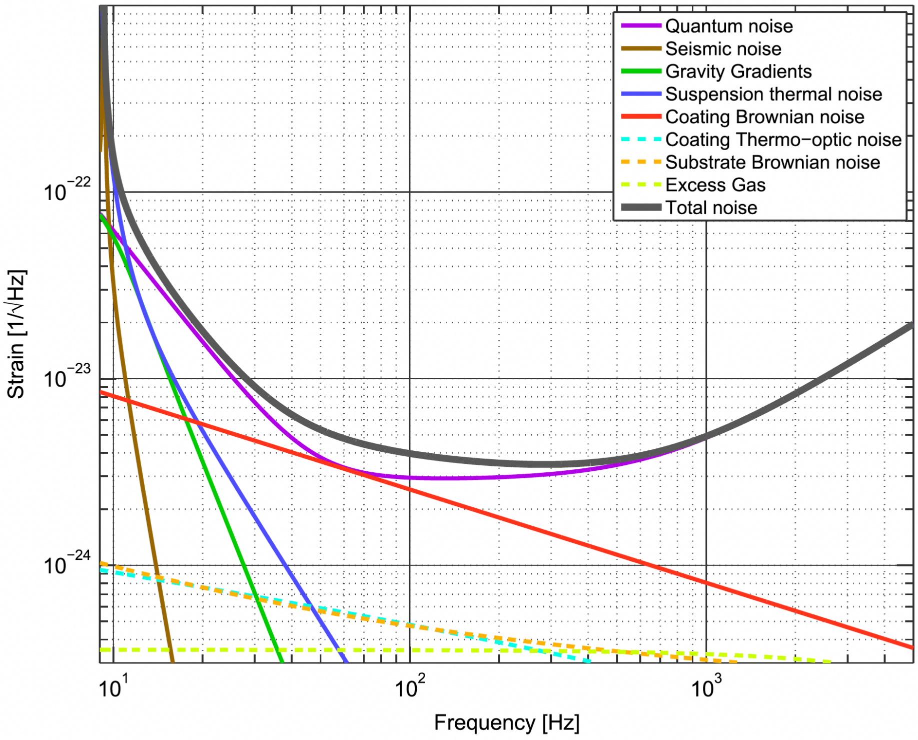

Fig. 1.6 Design noise level for Advanced LIGO.

Quantum noise consists of two components [44, 45]. The low-frequency regime is dominated by radiation pressure noise, originating from fluctuations in the radiation pressure exerted on the test masses. The high-frequency regime is dominated by shot noise, resulting from the uncertainty in the arrival time and quantity of photons at the photodetectors. The laser power inside the detector arms has contrasting effects on these two types of quantum noise: increasing the laser power enhances radiation pressure noise but diminishes shot noise.

Coating Brownian noise, as its name suggests, comes from the Brownian motion of the coating on the mirror surface. It is the most dominant among the noises that are attributed directly to the mirror itself. In the recent experiment in LIGO, the coating Brownian noise exceeds the level of quantum noise around 60 Hz, which means that the mirror coating technology has yet to be improved.

In the frequency range below 10 Hz, seismic noise and suspension thermal noise are notably significant, followed by Newtonian noise.

1.3.3 Noises dominant at lower frequencies

The optimal sensitivity range for the current earth-based interferometric gravitational wave detectors is 10 $\sim$ 1000 Hz. In the frequency range below around 10 Hz, there is a steep slope mainly caused by seismic noise, suspension thermal noise, and Newtonian noise.

Seismic noise originates from natural phenomena and human activities, such as wind, lunar tides, and transportation, among others. Typical ground motion noise is inversely proportional to the square of the frequency, meaning that lower frequencies exhibit more prominent seismic noise.

In order to mitigate the influence of seismic noise, a vibration isolation system is employed to isolate the test masses from the ground vibrations. This isolator uses a quadruple-pendulum to suspend the test masses, see in Figure 1.7. However, this introduces suspension thermal noise unavoidably, which originates from the fibers used to hang the test masses. The Brownian motion in these fibers directly results in the position fluctuations of the test masses, thereby influencing the sensitivity of the detector.

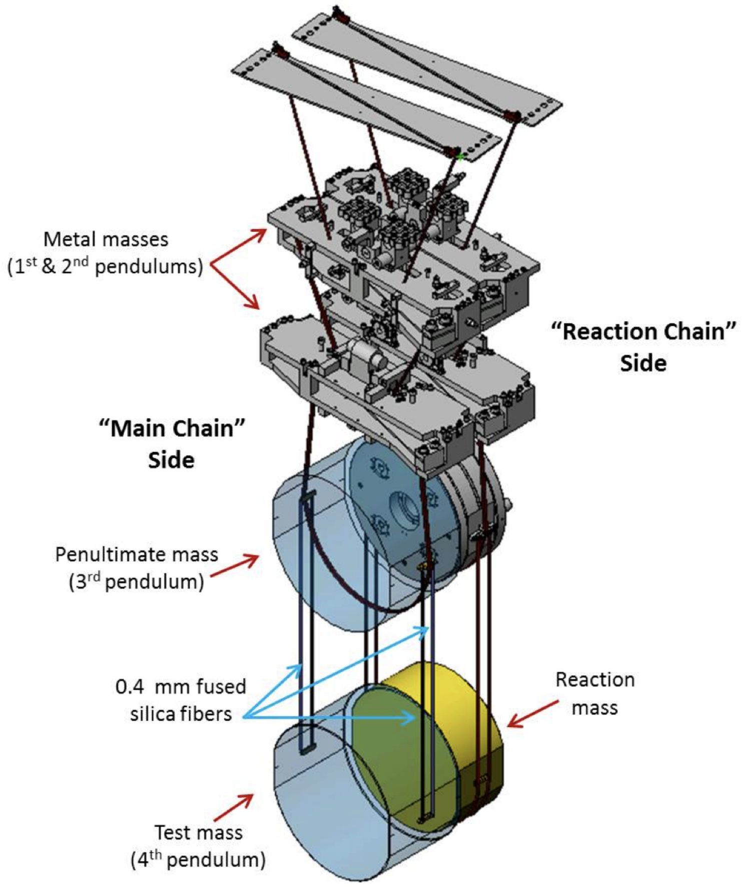
Metal masses
(1st & 2nd pendulums)
"Reaction Chain"
Side
"Main Chain"
Side
Penultimate mass
(3rd pendulum)
0.4 mm fused
silica fibers
Reaction
mass
Test mass
(4th pendulum)

Fig. 1.7 Quadruple-pendulum system to shield test masses from vibrations [14].

Newtonian noise, also known as gravity gradient noise, refers to the fluctuations in the local gravitational field caused by variations in mass distribution around the test masses. These changes in the gravitational field directly impact the motions of test masses, resulting in noise.

1.4 Methods to improve the sensitivity of a gravitational wave detector

1.4.1 Upgrade the interferometric gravitational wave detector

To enhance the sensitivity of laser interferometric gravitational wave detectors, various upgrades have been implemented. In the case of LIGO, sensitivity improvements can be achieved through the following approaches:

1. Increasing laser power to reduce quantum shot noise;
2. Increasing the size and mass of the test masses to reduce the influence of radiation pressure on their motion;
3. Changing the material of the test masses and suspension fibers to reduce thermal noise;
4. Upgrading and improving the isolation systems, such as utilizing active servo control techniques;
5. Employing frequency-dependent squeezing techniques and other methods to reduce quantum noise or even surpass the standard quantum limit (SQL);
6. The other fine-tuning and upgrading different components of the detector are crucial for enhancing sensitivity.

Additionally, the gravitational wave detector KAGRA, located in Kamioka, Japan, is constructed underground and operates in a cryogenic environment. This design helps in reducing seismic noise and thermal noise. Meanwhile, space-based gravitational wave projects and other astronomical observation methods are also important means for improving detection sensitivity and expanding the detection frequency range.

1.4.2 Novel type of interferometer

In addition to the construction and improvement of mainstream laser interferometric gravitational wave detectors, for which high power laser, optical cavities and suspended test masses are essential, researchers are also keeping exploring novel approaches to detect gravitational waves. These novel designs are normally less time-consuming and much cheaper, especially compared with the space projects.

First comes the atom interferometry [46]. In an atom interferometry, atoms are split to travel through two separate free-fall paths and then recombined. The resulting interference pattern contains information about gravitational waves since the travel time of the atoms is changed by the spacetime strain effected by the gravitational waves. Research carried out by the Stanford University has shown that atom interferometry can achieve a sensitivity on the order of $10^{-19}/\sqrt{\mathrm{Hz}}$ in the frequency range of 1∼10 Hz [47].

Another novel type of gravitational wave detector is the torsion bar, which can also achieve sensitivities superior to LIGO around 1 Hz [48]. A torsion bar detector consists of two freely suspended bars that are perpendicular to each other. Gravitational waves passing through the torsion bar induce different torques on the two bars, resulting in relative displacements that are recorded by sensors attached to them. The main noise sources in torsion bar detectors are thermal noise and angular motion of the bars.

In recent years, there has been significant progress in the research of Displacement-Noise-Free Gravitational Wave Detection (DFI) [49, 50]. As the name suggests, DFI is not affected by any displacement noise, which is a key limiting factor for earth-based laser interferometric gravitational wave detectors. By cleverly combining the measured data, DFI eliminates the displacement noise of test masses while preserving the gravitational wave signal. If neutrons are used instead of lasers, DFI's optimal sensitivity range is also below 1 Hz [51].

The focus of this thesis, Juggled Interferometer (JIFO), is also a novel gravitational wave detector, which aims to improve the sensitivity of gravitational wave detection in the low-frequency range. The main characteristic of JIFO is that its test masses are continuously juggled, or in other words, repeatedly released to free fall. This ensures that the test mass is completely free from the seismic noise and suspension thermal noise during the free-falling cycles. This thesis will discuss the design principles and data readout methods of the JIFO in Chapter 2, followed by the target gravitational wave sources in Chapter 3, and the design and progress of prototype experiments in Chapter 4. The main results of the experiment will be summarized in Chapter 5, and the overall conclusion and future works in Chapter 6.

Chapter 2

Concept and characteristics of a Juggled Interferometer (JIFO)

Juggled interferometer (JIFO) is a novel type of gravitational wave detector with repeatedly free-falling mirrors, which can significantly improve the sensitivity of earthbound gravitational wave detectors at lower frequencies. In this chapter, we will start from the introduction of JIFO in Section 2.1, which was firstly proposed by D Friedrich et al [52] in 2014. Then the data features of JIFO will be discussed in Section 2.2. The detrend method suggested by D Friedrich et al [52] will also be introduced here. In Section 2.3, a new data readout method for the interferometer is proposed, making no need of fringe locking for the free-falling mirrors. This is followed by the first analysis of the cyclic movement effects on the output data of a JIFO in Section 2.4, including the additional Newtonian noise and signal upconversion.

2.1 Basic configuration

2.1.1 Motivation

In Chapter 1, it was mentioned that the sensitivity of current earth-based laser interferometric gravitational wave detectors needs to be improved at low frequencies. Here, we take the Einstein Telescope (ET) [38, 53] as an example to illustrate this in more details.

ET is a gravitational wave detection project led by the European Gravitational Observatory (EGO), representing the third generation of detectors following the second-generation detectors such as Advanced LIGO. ET adopts an equilateral triangle configuration, as shown in Figure 2.1. Three detectors are planned to be built within this triangle, represented by different colors in the figure. Each detector is further divided into a high-frequency (HF) and a low-frequency (LF) part based on the difference in sensitivity range. This configuration is referred to as the *xylophone* setup. Operating multiple interferometers simultaneously not only enhances sensitivity but also helps with the polarization determination of gravitational waves. Moreover, ET's design features, such as a 10-kilometer arm length, underground construction, high-power lasers, cryogenics, and squeezed light technology, have significantly improved its target sensitivity compared to the second-generation detectors, as shown in Figure 1.5 in Chapter 1.

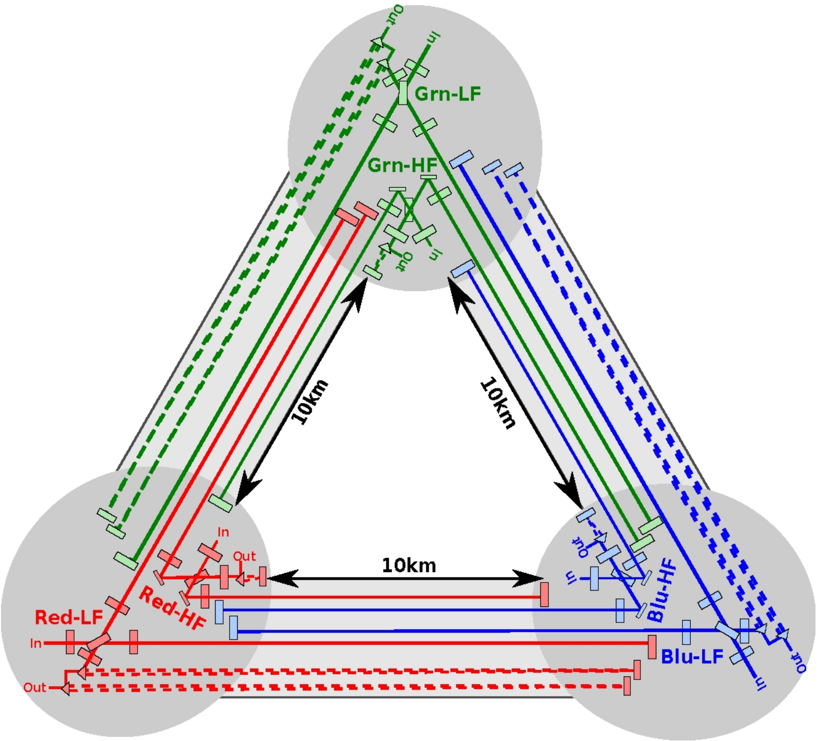

Fig. 2.1 Conceptual design of Einstein Telescope [54].

From Figure 1.5, it can be observed that although the target sensitivity curve of ET has improved significantly compared to the second-generation detectors overall, there is still a steep slope at lower frequencies. Figure 2.2 illustrates the sources causing this steep slope. It is clear that below 2 Hz, seismic noise is significantly greater than the other noises, followed by suspension thermal noise, Newtonian noise, and quantum noise.

Juggled Interferometer (JIFO) aims to eliminate seismic noise at low frequencies, and because suspension thermal noise is introduced by the isolation system designed to handle seismic noise, the removal of seismic noise would also result in the elimination of suspension thermal noise. This would significantly enhance the sensitivity of earth-based laser interferometric gravitational wave detectors in the low-frequency range.

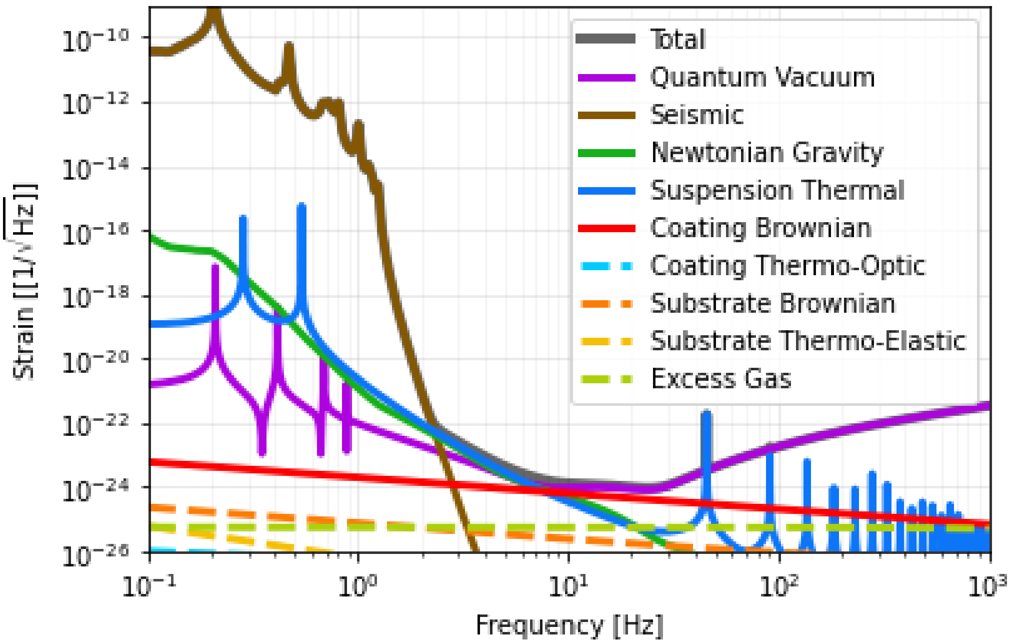

Fig. 2.2 Noise sources of ETLF (Einstein Telescope Low Frequency). The data sources are credited to the ET collaboration.

2.1.2 JIFO compared with a standard gravitational wave detector

As the name suggests, JIFO employs a "juggled" technique on its mirrors. To be more specific, the mirrors are continuously released and go through a free-falling cycle. Since the mirror is released, it is completely free from the influence of the ground and thus decoupled from the seismic noise caused by the ground vibration. Figure 2.3 illustrates a conceptual diagram of JIFO. It is a Michelson-type interferometer, differing from the standard laser interferometric gravitational wave detectors in the following aspects.

The main difference lies in the status of the mirrors during the measurement. In standard earth-based laser interferometric gravitational wave detectors, the mirrors are suspended by fibers and housed within an isolation system. The effects of ground vibrations on the mirrors are mitigated through feedback control of the isolation system and the damping and filtering by multi-stage pendulums. In contrast, JIFO takes a completely different approach by allowing the mirrors to undergo free-falling motion; thus, no isolation system is needed. Due to height limitations, the mirrors cannot remain in a free-falling state all the time. Instead, they undergo a cyclic motion of $acceleration$ - $free falling$ - $deceleration$, as depicted in Figure 2.4. Initially, the mirrors are accelerated to a certain velocity and then released. They subsequently follow a vertical projectile motion (free falling) due to gravity until they return to the released position. Finally, they are decelerated back to zero velocity and return to

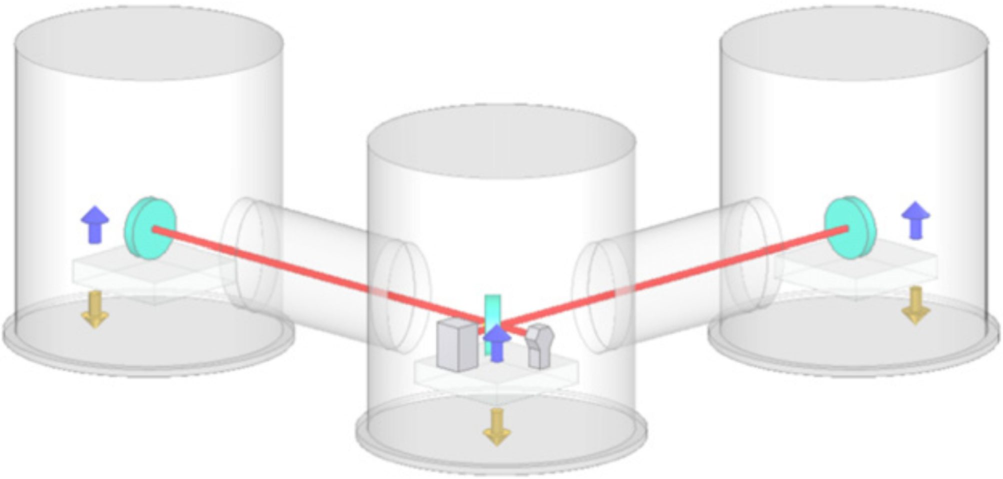

Fig. 2.3 Conceptual design of a Juggled Interferometer (JIFO) [52].

their initial position. The data obtained during the free-falling period is completely free from seismic noise. However, ensuring the safety of the mirrors and maintaining the operation of the interferometer during this motion presents new challenges. Since mirrors in space-based gravitational wave detectors also experience free falling, JIFO can also serve as a test bed for space-based gravitational wave detection projects.

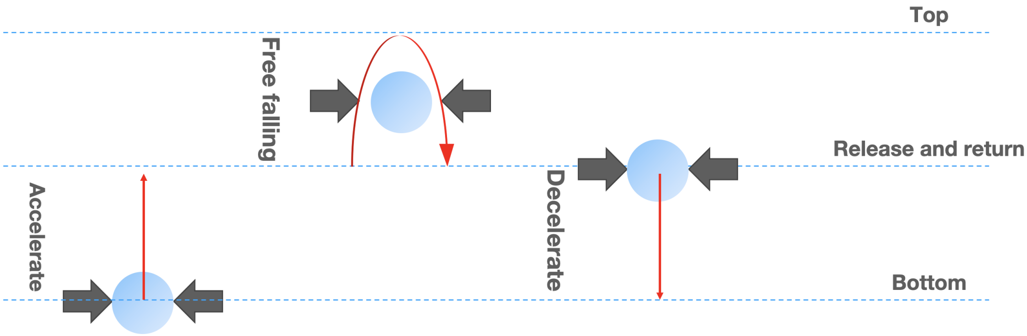

Fig. 2.4 Mirror movement process of JIFO. The mirror is moving vertically and goes through a cyclic *acceleration* - *free falling* - *deceleration* moving process. The arrows here represent the clamps to catch the mirrors to accelerate and decelerate, during the free-falling cycle, the clamps are loosened.

The second difference lies in the absence of the arm cavities in JIFO. The arm cavity is used in the interferometer to accumulate and amplify the changes in the arm length caused by gravitational waves through the back-and-forth reflection of laser light. However, since JIFO focuses on low frequencies where displacement noise dominates, the use of an arm cavity would amplify both the gravitational wave signal and the displacement noise equally. Therefore, the design of arm cavity does not make sense for JIFO.

The third difference lies in the periodic Newtonian noise. For standard earth-based laser interferometric gravitational wave detectors, Newtonian noise originates from fluctuations of masses distributed around the mirrors of the interferometer, leading to variations in the gravitational field. The mirror displacement caused by changing gravitational field is referred to as Newtonian noise. In the case of JIFO, due to the continuous up-and-down motion of the mirrors, Newtonian noise is generated whenever there is an uneven distribution of masses near the mirrors. More details about the Newtonian noise of a JIFO will be discussed in Section 2.4.

2.2 Data features

2.2.1 Discontinuous data

Due to the fact that only during the free-falling motion is the ground vibration noise eliminated, the data obtained during the acceleration and deceleration cycles is invalid. This implies that the effective data recorded by JIFO will be discontinuous. If a burst gravitational wave signal occurs during the acceleration or deceleration cycle of JIFO, it will be missed. For continuous wave sources, the missing data segments directly affect the signal-to-noise ratio (SNR).

When the duration of the effective signal constitutes $1/N$ of the total duration, the match factor decreases to $1/N$ in the matched filtering method [55]. At the same time, since the noise in each data segment is independent, the total noise becomes $1/\sqrt{N}$ times the original and the overall SNR becomes $1/\sqrt{N}$ times the original. If we prepare two JIFOs with staggered ascending and descending motions, the data gaps can be filled, and the lost SNR should be compensated for.

2.2.2 Initial effect and its detrending

The discontinuity of the data brings another issue, which is the variation in the initial effect of each data segment. Here, the initial effect refers to the initial velocity and initial displacement along the arm direction each time the mirror is released. The rotation of the mirror is not considered here, and relevant discussions can be found in Chapter 4. The initial effect reflected in the intensity of the interfered light, which is then converted into a mirror displacement signal $x(t)$. As shown by the blue line in Figure 2.5, the discontinuous displacement noise can be expressed by the equation:

$$x(t) = h(t) + i(t) + n(t), \tag{2.1}$$

where $h(t)$ is the gravitational wave signal, $i(t) = x_0 + v_0 t$ represents the initial effect including the initial displacement x_0 and initial velocity v_0, and $n(t)$ is the noise. Since the initial effect is linear, we can perform linear fitting on the displacement signal and subtract this linear data from the original data to remove the initial effect. This operation is referred to as "detrend". The red line in Figure 2.5 represents the data after detrending. It should be noted that detrending not only removes the influence of the initial effect but also eliminates the linear component of the gravitational wave signal in the data. When the period of the gravitational wave is much smaller than the free-falling cycle time t_c, this influence can be neglected. However, when the period of the gravitational wave is greater than t_c, the signal will be significantly attenuated.

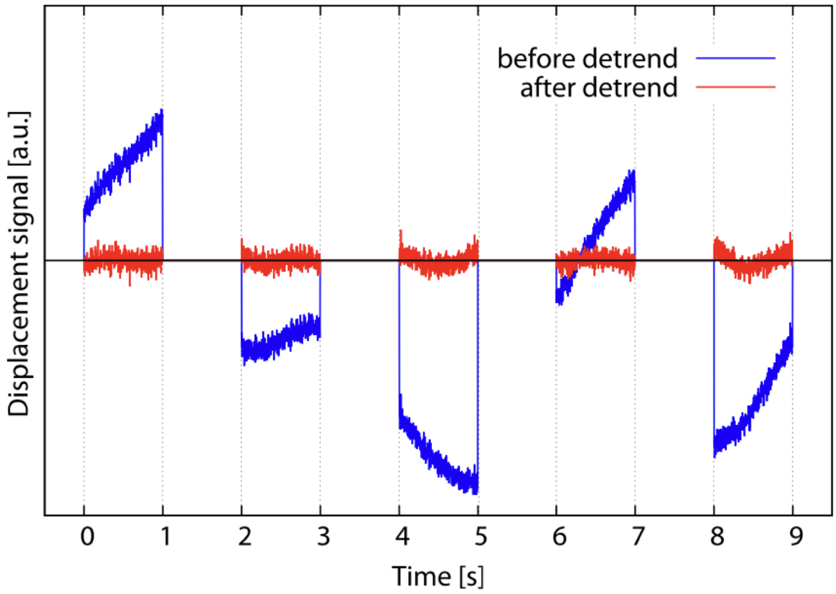

Fig. 2.5 Discontinuous data from JIFO before and after detrending [52].

To address the impact of the detrending process on the signal, we propose two solutions. The first straightforward approach is to detrend the template used in the matched filtering [55] in advance. In other words, we use a detrended template to match the detrended data. This way, the matching result should not be affected. Also, since the noises are also detrended equally at the same time, the SNR would not be affected. Another method is to re-trend the detrended data, i.e., restoring the linear component that was erroneously removed from the signal. The specific approach is to use the detrended result of a white Gaussian noise before (N) and after (N_d) detrending to obtain a transfer function of detrending (TF_d). Then, divide the detrended data by this transfer function in an attempt to obtain the displacement signal (X) before detrending, which does not contain the initial effect:

$$TF_d = \frac{N_d}{N}, \tag{2.2}$$

$$X = \frac{X_d}{TF_d}, \tag{2.3}$$

where the subscript d denoted $detrended$. However, this method still needs a further investigation since the detrend method is proved to have difference effect on the Gaussian noise compared with a pure monochromatic signal, as shown in Figure 2.6. Here the free-falling cycle time is set to be 1 s, and we can clearly see that there is an f^2 slope for the detrended Gaussian noise when the frequency is lower than 1 Hz. This means, for example, that the amplitude of the 0.1 Hz component of Gaussian noise will be reduced by a factor of 100, since its frequency is 1/10 of 1 Hz. However, if we conduct the detrend method for a 0.1 Hz monochromatic sine signal, it would be decreased by more than 100 times, which means the transfer function in Equation 2.2 needs to be modified.

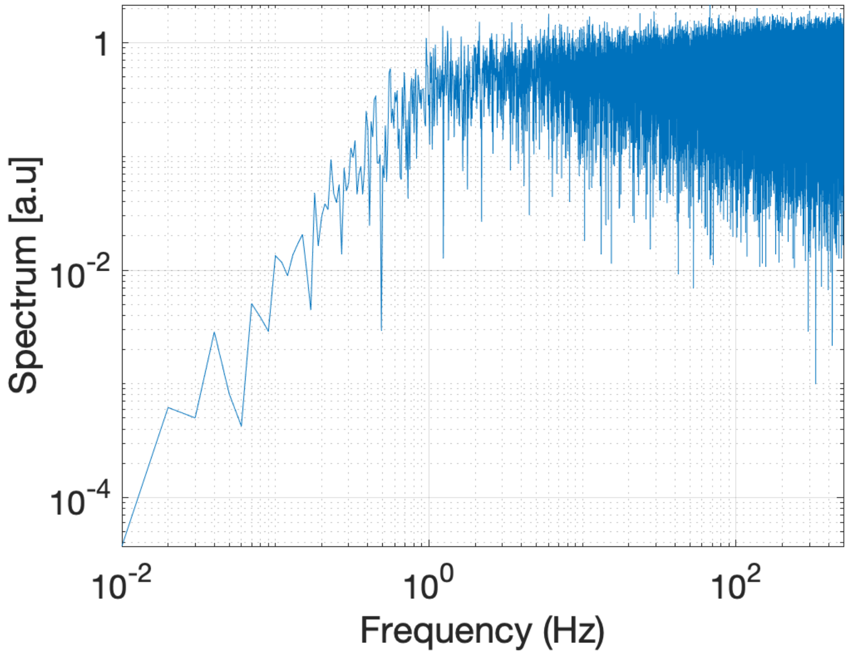

Fig. 2.6 Gaussian noise after detrending. The free-falling cycle time is set to be 1 s. The detrend process results in an f^2 slope when the frequency is lower than 1 Hz.

2.3 Data readout method

2.3.1 Mirror displacement signal from an interferometer

Interferometers are powerful tools that are widely used to measure small changes in distance which is even smaller than the wavelength of the laser. However, since the directly measured data is the laser intensity, it is necessary to convert this intensity variation into the change in distance, or the mirror displacement along the arm length. Since in the context of gravitational wave detection, the information of gravitational waves is concealed within the mirror displacement signal.

For a standard interferometer, the measured laser intensity at the output is the interference of E_x and E_y, which are the electromagnetic fields passing through the x-arm (right) and the y-arm (upper) of the interferometer, see in Figure 2.7a. The input filed can be written as:

$$E_{in} = A_0 \times e^{i\omega_0 t}, \tag{2.4}$$

with A_0 denoting the amplitude, and ω_0 the angular frequency of the laser. Then after the beam splitter and the travel along the x-arm and y-arm, E_x and E_y can be calculated by:

$$E_x = \frac{A_0}{2} e^{i(\omega_0 t + 2k(L+\Delta L_x))}, \tag{2.5}$$

$$E_y = \frac{A_0}{2} e^{i(\omega_0 t + 2k(L+\Delta L_y))}, \tag{2.6}$$

where k is the wave number, L is the arm length, and $\Delta L_x = -\Delta L_y$ represent the displacement of M1 and M2, respectively. The interfered intensity of E_x and E_y is:

$$P = |E_x + E_y|^2 = \frac{P_0}{2}(1 + \cos(\Delta\phi)), \tag{2.7}$$

where P_0 is the input power, $\Delta\phi = 2k|\Delta L_x - \Delta L_y|$ is the phase difference between the two beams. The interference intensity exhibits a cosine function with respect to $\Delta\phi$, as shown in Figure 2.8a.

If the intensity is near the middle fringe, such as point A in Figure 2.8a, we can directly infer the phase change, and therefore the mirror displacement, from the intensity variation. However, if the intensity is near a dark fringe or a bright fringe, such as point B, we cannot directly determine the phase change from the intensity variation because their relationship is no longer linear. In such cases, the laser should be modulated, as shown in Figure 2.7b, by introducing an electro-optic modulator (EOM) in the arm. In this case, the field E_x from the

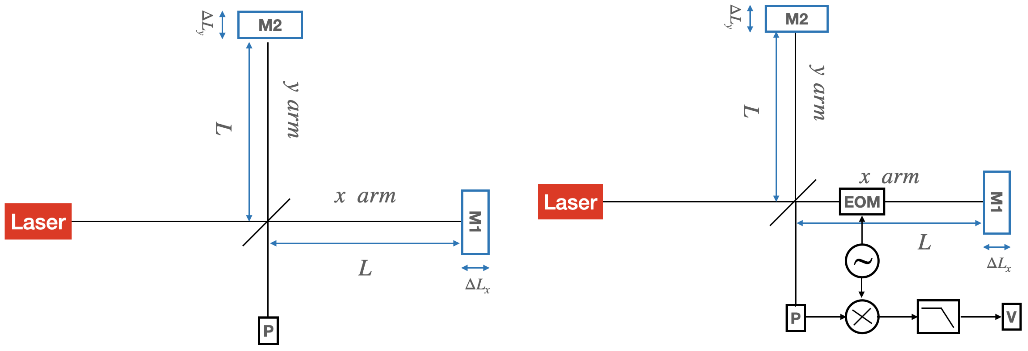

M2
ΔL_y
L
$y\ arm$
Laser
$x\ arm$
M1
L
ΔL_x
P
M2
ΔL_y
L
$y\ arm$
Laser
$x\ arm$
EOM
M1
L
ΔL_x
P
V

(a) without modulation

(b) with modulation

Fig. 2.7 Michelson interferometer with and without laser modulation.

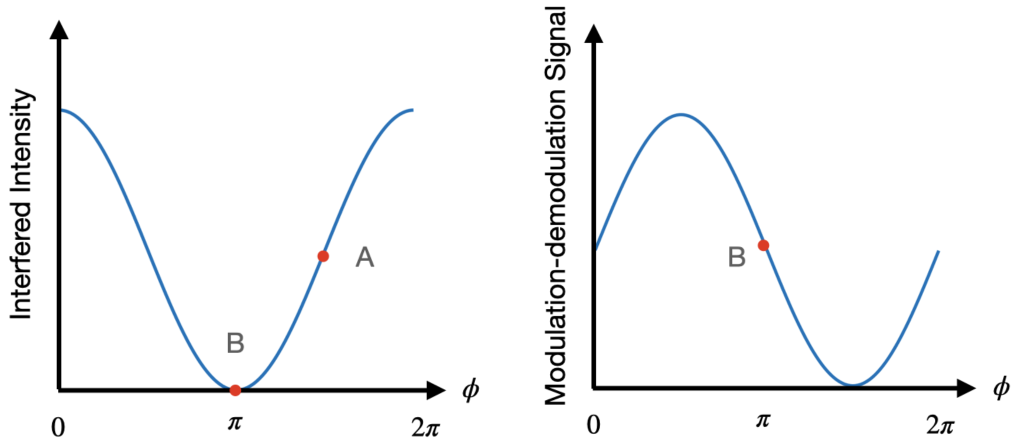

(a) Interfered intensity

(b) Modulation-demodulation signal

Fig. 2.8 Interfered intensity and modulation-demodulation signal changing with phase difference of two beams.

x-arm becomes:

$$E_x = \frac{A_0}{2} e^{i(\omega_0 t + 2k(L+\Delta L_x) + m \times \sin(\omega_m t))}. \tag{2.8}$$

Here, ω_m is the modulation frequency, and $m \ll 0$ represents the modulation depth. The interfered intensity becomes:

$$\begin{aligned} P &= |E_x + E_y|^2 \\ &= \frac{P_0}{2}(1 + \cos(\Delta\phi) + \frac{m^2}{4} + \frac{m^2}{4}\cos(2\omega_m) + m\sin(\omega_m t)\sin\Delta\phi). \end{aligned} \tag{2.9}$$

By demodulating the interference signal, i.e., mixing it with the modulation signal ($\sin\omega_m$t) and passing it through a low-pass filter, we obtain the demodulated signal:

$$\begin{aligned} V &= < P \times \sin(\omega_m t) > \\ &= \frac{P_0 m}{4} sin(\Delta\phi). \end{aligned} \tag{2.10}$$

Here the pointed brackets indicate averaging. Since the average value of the high-frequency signal is 0, the calculation of averaging is equivalent to low-pass filtering. It can be observed that the demodulated signal exhibits a sinusoidal function with respect to the phase difference between the two beams. Thus, even near dark or bright fringes (point B in Figure 2.8b), we can tell the phase change from the demodulated signal.

2.3.2 Pre-modulation

To prevent the free falling of the EOM, pre-modulation is more suitable for JIFO, which means to modulate the laser before it passes through the beam splitter. Additionally, the two arms of the interferometer must have different lengths, as shown in Figure 2.9. The length of the x-arm is shortened to L_x and the length of the y-arm is elongated to L_y. In this case, the phase difference of the two beams now has two components:

$$\Phi_o = k|L_y - L_x|, \tag{2.11}$$

$$\Delta\phi(t) = 2k|\Delta L_x - \Delta L_y|. \tag{2.12}$$

Also, assuming the input electromagnetic field has an amplitude of A_0, as defined in Equation 2.4, then E_x and E_y in this case are calculated by:

$$E_x = \frac{A_0}{2} e^{i\omega_0(t-t') + im\sin\omega_m(t-t')} e^{i2k\Delta L_x}, \tag{2.13}$$

$$E_y = \frac{A_0}{2} e^{i\omega_0(t+t') + im\sin\omega_m(t+t')} e^{i2k\Delta L_y}, \tag{2.14}$$

where $\omega_m t' = \Phi_0$ and $\omega_0 t' = 2n\pi$. The interfered intensity detected by the photodetector after a low pass filter is now:

$$\begin{aligned} P_{pd} &= < |E_x + E_y|^2 > \\ &= < |\frac{A_0}{2} e^{i\omega_0 t + im\sin\omega_m(t-t')} e^{i\frac{\Delta\phi(t)}{2}} \times (1 + e^{im\sin\omega_m(t+t') - im\sin\omega_m(t-t')} e^{-i\Delta\phi(t)})|^2 > \\ &= < \frac{P_0}{2}\{1 + \cos\Delta\phi(t) + 2m\cos\omega_m t\sin\Phi_0\sin\Delta\phi(t)\} > \\ &= \frac{P_0}{2}(1 + \cos\Delta\phi(t)). \end{aligned} \tag{2.15}$$

The demodulation signal is then:

$$\begin{aligned} V_1 &= < \frac{2P_0 m\sin\Phi_0}{2} \cos\omega_m t\sin\Delta\phi(t) \times \cos\omega_m t > \\ &= \frac{P_0 m\sin\Phi_0\sin\Delta\phi(t)}{2} \\ &= \frac{P_0 m_{\text{eff}}\sin\Delta\phi(t)}{2}. \end{aligned} \tag{2.16}$$

Here, the effective modulation depth is defined by $m_{\text{eff}} = m\sin\Phi_0$. We can see that if $\Phi_0 = 0$, V_1 would also be 0, making no mirror displacement signal in the modulation-demodulation output. A differential arm length is the key to obtaining a mirror displacement signal in the pre-modulation configuration.

2.3.3 Phase reconstruction

In order to determine the displacement signal using Equation 2.15 and Equation 2.16, it is necessary to lock the interferometer at bright/dark fringe or middle fringes by feedback controlling the displacement of the mirrors [56]. For mirrors in a free-falling state in JIFO, non-contact electromagnetic actuators could be utilized [57]. However, this is quite a challenging task.

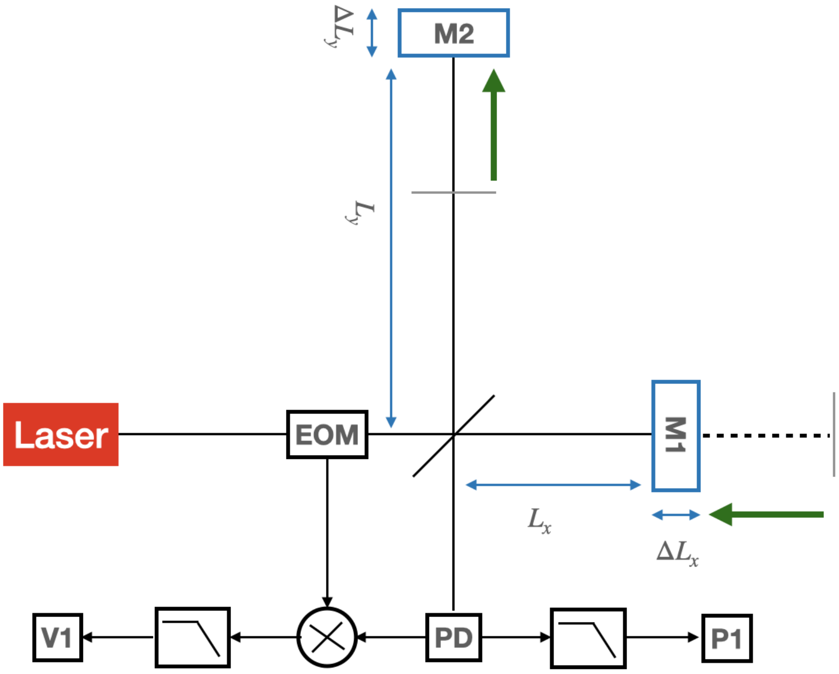

Fig. 2.9 Pre-modulated interferometer.

Here, we propose a method to reconstruct mirror displacement. For simplicity, we focus on the sine and cosine components of Equation 2.15 and Equation 2.16:

$$p_1 = \cos(\phi(t)), \tag{2.17}$$

$$v_1 = \sin(\phi(t)). \tag{2.18}$$

Usually, $\phi(t)$ can be obtained by taking the arc tangent of the ratio $\alpha = \frac{v_1}{p_1}$:

$$\phi(t) = \tan^{-1}\alpha + n\pi + \phi_0, \ \ n = 1,2,... \tag{2.19}$$

The integer n in the equation can be determined by phase unwrapping. However, the measured mirror displacement by JIFO undergoes oscillatory motion due to the influence of gravitational waves and the initial effects of each release, which makes phase unwrapping complicated [58]. As shown in Figure 2.10, assuming α_0 is measured at the time of t_0 and α_1 is measured at the time of t_1, we cannot determine directly whether the phase changed from ϕ_0 to ϕ_{1a} or ϕ_{1b} since both of them give the same tangent value.

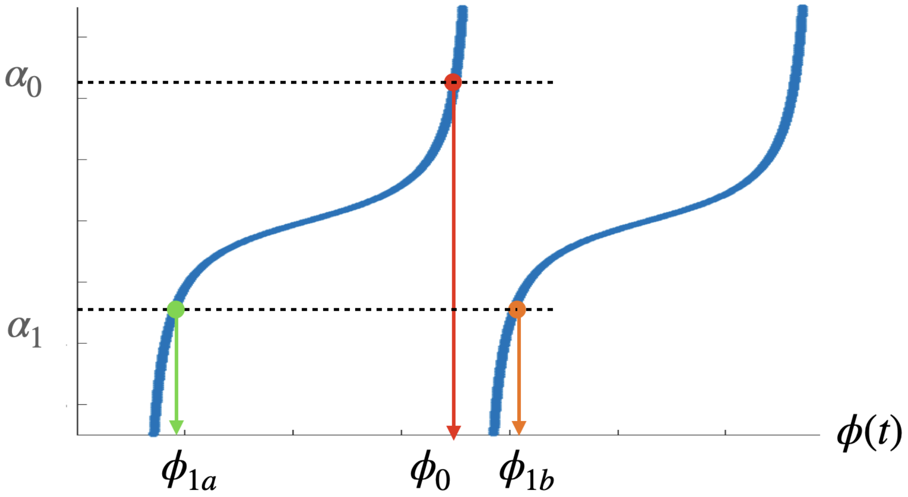

Fig. 2.10 Phase unwrapping from tangent $\phi(t)$. One cannot determine the exact phase for the value α_1.

This unwrapping difficulty can be solved by making two complex functions [59]:

$$p_1 + iv_1 = e^{i\phi(t)}, \tag{2.20}$$

$$p_1 - iv_1 = e^{-i\phi(t)}. \tag{2.21}$$

Then the differential of $\phi(t)$ can be calculated by:

$$\frac{d\phi(t)}{dt} = -i \times \frac{de^{\phi(t)}}{dt} \times e^{-i\phi(t)}. \tag{2.22}$$

Thus, the reconstruction of $\phi(t)$ can be achieved by integrating $\frac{d\phi(t)}{dt}$ over time, except that the initial value of the phase cannot be obtained:

$$\int_0^t \frac{d\phi(t)}{dt} dt = \phi(t) + const. \tag{2.23}$$

When consider the SNR of the reconstructed data, the modulation-demodulation signal (V_2) from the laser port would be helpful. The optical setup should then be updated to the version shown in Figure 2.11. Since $V_2 = -V_1$, the complex function in Equation 2.20 can be rewritten as:

$$e^{i\phi(t)} = p_1 + iv_1 = p_1 - iv_2. \tag{2.24}$$

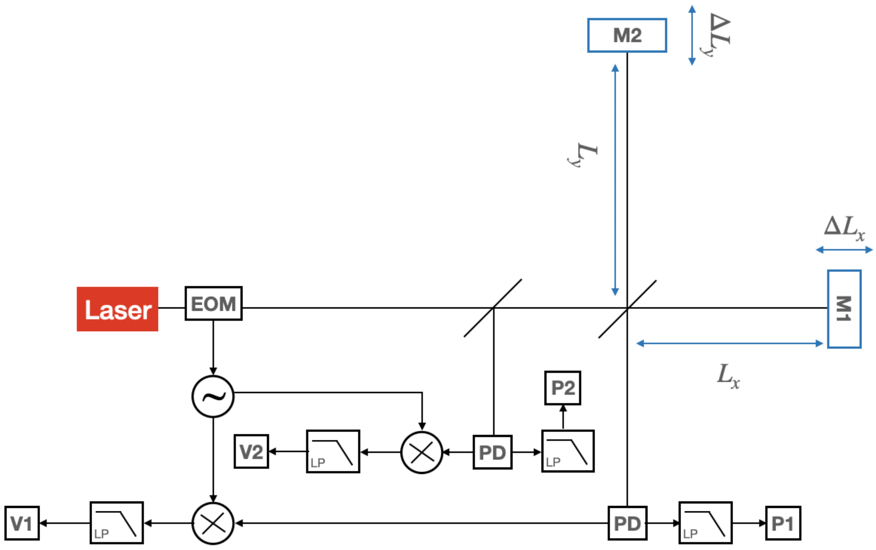

Fig. 2.11 Updated interferometer with two PD signals.

Here, we calculated the shot noise and signal in terms of power change. Shot noise is proportional to the fluctuation of photon number, which is the square root of the number of photons detected. We have the laser power $P = Nh\nu$, in which N, with the unit of [1/s], represents the number of detected photons per second, h is the Plank Constant, and ν is the laser frequency. The photon number fluctuation can then be calculated by $\tilde{N} = \sqrt{\frac{P\lambda}{hc}}$, also with the unit of [1/s]. The shot noise, with the unit of [J/s] or [W], is then calculated by:

$$n_{shot} = h\nu \times \tilde{N} = \sqrt{\frac{Phc}{\lambda}}. \tag{2.25}$$

Since the two PD signals are uncorrelated with each other, the total shot noise is calculated by:

$$n_{tot} = \sqrt{\sqrt{\frac{P_1 hc}{\lambda}}^2 + \sqrt{\frac{P_2 hc}{\lambda}}^2} = \sqrt{\frac{P_0 hc}{\lambda}}. \tag{2.26}$$

It is of interest to notice that the total shot noise does not change with $\phi(t)$, which means it is fringe-independent. Assuming V_2 has the same shot noise level with P_1, the SNR of

$e^{i\phi(t)} = p_1 - iv_2$ is then:

$$\begin{aligned} \mathrm{SNR}(e^{i\phi(t)} = p_1 - iv_2) =& \frac{P_0/2 \times \left| de^{i\phi(t)} \right|}{\sqrt{\frac{P_0 hc}{\lambda}}} && (2.27) \\ =& \frac{P_0 |d\phi(t)| \times |\cos(\phi(t)) + i\sin(\phi(t))|}{2\sqrt{\frac{P_0 hc}{\lambda}}} && (2.28) \\ =& \frac{|d\phi(t)|}{2} \sqrt{\frac{P_0 \lambda}{hc}}. && (2.29) \end{aligned}$$

Which is also fringe-independent with a value of half the SNR around the dark fringe.

By now, we have developed a new method to reconstruct the mirror displacement signal from the modulation-demodulation signal and the interfered laser power, without locking the interferometer while maintaining a constant SNR. This method is of great significance in that we can skip the difficulty of locking the free-falling mirrors and directly obtain a good SNR that is half of what it is at the dark fringe.

2.3.4 Analog-to-digital conversion of JIFO readout

In this section, we move to discuss the issue of analog-to-digital conversion for the readout of a JIFO. Since the measured light intensity change will be from dark to bright fringe, an analog-to-digital converter (ADC) with relatively high number of bits will be required to ensure sufficient resolution. The resolution of an ADC is calculated by the following equation:

$$dV_{ADC} = \frac{V_{FSR}}{2^b}, \tag{2.30}$$

where V_{FSR} is the span of the ADC with FSR denoting full-scale voltage range and b is the number of bits. If we assume an interferometer targeting a sensitivity of $dx = 10^{-19}$ m, the phase change would be $d\phi = \frac{2\pi}{\lambda} dx \approx 6 \times 10^{-13}$, given the laser wavelength $\lambda = 1\mu m$. The power change corresponding to the phase change according to Equation 2.15 can be deduced as follows:

$$dP_{pd} = d(\frac{P_0}{2}(1 + \cos\Delta\phi(t))) - \frac{P_0}{2} \sin\Delta\phi(t) d\phi \approx 3P_0 \times 10^{-13}, \Delta\phi(t) \ll 1, \tag{2.31}$$

which means that to ensure a sensitivity of $dx = 10^{-19}$ m, $dV_{ADC} = 3P_0 \times 10^{-13}$ is required. This put demand on the ADC to be of $\log_2(\frac{P_0}{dV_{ADC}}) = 42$ bits, while the common high resolution ADCs on the market today are 32 bits.

To solve the problem of analog-to-digital conversion, there is a method to try in addition to using a high-resolution ADC. That is, dividing the voltage range into different intervals for reading, each of which is small enough to ensure that the use of a standard ADC can also meet the required resolution.

At the same time the intensity of the laser light incident on the photodetector could be too high and would be a problem. We will either need to upgrade the existing photodetector or reduce the lase power layer by layer with multiple beam splitters.

2.4 Effects of cyclic movement

2.4.1 Additional Newtonian noise

As mentioned in Section 2.1.2, additional Newtonian noise would be generated due to the up-and-down cyclic movement of the mirrors in JIFO. In this section, we discuss the Newtonian noise of a JIFO from two kinds of sources: the walls (including ceiling, floor and 4 walls around) of the place where the JIFO is located and the masses around the mirrors.

The main gravitational force acting on the JIFO should be originated from the walls around it. The basic idea to consider Newtonian noise from the walls is the following: the cyclic movement of the JIFO results in the change in the distance from the mirrors to the wall; then the gravitational force of the wall on the mirror changes; finally, the gravity force along the interferometer arm results in mirror displacement noise for the detector.

If we assume that the ceiling and the floor are of infinite size, according to the Gauss' law, the gravity field in between should be uniform. So, in this case, there is no gravity force change when the mirror is moving, and therefore, no additional Newtonian noise. If they have a finite size of $a \times b$, the gravity along the x and y axis would be canceled when JIFO is moving along the central axis. Figure 2.12 gives an image for this situation. At the same time, the gravity along the z axis does not have influence on the mirror's movement along arm direction. The forces from the 4 walls around are also canceled with each other. Therefore, there is also no additional Newtonian noise sourced by the walls in this situation.

If JIFO is not located along the central axis but at (x0, y0, z0), then the gravity force from an area element $ds = dx \times dy$ in a coordinate of (x,y,z) would be:

$$\mathrm{d}F = \frac{G\rho m \mathrm{d}s}{\sqrt{(x-x_0)^2+(y-y_0)^2+(z-z_0)^2}^{\,2}}, \tag{2.32}$$

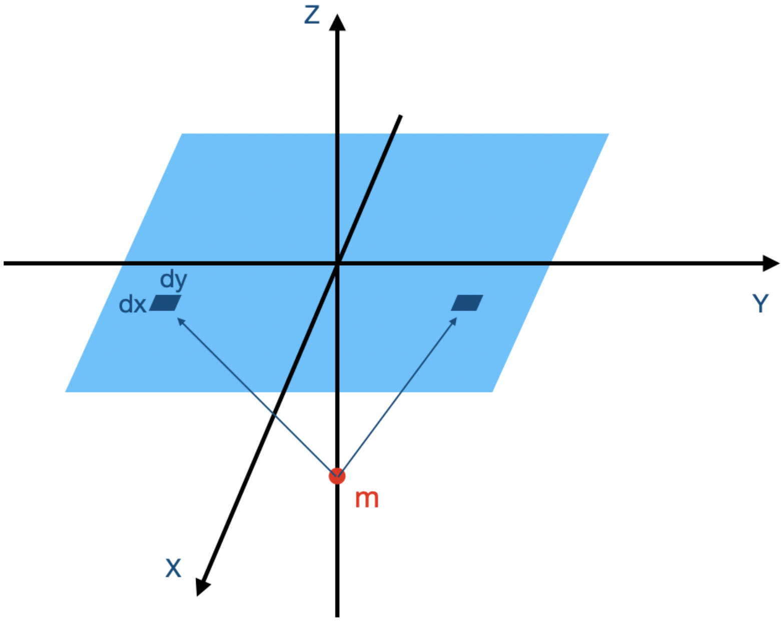

Fig. 2.12 Gravity force from the ceiling (blue parallelogram) to the mirror (red dot). When the JIFO is moving along the z axis, the gravity forces along the x and y axis are canceled with each other.

where m is the mass of the mirror, ρ is the area density of the wall and G is the gravitational constant. Project $\mathrm{d}F$ to the x direction gives:

$$\mathrm{d}F_x = \frac{G\rho m \mathrm{d}s}{\sqrt{(x-x_0)^2+(y-y_0)^2+(z-z_0)^2}^2} \times \frac{x-x_0}{\sqrt{(x-x_0)^2+(y-y_0)^2+(z-z_0)^2}}. \quad (2.33)$$

The acceleration caused from the gravity force from the wall is:

$$a = \int \frac{\mathrm{d}F}{m}, \quad (2.34)$$

and the integration of acceleration a gives velocity v, the integration of v gives displacement x, which is the Newtonian noise:

$$\begin{aligned} v &= \int a\,\mathrm{d}t, \\ x &= \int v\,\mathrm{d}t. \end{aligned} \quad (2.35)$$

Here, we assume that the JIFO is inside a rectangle of size $10\,\mathrm{m} \times 10\,\mathrm{m} \times 5\,\mathrm{m}$ and thickness $0.3\,\mathrm{m}$ making with concrete ($\rho = 1.44 \times 10^3 \mathrm{kg/m^3}$). The calculation result of the mirror displacement resulting from the walls around is about 3×10^{-8} m, which is significant compared with the expected gravitational wave signals. To avoid this, we should put the JIFO along the central axis of the room thus the gravity forces from the walls can be canceled, as discussed earlier.

Apart from the walls, there may be some other masses around the JIFO. If these masses are not moving, we can obtain the mirror displacement data for a time series before and after detrend process as shown in Figure 2.13. Here we assume that we have two JIFOs with staggered free-falling time, so there is no data gap between different cycles. Because the mirror would return to its initial position after each free-falling cycle, the displacement exhibits periodicity with a period equal to the free-falling time (cycle time, t_c) of the mirror. Then the mirror displacement spectrum will peak at $f = 1/t_c$ Hz and its harmonics, as shown in Figure 2.14.

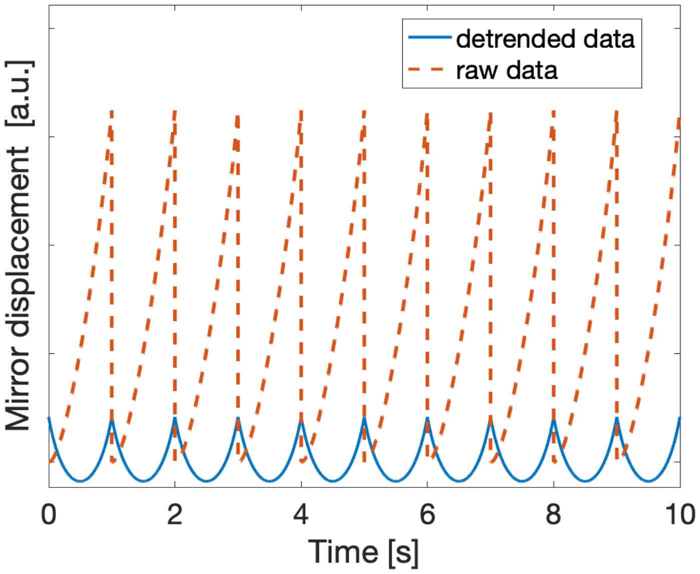

Fig. 2.13 Mirror displacement data resulting from a resting mass. The red doted line and blue solid line show the mirror displacement before and after the detrend process. The mirror's free-falling time is set to be 1 second and two JIFOs with staggered free-falling time are assumed.

Using the same method of calculating the Newtonian noise generated by the wall, Figure 2.15 gives the spectrum of the Newtonian noise strain resulting from a range of masses at different distances. The interferometer arm length is set to be $L = 10\,\text{km}$, which is the same as ET. A 100 kg mass, which is 1 m away from the mirror, would result in $7 \times 10^{-15}/(\sqrt{\text{Hz}})$ Newtonian noise at 1 Hz for an interferometer with 10 km arm length.

Based on the requirement of detection accuracy, we can further derive the requirement of mass distribution around JIFO. For example, to make sure that Newtonian noise is below

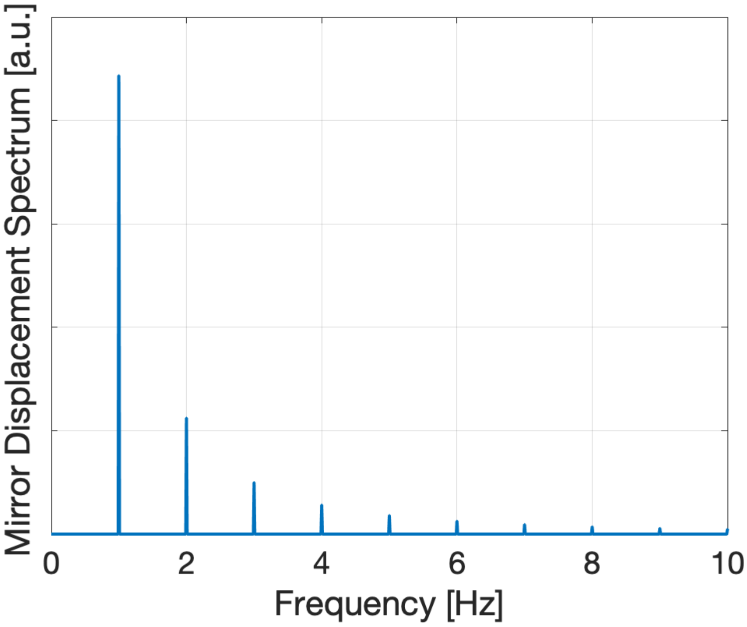

Fig. 2.14 Mirror displacement spectrum peaks at 1 Hz and its harmonics. The mirror free-falling time is set to be 1 second and two JIFOs with staggered free-falling are assumed.

$10^{-21}/\sqrt{\mathrm{Hz}}$ around 1 Hz, there should be no mass heavier than $\frac{100\,\mathrm{kg}}{7\times10^{6}} \approx 10^{-5}kg = 10\,\mathrm{mg}$ within a circle of 1 m diameter centered on the JIFO mirror. This evaluation is based on the fact that the gravitational force, and thus the Newtonian noise, is proportional to the mass. Or we can artificially place masses in symmetrical places to cancel the Newtonian noise produced by the original masses.

If the source is oscillating at a frequency of f, then the spectrum would show 2 side bands at $(f_c \pm f)$ Hz. Figure 2.16 shows the image of a mass around the mirror moving along the arm direction of the interferometer. The mirror displacement spectrum is shown in Figure 2.17, for which the oscillating source is moving at a frequency of $f = 0.1$ Hz and cyclic frequency of the JIFO is $f_c = 1$ Hz.

We should note that, the Newtonian noise discussed above is calculated for one of the mirrors in the interferometer while the total Newtonian noise should consider all of the mirrors, and there will be some cancellation and superposition between different mirrors. Figure 2.18 shows an image of 2 mirrors with an oscillating mass around them. In this case, we have the Newtonian noise proportional to the difference in the gravity force (ΔF) from the mass to the two mirrors expressed as:

$$\Delta F \sim \frac{1}{(D \pm A)^2} - \frac{1}{(L + D \pm A)^2}, \tag{2.36}$$

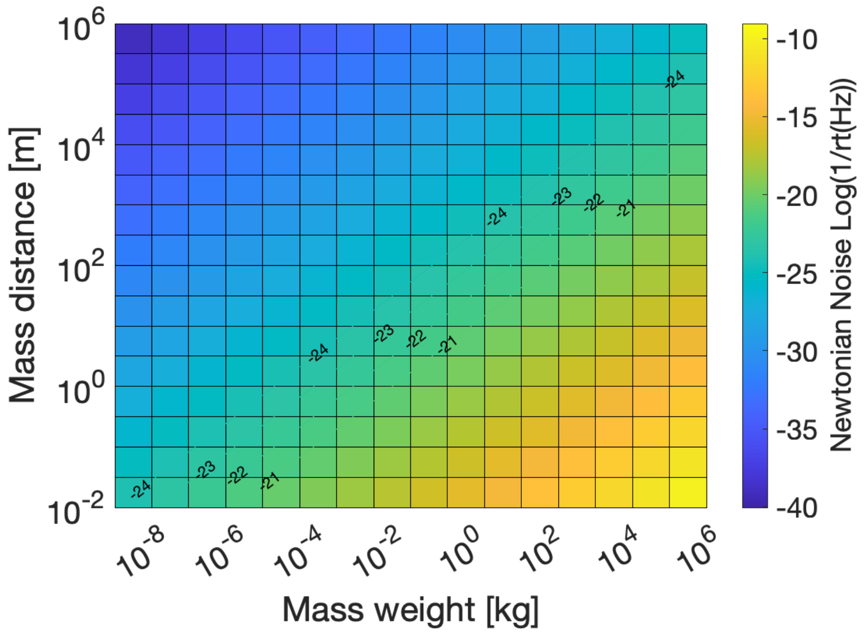

Fig. 2.15 Spectrum of the Newtonian noise resulting from a range of masses at different distances. The mass weight is ranging from $10^{-8} \sim 10^6$ kg, and the distance from the mass to the mirror ranges from $10^{-2} \sim 10^6$ m. The interferometer arm length is set to be $L = 10\,\text{km}$. The yellower the data, the louder the noise. The numbers on the colored squares indicate the logarithm value of the Newtonian noise corresponding to certain weights and distances.

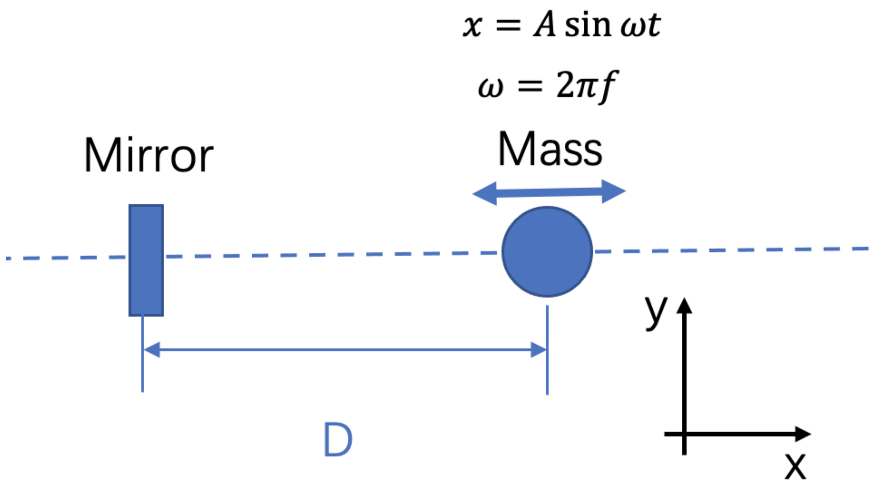

Fig. 2.16 Mirror and a moving mass around. The mass is oscillating along the arm direction (x direction) of the interferometer at a frequency of f.

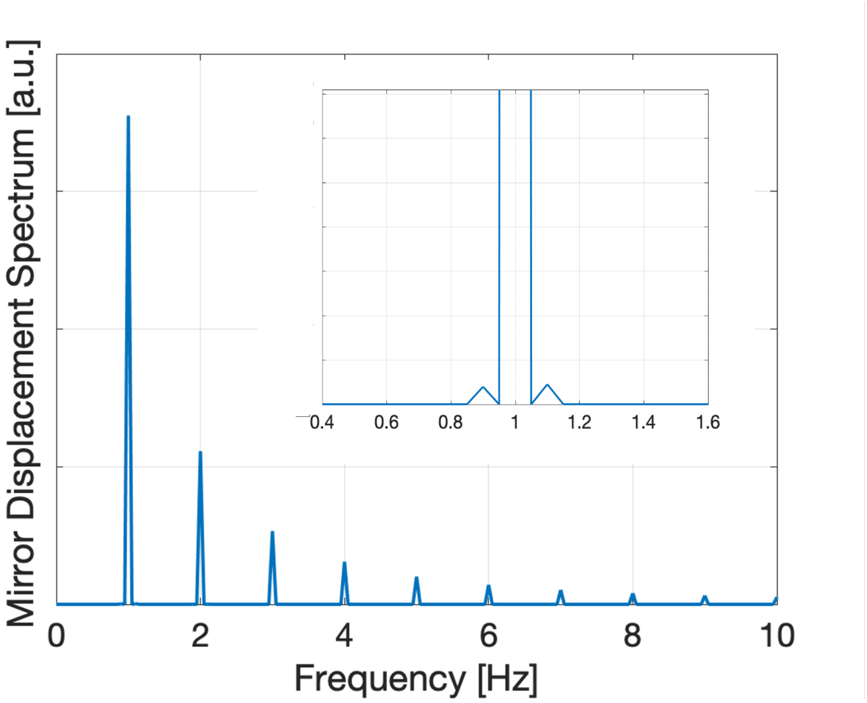

Fig. 2.17 Mirror displacement spectrum resulting from a moving source around. The oscillating mass is moving at a frequency of $f = 0.1$ Hz and cyclic frequency of the JIFO $f_c = 1$ Hz. The zoomed-in figure shows two side bands at 1.1 Hz and 0.9 Hz.

where D is the distance from the mass to one of the mirrors, L is the distance between the two mirrors and A is the oscillation amplitude of the mass. It is easy to see that when $A \ll D$, which would be the usual case, the amplitude of the vibration does not influence the gravity too much. Then consider the scale difference between D and L. When $A \ll D, D \gg L$, we have

$$\Delta F \sim \frac{1}{(D \pm A)^2} - \frac{1}{(L + D \pm A)^2} \sim \frac{2DL + L^2}{D^2 (D+L)^2} \sim \frac{2DL}{D^4} \sim \frac{2L}{D^3} \sim 0, \ A \ll D, D \gg L, \tag{2.37}$$

which means there are little difference in the gravity forces on the two mirrors, making the displacement noises of the two mirrors canceled with each other. When $A \ll D, D \ll L$, we have

$$\Delta F \sim \frac{1}{(D \pm A)^2} - \frac{1}{(L + D \pm A)^2} \sim \frac{2DL + L^2}{D^2 (D+L)^2} \sim \frac{L^2}{D^2 L^2} \sim \frac{1}{D^2}, \ A \ll D, D \ll L \tag{2.38}$$

which means that when D is small, a relatively large mirror displacement difference can be produced. This can be equated to the case when there is only one mirror.

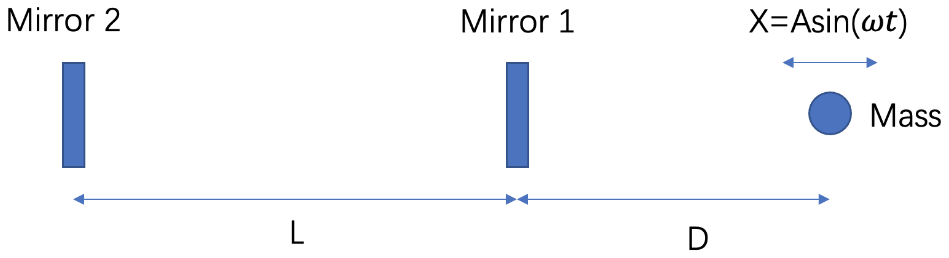

Fig. 2.18 Two mirrors and a moving mass around. The mass is oscillating along the arm direction (x direction) of the interferometer at an angular frequency of ω.

2.4.2 Signal upconversion

In Figure 2.17, we have seen that the low-frequency mass vibration (f) can be upconverted to ($f_c \pm f$) by the movement of the JIFO itself, with f_c the cyclic frequency of JIFO. This phenomenon triggers the following two inspirations: 1. JIFO may be able to serve as a Newtonian noise meter by monitoring the side bands; 2. Low-frequency gravitational wave signals may be able to be upconverted to the sensitive frequency band of the detector by the JIFO. These two ideals are simply explained below.

Taking ET as an example, the Newtonian noise of it around 1 Hz is buried under the other noises (see in Figure 2.2). However, it is worth measuring the Newtonian noise at this low-frequency band since it could become dominant in the future. The measurement can be achieved by a JIFO. If the cyclic frequency of JIFO is set to be 100 Hz, then the 1-Hz Newtonian noise will be upconverted to 99 Hz and 101 Hz, which are falling within the optimized sensitivity frequency band of ET.

Similarly, we can also consider a gravitational wave of 1 Hz passing by a JIFO. While the gravitational wave itself may not be intense enough to be detected directly at 1 Hz, there is a chance to see its upconversions at (100 ± 1) Hz, where the sensitivity of the detector is significantly greater compared to 1 Hz.

More detailed calculations are still required to be underwent in the context of more specific examples.

Chapter 3

Promising science cases of a Juggled Interferometer (JIFO)

In this chapter, the sensitivity curve of JIFO is evaluated. Based on this sensitivity, several science cases are analyzed, showing the ability of a JIFO to detect gravitational waves at around 0.1 - 10 Hz. This is the first time that the sensitivity curve of a JIFO is presented and analyzed. The noise budget of the Einstein Telescope is referenced for comparison in this chapter. Since the advantages of using free-falling mirrors in improving low-frequency sensitivity apply to all other interferometers on earth, the results presented in this chapter can also provide insights for other earthbound gravitational wave detectors.

3.1 Sensitivity improvement of a JIFO compared with ET

In this section, we will quantitatively discuss the improvement in gravitational wave detection sensitivity on earth by utilizing JIFO.

In Chapter 1 when the motivation of building a JIFO is stated, we presented the sensitivity curve of ET and identified seismic noise and suspension thermal noise as prominent noise sources in the low-frequency range. Here, we assume the construction of a JIFO with the same scale and exhibiting identical displacement noise as ET. In other words, we remove the isolator and suspension system from the ET setup and introduce a mirror free-falling system. The improved sensitivity curves are shown in Figure 3.1. The thick red line in the figure represents the sensitivity of ET, labeled as *suspended*, indicating that the mirrors in ET are designed to be suspended with fiber. The thick blue line represents the sensitivity of JIFO, labeled as *juggled*, indicating that the mirrors in JIFO are repeatedly released and undergoes free-falling motion. It can be observed that JIFO exhibits a significant

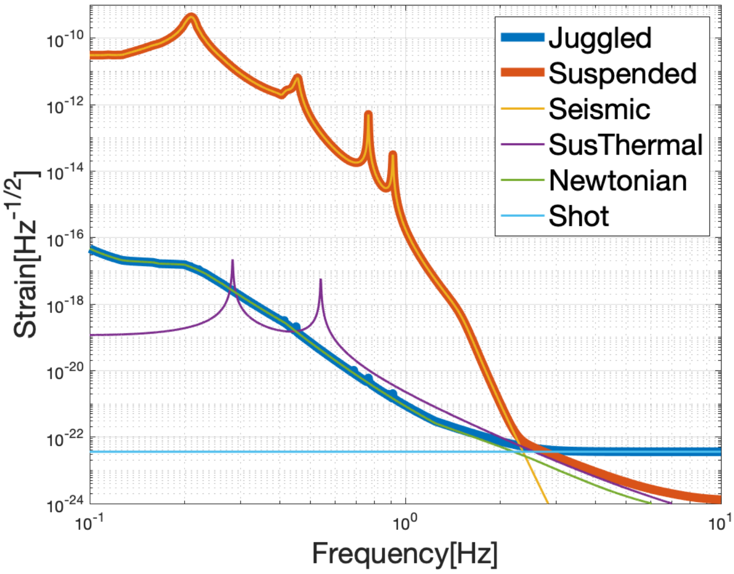

Fig. 3.1 Sensitivity curves and main noise sources of ET and JIFO [59]. The thick red line with a legend of *suspension* shows the sensitivity of ET and the blue line with a legend of *Juggled* shows the sensitivity of JIFO. Below 2.5 Hz, the dominant noise of ET is seismic noise and that of JIFO are Newtonian noise. At higher frequencies, the dominant noise for both detectors is shot noise.

improvement in sensitivity compared to ET below ∼2.5 Hz. After eliminating seismic noise and suspension thermal noise, the primary noise sources for JIFO at low frequencies are Newtonian noise, while at high frequencies, it is shot noise. In this analysis, we assume that the mass distribution around the interferometer is sufficiently uniform, thereby avoiding the generation of additional Newtonian noise due to the up-and-down motion of the JIFO mirror, as discussed in Chapter 2.

Based on the shot noise level, which is $h_{shot} \sim 10^{-23}/\sqrt{\text{Hz}}$ according to Figure 3.1, we can evaluate the laser frequency and amplitude noise requirements for JIFO. For an arm length of L=10 km, the shot noise and be converted to displacement noise: $\Delta X = h_{shot} \times L = 10^{-23} \times 10^4 \text{m}/\sqrt{\text{Hz}} = 10^{-19} \text{m}/\sqrt{\text{Hz}}$. Assuming there is a length difference of ΔL_{arm} =1 m for the two arms of the interferometer, then the frequency noise should be within:

$$\Delta f = c/\lambda \frac{\Delta x}{\Delta L_{arm}} = 3 \times 10^{-5} \text{Hz}/\sqrt{\text{Hz}}, \tag{3.1}$$

where $c = 3 \times 10^8$ m/s is the speed of light and $\lambda = 1064$ nm is the wavelength of the laser. Assuming the offset from the middle fringe is $\Delta L_{mid} = 10^{-13}$ m, then the power fluctuation should be within:

$$\frac{\Delta P}{P} = \frac{\Delta x}{\Delta L_{mid}} = 10^{-6}/\sqrt{\mathrm{Hz}} \tag{3.2}$$

3.2 Promising science cases

3.2.1 Detecting Quasi-normal modes of massive black holes

When we consider the oscillation of a string, of which both ends are fixed, we can obtain its normal modes, which are a series of standing waves that satisfy the condition where an integer multiple of the wavelength is equal to twice the string length. The corresponding frequencies are real numbers and are multiples of the fundamental frequency:

$$f_0 = 2L\frac{T}{m}, \tag{3.3}$$

where T is the tension in the string and m is the linear density. However, energy dissipation is not considered in this case, meaning that after the string is plucked, it will continue to vibrate with a constant amplitude. In the case of Quasi-normal modes (QNMs), the ends of the string are no longer fixed, and the energy of the oscillation escapes, causing the amplitude to decay over time. This decay can be represented as:

$$A(t) \approx A_0 e^{-\omega_2 t} \cos\omega_1 t \tag{3.4}$$

where A_0 is the initial oscillation amplitude, ω_1 represents the oscillation frequency and ω_2 represents the decay rate. Normally, QNMs are also written as:

$$A(t) = A_0 \times \mathrm{Re}(e^{i\omega t}), \tag{3.5}$$

$$\omega = \omega_1 + i\omega_2. \tag{3.6}$$

Here the QNM frequency ω is an imaginary number consisting of two parts, one being the oscillation frequency and the other being the decay rate. The curve of Equation 3.5 shows a shape of ringdown, as shown in Figure 3.2.

Studying the QNMs of black holes (BH QNM) is an important step in computing gravitational waveforms. The comparison of the theoretical calculation results and the actual detection results can help us understand the nature of black holes and test general relativity [60–62]. The process of binary black holes mergers is typically divided into three stages: inspiral, merger, and ringdown. This is illustrated in Figure 3.3. After the two black holes

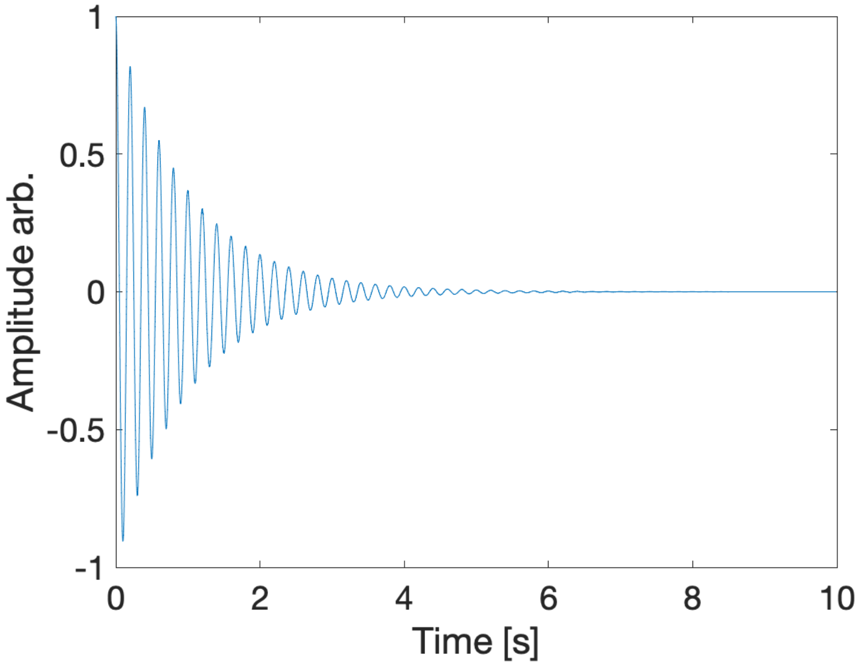

Fig. 3.2 Example of ringdown oscillation. The initial oscillation amplitude is set to be one, the oscillation amplitude is 5 Hz and the decay rate is 1.

merger into one, the resulting new black hole is still *ringing*, the generated gravitational waves at this stage can be approximated using QNMs. The gradual decrease in the amplitude of gravitational waves during the ringdown stage reflects the energy carried away by the waves from the system. Similar ringdown phenomena can also occur when particles fall into a black hole, causing perturbations in it.

The central frequency (f_c) of the BH QNM is proportional to the mass of black hole (M) [63]:

$$f_c(\mathrm{Hz}) = \frac{32 \times 10^3\,\mathrm{M}_\odot}{M} \times [1 - 0.63(1-a)^{0.3}], \tag{3.7}$$

where $a \in [0,1]$ is the spin angular momentum of the black hole, $\mathrm{M}_\odot$ is the solar mass. Figure 3.4 shows that the central frequency decreases as the mass of black hole increases, with a slope of M^{-1}. The dimensionless effective strain of the QNM can be estimated by [60]:

$$h_{\mathrm{eff}} \sim 3 \times 10^{-20} [\frac{E}{250\,\mathrm{M}_\odot c^2}]^{1/2} [\frac{f_c}{1\,\mathrm{Hz}}]^{-1/2} [\frac{r}{6\,\mathrm{Gpc}}]^{-1}, \tag{3.8}$$

where E is the emitted energy which is assumed to be 1% of the mass of the black hole in this thesis, r is the luminosity distance, and f_c is calculated by Equation 3.7. The dimensionless

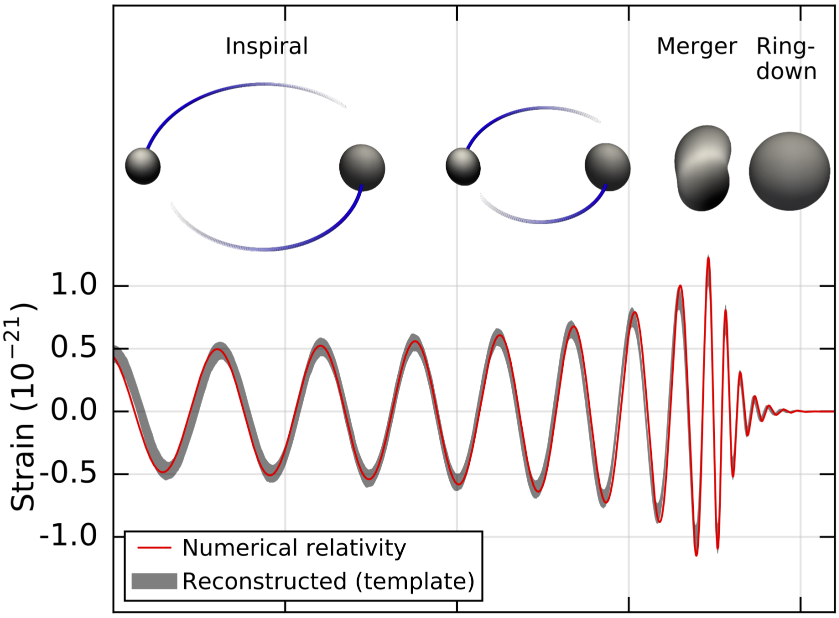

Fig. 3.3 Process of binary black holes merger [14]. The schematic on the top shows the three stages: inspiral, merger, and ringdown. The curves on the bottom are the strain of gravitational wave emitted during these processes. There is an obvious decay of the strain in the ringdown stage, which is the Quasi-normal mode of the resulting black hole.

effective strain can then be transferred to spectrum density using [64]:

$$S_h(f) = \sqrt{\frac{h_{\text{eff}}^2}{f}}. \tag{3.9}$$

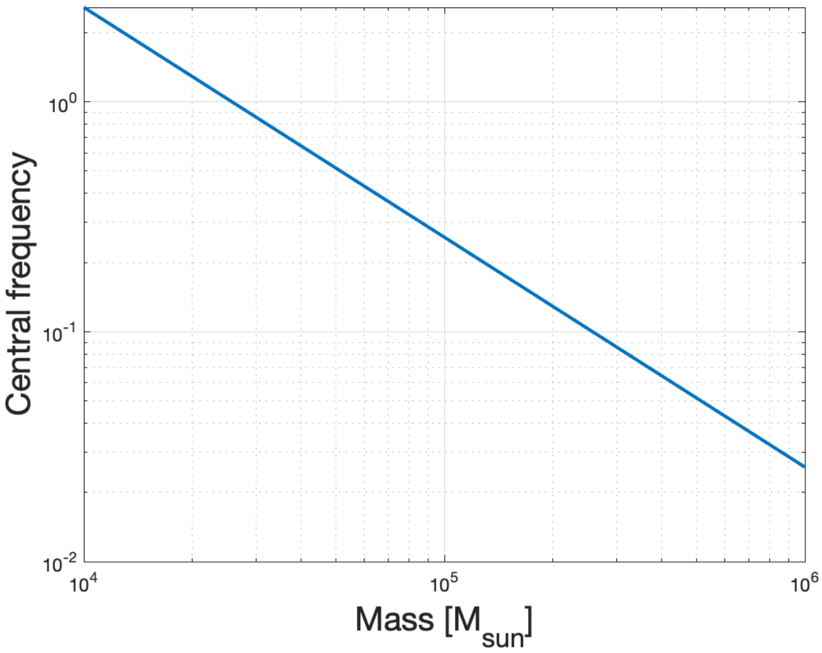

Fig. 3.4 Central frequency of the Quasi-normal modes of black holes as a function of mass. Spin $a = 0.98$.

When the central frequency falls within the range of 0.1 Hz to 2.5 Hz, it correspond to black holes roughly weighting $10^4 \sim 10^5 \mathrm{M}_\odot$, falling into the category of massive black holes. The calculated QNM spectrum is shown in Figure 3.5. The Algorithm Library Suite of LIGO Scientific Collaboration (lalsuite) [65] is used for the calculation here. We can see that the strain of QNMs from 0.5 Hz to ~1.7 Hz is above the sensitivity of JIFO but below that of ET, which means that these sources can only be detected by JIFO. Around 1.7 Hz, the detection has its maximum SNR, which approximately equals 200.

3.2.2 Testing Brans-Dicke theory

The Brans-Dicke (BD) theory is proposed by Carl H. Brans and Robert H. Dicke in the 1960s [66], which introduces a scalar field in addition to the tensor field in general relativity. As a result, in BD theory, the gravitational interaction is mediated not only by the curvature of

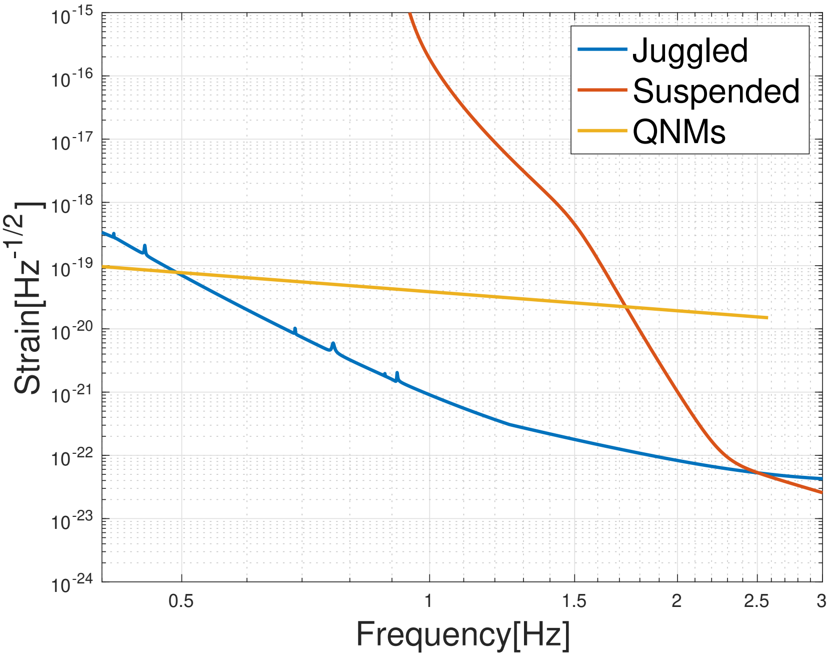

Fig. 3.5 Quasi-normal modes (yellow line) for massive black holes and the sensitivity curves for ET (red line) and JIFO (blue line) [59]. The sources are assumed at $z = 1$ with a spin $a = 0.98$.

spacetime but also by the scalar field. The strength of the coupling between the scalar field and mass in BD theory is determined by a parameter called BD parameter, ω_{BD} [67]. When $\bar{\omega} = 1/\omega_{BD}$ approaches zero, which means there is no coupling between the scalar field and mass, the BD theory is equivalent to general relativity.

Gravitational wave signal generated by a binary system can be used to constrain the upper limit of the $\bar{\omega}$ parameter, with at least one of the orbiting objects being a neutron star. The strain of gravitational waves generated from balck hole-neutron star (BH-NS) binaries is calculated in Figure 3.6. It can be seen that below 2.5 Hz, JIFO can obtain a better detection SNR than ET, and therefore, provide stronger constrain of the upper limit of $\bar{\omega}$.

To obtain the constraint on $\bar{\omega}$, we adopted the method described in [67, 68], and the key tool is the Fisher matrix. Assuming that the waveform h is determined by a series of parameters θ_i, the Fisher matrix can be calculated as follows:

$$\Gamma_{ij} \equiv \left(\frac{\partial h}{\partial \theta_i} \mid \frac{\partial h}{\partial \theta_j} \right). \tag{3.10}$$

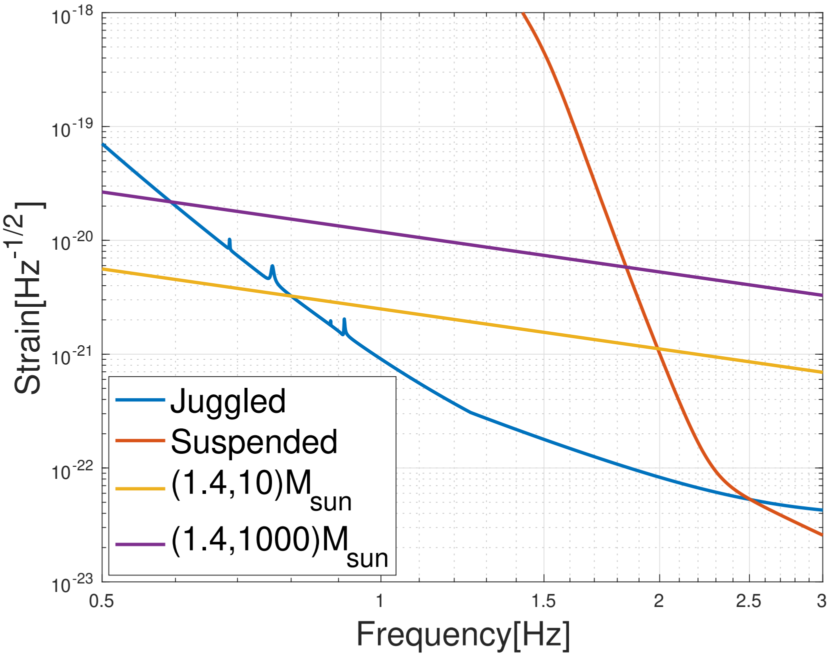

Fig. 3.6 Gravitational wave strain from NS-BH binaries and the sensitivity curves for ET (red line) and JIFO (blue line) [59]. The sources are located at 78 Mpc from the detector.

The definition of the inner product is the following:

$$(A \mid B) = 4\,\mathrm{Re}\int_0^\infty df \frac{\tilde{A}^*(f)\tilde{B}(f)}{S_n(f)}, \tag{3.11}$$

in which $S_n(f)$ is the noise spectrum of the gravitational wave detector.

The root-mean-squre (rms) error of the estimation of θ_i can be inferred from the square root of the diagonal elements of the inverse of the Fisher matrix as follows:

$$\Delta\theta^a = \sqrt{\Sigma^{aa}}, \tag{3.12}$$

$$\Sigma = \Gamma^{-1}. \tag{3.13}$$

The waveform of the gravitational wave here is written as:

$$\tilde{h}(f) = \frac{\sqrt{3}}{2}\mathbb{A} f^{-7/6} e^{i\Psi(f)}, \tag{3.14}$$

in which $\mathbb{A}$ is the amplitude:

$$\mathbb{A} = \frac{1}{\sqrt{30}\pi^{2/3}}\frac{\mathbb{M}^{5/6}}{D_L}, \tag{3.15}$$

and $\Psi(f)$ is the phase under the stationary phase approximation:

$$\begin{aligned}\Psi(f) =& 2\pi f t_c - \phi_c + \frac{3}{128}(\pi \mathbb{M} f)^{-5/3}\left[1 - \frac{5}{84}\mathbb{S}^2 \bar{\omega} x^{-1}\right.\\ &+ \left(\frac{3715}{756} + \frac{55}{9}\eta\right)x - 4(4\pi - \beta)x^{3/2}\\ &\left.+ \left(\frac{15293365}{508032} + \frac{27145}{504}\eta + \frac{3085}{72}\eta^2 - 10\sigma\right)x^2\right].\end{aligned} \tag{3.16}$$

where $\mathbb{S}$ can be calculated from the difference of the binding energy of the two bodies in the binary system, $\eta = \frac{m_1 m_2}{(m_1+m_2)}$ with m_1 and m_2 the mass of the two bodies in the binary system and $x = [\pi(m_1+m_2)f]^{2/3}$. The parameter set also includes f, the frequency of gravitational waves; D_L, the luminosity distance of the source; $\mathbb{M}$, the chirp mass; t_c and ϕ_c, the time and phase when the coalescence happens; β, the spin-orbit effect; and σ, the spin-spin effect. Since the $\bar{\omega}$ is expected to be zero if we agree with general relativity, then the rms error of it indicates the upper limit.

From the strain of gravitational wave from (1.4,10) $M_\odot$ and sensitivity of JIFO shown in Figure 3.6, we can calculate the Fisher matrix using Equation 3.10 and Equation 3.11. The distance is chosen to be 78 Mpc to have a detection SNR of 10 in the context of matched filtering [55]. The event rate of this detection is evaluated to be 0.01-1 in 5 years [69]. Assuming $t_c = 0$, $\phi_c = 0$, $\mathbb{S} = 0.3$, $\bar{\omega} = 0$, $\beta = 0$, $\sigma = 0$, the diagonal elements of the inverse of the Fisher matrix is calculated to be 1.14×10^{-5} for $\bar{\omega}$. This also gives the lower limit of $\omega_{BD} > 8.8 \times 10^4$. It is notable that $\mathbb{S} = 0.3$ is chosen for the NS-BH binary system, while binary BHs or binary NSs would give $\mathbb{S} \sim 0$, resulting in little effect from ω_{BD} to the waveform. The value of $\mathbb{S}$ also supports the reason why NS-BH binaries are chosen for ω_{BD} constraint. For comparison, we list some more constraint results obtained by other methods and detectors in Table 3.1:

Table 3.1 ω_{BD} constraint results from different detectors.

	Cassini	DECIGO	ET (f>1Hz)	JIFO (f<2.5 Hz)
ω_{BD}	$>4 \times 10^4$ [70]	$>2 \times 10^6$ [67]	$>10^6$ [71]	$>8.8 \times 10^4$ [59]

3.2.3 Primordial black holes research

Under the Big Bang theory, primordial black holes (PBHs) are believed to be formed during the radiation-dominated era in the early universe [72]. Due to the inhomogeneity of the universe, there were certain regions with high density. These regions underwent gravitational collapse inward and formed black holes when there were density fluctuations around, and these black holes are referred to as PBHs [73]. Unlike black holes formed from stellar collapse or binary mergers, PBHs can have a wide range of masses, ranging from very light to very heavy. Therefore, heavy PBHs are often discussed to explain the formation of supermassive black holes [74], and those with asteroid masses are considered as one of the candidates for dark matter [75, 76].

There are many ways to study PBHs, such as analyzing their effects on the cosmic microwave background radiation [77], studying their gravitational lensing effects [78], and studying the gravitational waves that accompany the formation of PBHs (PBH GW) [79]. The central frequency of PBH GW can be calculated from the mass of PBH (M_{PBH}) and the relativistic degree of freedom (g_*) when PBHs are formed:

$$f_{\mathrm{GW}} = 1\ \mathrm{Hz} \left(\frac{M_{\mathrm{PBH}}}{10^{17}\,\mathrm{g}}\right)^{-1/2} \left(\frac{g_*}{106.75}\right)^{-1/12}, \tag{3.17}$$

We can see that when the mass of the primordial black hole $M = 10^{17}$ g, the corresponding PBH-GW is around 1 HZ.

We assume that the primordial perturbation generating the PBH GW is a delta function of a monochromatic frequency [80]:

$$P_\zeta(k) = A_\zeta \delta(\log k/k_*), \tag{3.18}$$

where A_ζ is a normalization parameter indicating the amplitude of the perturbation and k is the wavenumber of the spectrum. The delta function peaks when $k = k_*$, where $k_* = 2\pi f_{\mathrm{GW}}/c$ with f_{GW} the frequency of PBH GW and c the speed of light. Then the energy density of PBH-GW is [80]

$$\begin{aligned}\Omega_{\mathrm{GW}}(\eta,k) =& \Omega_{r,0}h^2 \frac{3A_\zeta^2}{64}\left(\frac{4-\tilde{k}^2}{4}\right)^2 \tilde{k}^2 \left(3\tilde{k}^2-2\right)^2 \\ &\times \left(\pi^2 \left(3\tilde{k}^2-2\right)^2 \Theta(2\sqrt{3}-3\tilde{k})\right. \\ &\left.+ \left(4+\left(3\tilde{k}^2-2\right)\log\left|1-\frac{4}{3\tilde{k}^2}\right|\right)^2\right)\Theta(2-\tilde{k}),\end{aligned} \tag{3.19}$$

where $\Omega_{r,0}h^2$ is the density parameter of the radiation component at the present, with h the Hubble constant, $\tilde{k} = k/k_*$ is the dimensionless wavenumber and Θ is the Heaviside theta function defined by:

$$\Theta(x) = \begin{cases} = & 1, \quad x \geq 0 \\ = & 0. \quad x < 0 \end{cases} \tag{3.20}$$

The energy density can then be converted to spectrum density according to [80]:

$$S_h(f) = \Omega_{\mathrm{GW}} \frac{3H_0^2}{2\pi^2 f_{\mathrm{GW}}^3}, \tag{3.21}$$

Figure 3.7 shows the strain of PBH GW, which peaks at 1 Hz, together with the sensitivity curves of ET and JIFO with a one-year correlation. We can again see that this PBH GW can be detected by JIFO, while it is beyond the detection ability of ET. The detection SNR is calculated to be 19 according to the method in [81].

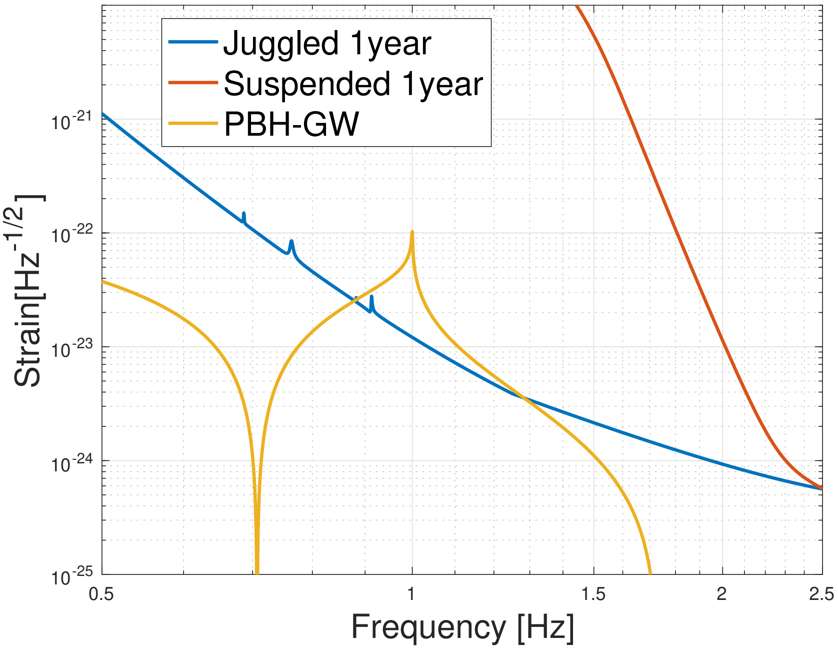

Fig. 3.7 Strain of PBH GW peaking at 1 Hz, together with the sensitivity curves of ET (red) and JIFO (blue) with a one-year correlation [59]. The perturbation amplitude parameter A_ζ takes the value 5×10^{-3} and the current radiation density parameter $\Omega_{r,0}h^2$ is 10^{-4}.

Chapter 4

Principle verification experiment

In this chapter, the proof-of-principle experiment of JIFO will be introduced. No similar experiments have ever been carried out in any prior researches.

So far, in this thesis, we have discussed that the test masses (mirrors) of the JIFO are repeatedly released and clamped with controlled manipulation. Additionally, in order to obtain gravitational wave signals, the laser is also modulated and demodulated. However, in the principle verification experiment, we initially do not employ feedback control for the mirrors, nor do we perform modulation and demodulation of the laser. Also, the prototype scale is much smaller compared to the current size of gravitational wave detectors. As a first step in the experimental attempt, our objectives are:

1. Achieving the releasing and catching of the mirrors.
2. Minimizing the tilt of the released mirror in the air.
3. Characterizing the performance of the experimental system and providing solutions accordingly.

4.1 Overview of the experiment

The layout of the entire experiment is depicted in Figure 4.1. Region 1 shows the optical path on the optical table, where the laser beam is coupled into the optical fiber; details can be found in Section 4.2.1. The laser beam is incident into the adjacent vacuum tank through the optical fiber. The interferometer will be set up inside the tank. The specific optical path can be found in Section 4.2.2, and details about the vacuum tank and photodetector will be described in Section 4.4.

Region 2 corresponds to the free-falling system, where a linear stage is fixed inside the frame. By controlling the motion of the linear stage, the release and catch of the mirror can be achieved. This part will be discussed in Section 4.3.

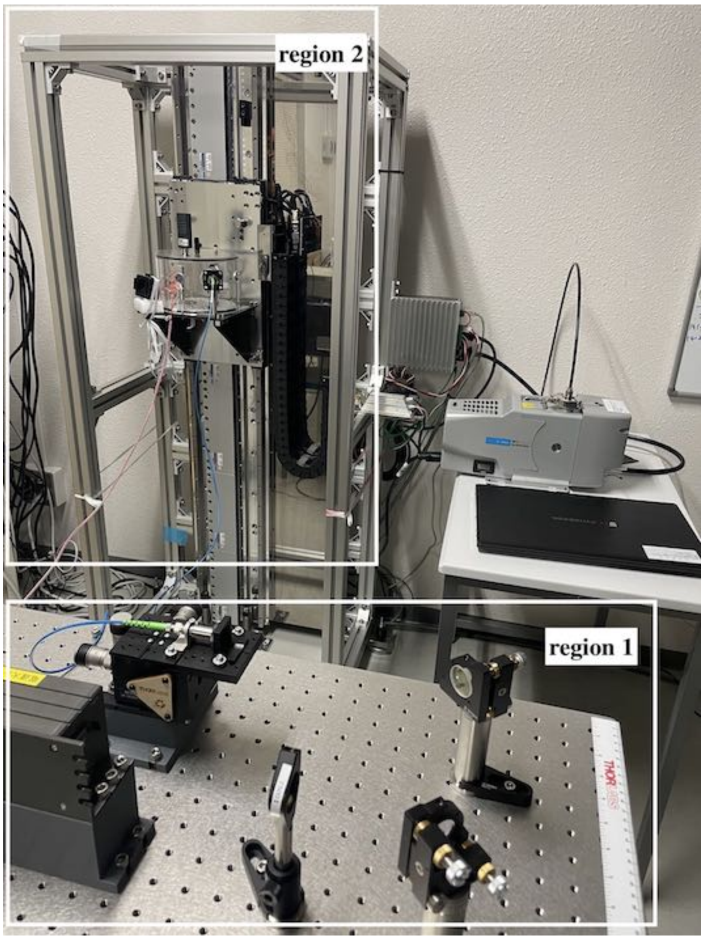

Fig. 4.1 Overview of the experiment setup. The laser beam is first coupled into an optical fiber in region 1 (see 4.2 for details), and then injected into a vacuum tank see (4.4b for details). The linear stage in region 2 is used to realize the mirror free falling.

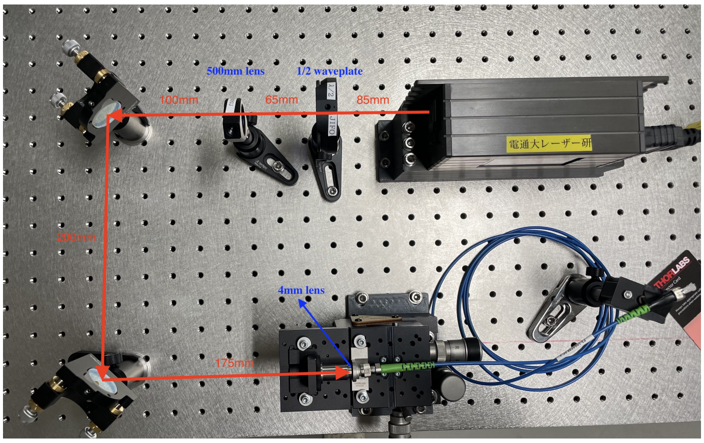

(a) optial path

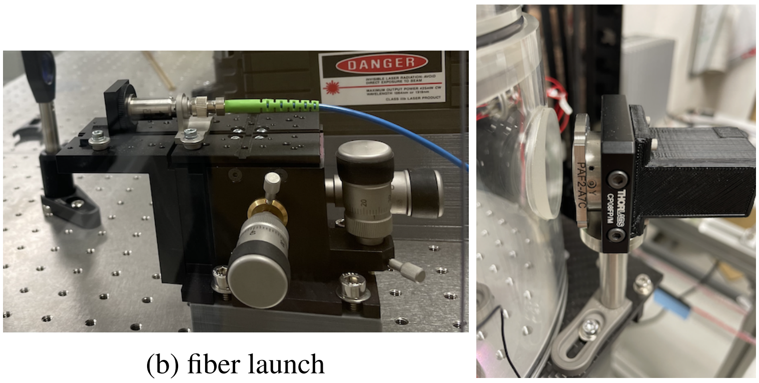

(b) fiber launch

(c) output collimator

Fig. 4.2 Laser beam coupling into a fiber. The 500 mm lens and 4 mm lens are used to focus the light beam onto the fiber head to ensure maximum coupling efficiency. The laser beam first enters the fiber fixed on the fiber launch, and before entering the vacuum tank, it passes through a collimator.

4.2 Optical setup

4.2.1 Fiber coupling

As the JIFO undergoes continuous vertical movement, it is demanded that the light beam also needs to move accordingly. However, directly moving the light source poses significant risks. Therefore, we employed optical fibers. On the optical table, we first couple the laser beam into the optical fiber, and then secure the output end of the fiber onto the platform where the interferometer is placed. Figure 4.2 shows the fiber coupling setup. By adjusting the two reflection mirror and the fiber launch carefully, a coupling efficiency of 64% is achieved. The input power before the fiber (right after the 4 mm lens) is 11 mW, and the output power after the fiver is 7 mW .

There is an important consideration regarding the laser-to-fiber coupling. In order to minimize the return loss, the fiber end is typically cleaved at an angle of 8 degrees. To ensure that the laser beam enters the fiber parallel to its axis, a fiber connector with a 4-degree angled surface should be selected for connection. This can be calculated from simple geometric principles and the laws of refraction. As shown in Figure 4.3, the laser beam vertically incident forms a 4-degree angle (angle A) with the perpendicular to the surface of the fiber connector. Additionally, due to the 8-degree cleave angle on the fiber surface, the incident angle of the laser beam onto the fiber, denoted as angle B, can be calculated to be 8 + 4 = 12 degrees. By applying the law of refraction, considering the refractive index of air ($n_1 = 1$) and the refractive index of the fiber ($n_2 = 1.5$), the resulting exit angle, denoted as angle C, can be calculated as 8 degrees, ensuring that the exiting light ray is parallel to the fiber:

$$\frac{\sin B}{\sin C} = \frac{n_2}{n_1}. \tag{4.1}$$

In our experiment, *THORLABS HBF*005 with a 4.05 degrees angle is used to fit with the cleaved fiber.

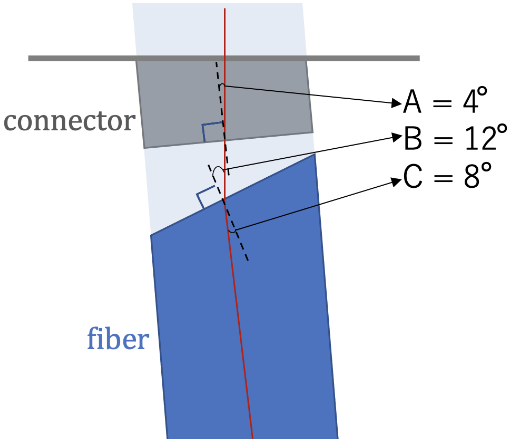

Fig. 4.3 Fiber connector (4° surface, gray) and fiber (4° cleaved, blue). With an incident angle satisfying the law of refraction, the laser beam, shown as a red line, travels parallel to the fiber.

4.2.2 Tilted end mirror

In Section 2.3, we present a data readout method that requires both the interference signals at the output end of the interferometer and one returning to the laser end. Therefore, an additional beam splitter is needed. In the proof-of-principle experiment, to reduce the number

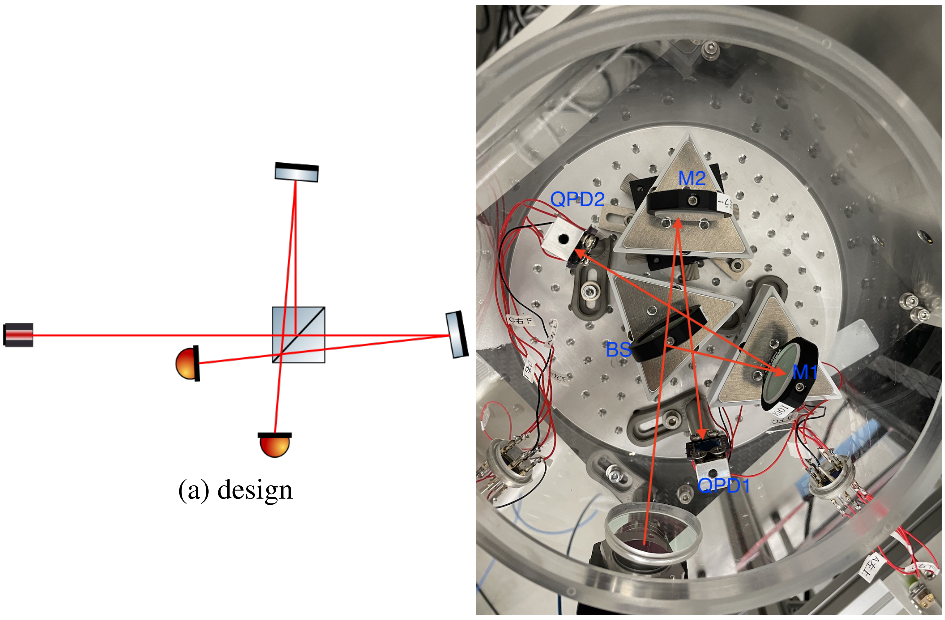

(a) design

(b) setup in the vacuum tank

Fig. 4.4 Interferometer with tilted end mirrors. This setup helps in obtaining two interference signals with only one beam splitter.

of free-falling mirrors, we chose to slightly tilt the two end mirrors of the interferometer, such that the reflected laser beams are slightly staggered from the incident light path, enabling the acquisition of two interference signals using a single beam splitter, as illustrated in Figure 4.4.

4.3 Free-falling system

The free-falling system serves as a crucial part of this experiment. We aim to achieve mirror free-falling in the simplest manner possible, while ensuring two key aspects: 1. Automatic realignment of the mirror after each release, and 2. Safety of the mirror during the moving process. To accomplish this, we have devised a triangular mirror holder (see Section 4.3.2), and implemented the release of the mirror and its safety assurance through control of a linear stage (see Section 4.3.3).

4.3.1 Mirror tilt upper limit

To achieve automatic realignment, it implies that the mirror should maintain an interference state every time it returns to the initial position. Thus, we can calculate a maximum allowable tilt (upper limit) for the mirror. As shown in Figure 4.5, to ensure interference between two laser beams, the wavefront displacement between them should be smaller than the wavelength (λ) of the laser. Considering that a rotation of the mirror by an angle θ results in a rotation of the light beam by 2θ, we have the following relationship, for a wavelength $\lambda = 1\,\mu$m, beam waist $b = 0.5\,$mm and, $\theta \ll 1$:

$$\Delta x = 2\theta b \ll \lambda, \tag{4.2}$$

$$\theta \ll \frac{\lambda}{2b} \approx \frac{1\,\mu\text{m}}{1\,\text{mm}} = 10^{-3}. \tag{4.3}$$

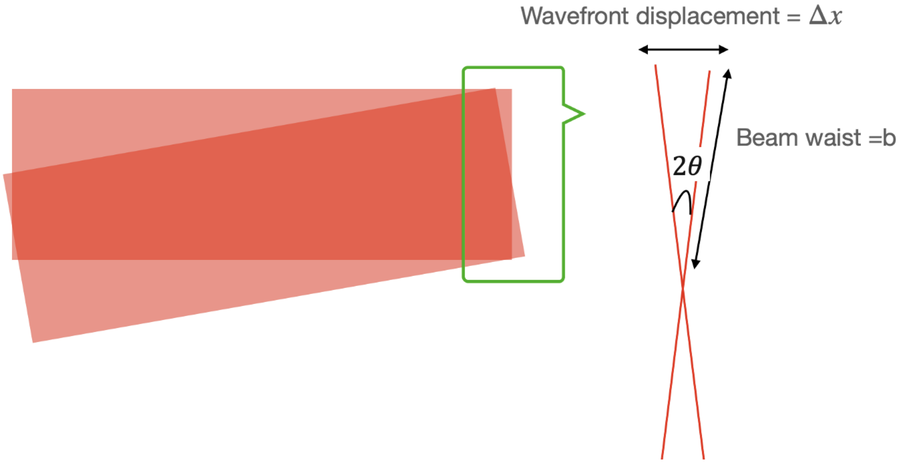

Fig. 4.5 Requirement on the mirror tilt to maintain interference. The wavefront displacement between two laser beams should be smaller than their wavelength.

For a more precise calculation, we need to use the formula for a Gaussian beam. Considering a laser beam propagating along the z-axis and focusing on the fundamental mode, the electric field distribution in the x direction can be expressed as follows:

$$A(x,z) = A_0 \frac{\omega_0}{\omega(z)} \times e^{-\frac{x^2}{\omega(z)^2}} e^{\frac{ikx^2}{2R(z)} + i\phi_0 - ikz}, \tag{4.4}$$

where A_0 is the amplitude of the electric field when x and z are equal to 0, ω_0 is the beam radius, beam size $\omega(z) = \omega_0[1 + (z/z_0)^2]^{1/2}$, wavefront radius of curvature $R(z) = z[1 + (z_0/z)^2]$, Guoy phase $\phi_0 = \text{atan}(z/z_0)$ and Rayleigh length $z_0 = \frac{1}{2}k\omega_0^2$ with k the wavenumber. Then the optical axes of the two beams in Figure 4.5 can be considered to be tilted from the z-axis by an angle θ. Thus, we have the following transformations by denoting the two tilted beams as $A'(x',z')$ and $A''(x'',z'')$:

$$
\begin{aligned}
A'(x',z') &= A(\cos\theta x - \sin\theta z, \sin\theta x + \cos\theta z), &(4.5)\\
A''(x'',z'') &= A(\cos\theta x + \sin\theta z, -\sin\theta x + \cos\theta z). &(4.6)
\end{aligned}
$$

Then the interference intensity of this two beams can be easily calculated by: $(A' + A'')(A' + A'')^*$. Figure 4.6 shows the electric field intensity distribution of the tilted beams (blue and red) and their interference intensity (yellow) around the bright fringe when the tilt angle $\theta = 10^{-3}$ rad.

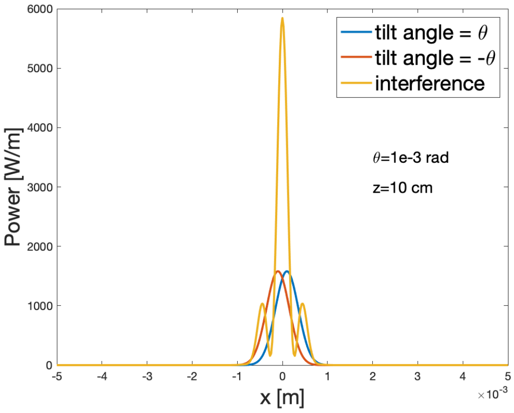

Fig. 4.6 Interference of two tilted beams around the bright fringe. The yellow line shows the interference at z = 10 cm with a tilt angle of $\theta = 10^{-3}$ rad. The intensity of the two tilted beams (blue and red) is 1 W each, the beam waist is 0.5 mm, and the wavelength is 1064 nm.

We can find that due to the tilt of the two beams, the interfered light will exhibit fringes instead of a simple bright spot. From the photodetector, we would see that output intensity is decreased since it is the integrated value of the interfered light in Figure 4.6 that a photodetector measures. When a gravitational wave passes through, the two arms of the interferometer will have differential length changes, and the travelling paths of the two beams will also undergo changes: one arm elongates ($z' +$ dz) while the other contracts ($z'' -$dz). As a result, the total intensity will show variations in brightness with respect to dz, manifesting as flashing of the beam spot at the output port. The numerical calculation results for the in interference intensity are illustrated in Figure 4.7. Here, we define the contrast of these brightness variations as follows:

$contrast = (max\,power - min\,power)/(max\,power + min\,power)$.

A zero contrast indicates the absence of interference. Figure 4.8 demonstrates the relationship between contrast and the tilt angle of a mirror. It can be observed that when theta exceeds 10^{-3} rad, the contrast tends towards zero, which means no interference. To achieve a contrast greater than 90%, theta needs to be less than 10^{-4} rad.

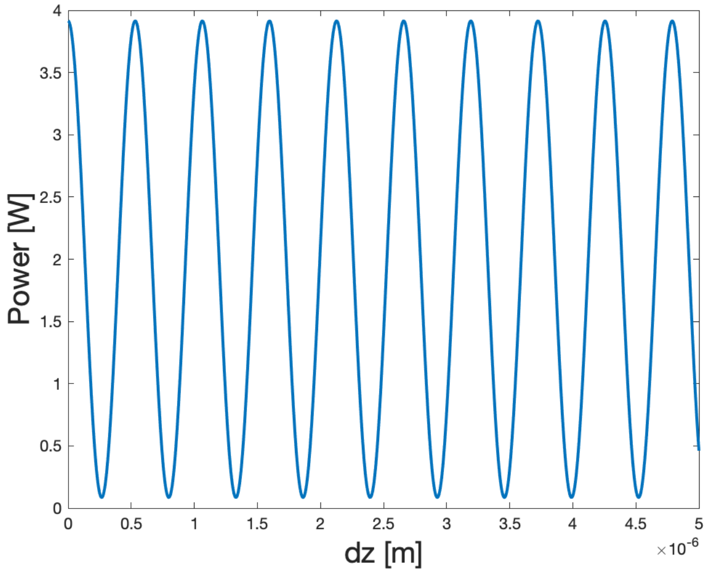

Fig. 4.7 Interference intensity change as the arm length of the interferometer changes. The mirror tilt angle is 10^{-4} rad, the input power of two beams is 1 W each, and the laser wavelength is 1064 nm.

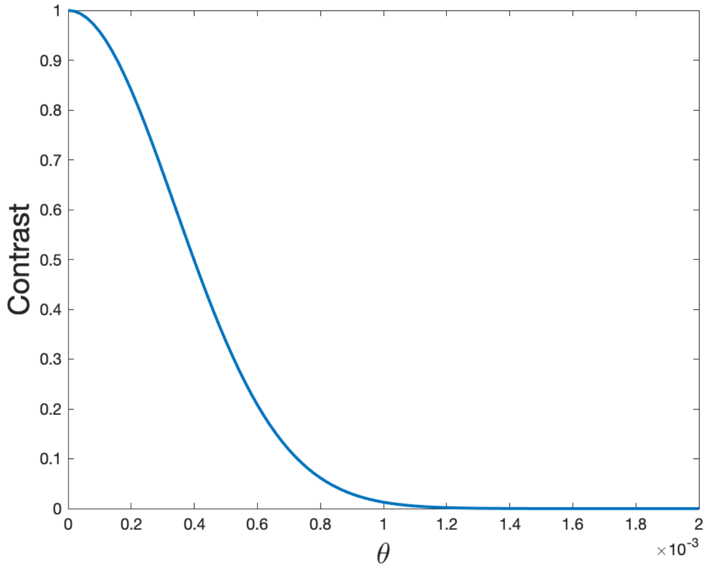

Fig. 4.8 Interference contrast changing with the mirror tilt.

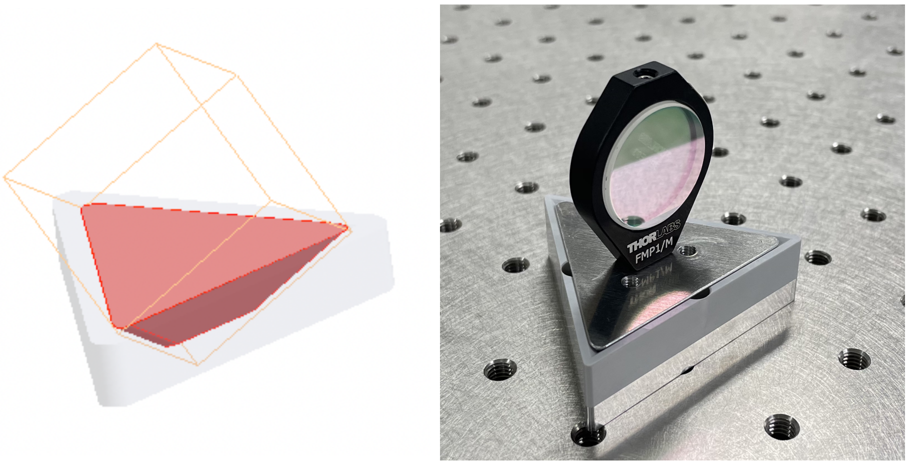

(a) design

(b) actual picture

Fig. 4.9 Mirror holder.

4.3.2 Mirror holder design and test

We designed and tested the mirror holder from three aspects: shape, size, and material. Our target, as demonstrated earlier in Section 4.3.1, is to ensure that the tilt angle of the mirror upon its return is less than 10^{-3} rad, preferably smaller than 10^{-4} rad for a better contrast.

Firstly, for the shape, the design inspiration is derived from creating a *slot* for the mirror, allowing it to fall back into its initial position and automatically realign after each release and return. The design is shown in Figure 4.9a: the gray area represents the slot (base), while the mirror is secured on the red part, referred to as the mirror holder. The mirror holder is a part of a cube and has a face-to-face contact with the base below. For an actual picture, please refer to Figure 4.9. From a minimum equilibrium perspective, a point-to-face contact between the base and the mirror holder would also be a stable solution. However, due to constraints such as manufacturing precision and model size, we could not make it to achieve a smooth enough contact point, resulting in excessive friction. Therefore, we ultimately opted for this face-to-face contact approach.

Secondly, we tested models of different sizes to find out an optimal one. On one hand, due to limitations imposed by other equipment, we needed to minimize the size of the mirror holder. On the other hand, considering that the mirror itself has a diameter of 1 inch and a mass of 20 g, excessively small mirror holders would not be conducive to maintaining balance. Therefore, we made three models of different sizes for comparison: large (8.5 cm), medium (5.5 cm), and small (2.5 cm) triangle side lengths, as shown in Figure 4.10.

Figure 4.11 shows the optical path of our test. The laser is incident on a beam splitter, with the reflected light serving as a reference, and the transmitted light incident on the mirror fixed

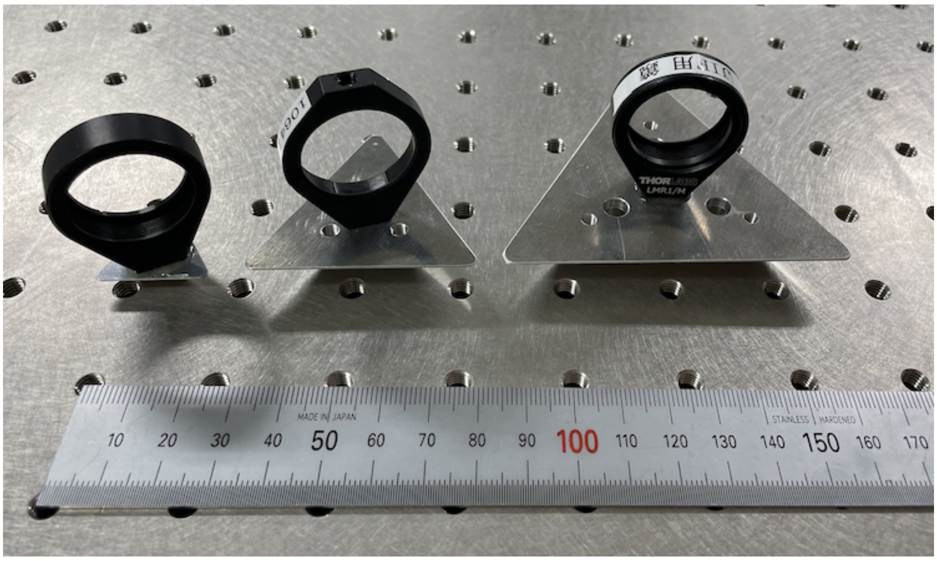

Fig. 4.10 Three sizes of mirror holders.

on the triangle-shaped mirror holder. The position of the reflected beam spot is monitored using a beam profiler. The distance between the beam profiler and the mirror holder is 50 cm in this setup. During testing, we repeatedly picked up and released the mirror, recording the position of the reflected beam on the beam profiler. The probability distribution plot of the beam spot positions was generated as shown in Figure 4.12. We performed fitting using a Gaussian distribution curve on the data and obtained their standard deviations as shown in Table 4.1. The beam position deviations are converted to mirror tilt angle by dividing them by the distance from the mirror to the beam profilier, which is 50 cm in this case. From the test result, we can find that all of these three sizes meet the requirement specified in the previous section, with the mirror tilt below 10^{-4} rad in 1 σ range after each release and return. Additionally, larger models show greater stability. Therefore, we ultimately selected the largest allowable size of the mirror holder for our experiment (limited by the size of the vacuum tank), which is the middle size with a side length of 5.5 cm.

Table 4.1 Standard deviations of beam spot position for different mirror holder sizes. The test is conducted with three different model sizes.

	side length [cm]	x distribution σ [rad]	y distribution σ [rad]
small	2.5	2.9×10^{-4}	3.4×10^{-4}
middle	5.5	6.0×10^{-5}	2.6×10^{-5}
big	8.5	1.6×10^{-5}	1.0×10^{-5}

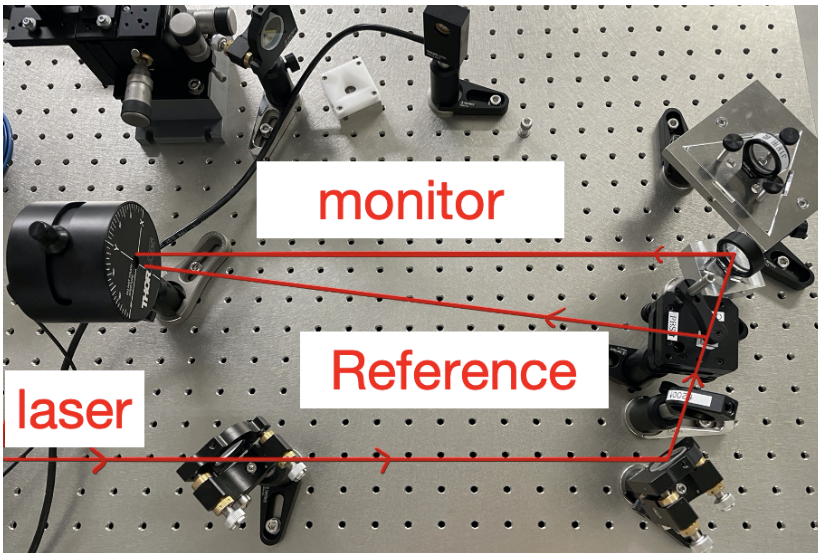

Fig. 4.11 Testing the stability of the mirror holder. The position of the reflected beam spot is monitored using a beam profiler.

Thirdly, we need to select suitable materials. When two extremely smooth metal surfaces come into contact, there is a risk of occurrence of a contact welding effect, which makes it difficult to separate them. Therefore, in our experiment, the mirror holder and the base need to be made of different materials: the mirror holder is made of aluminum, while the base is designed and tested using three different materials: PTFE (Teflon), TX-PET, and PE. The pictures of the samples are shown in Figure 4.13, and the test results are shown in Table 4.2. We can see that PE exhibits the least stability, while PTFE (Teflon) and TX-PET perform similarly. However, due to the higher compressive modulus of TX-PET, indicating its resistance to deformation, TX-PET was ultimately chosen in this experiment.

Table 4.2 Standard deviations of beam spot position for different materials. The test is conducted with three different materials. The side length of these three models are all 5.5 cm.

	x distribution σ [rad]	y distribution σ [rad]
PTFE	2.7×10^{-5}	3.2×10^{-5}
TX-PET	5.5×10^{-5}	4.5×10^{-5}
PE	$>10^{-4}$	$>10^{-4}$

4.3.3 Linear stage for mirror free falling

We employed a linear stage to achieve the release of the mirror. By specifying time and displacement information in the control program, we were able to control the linear stage

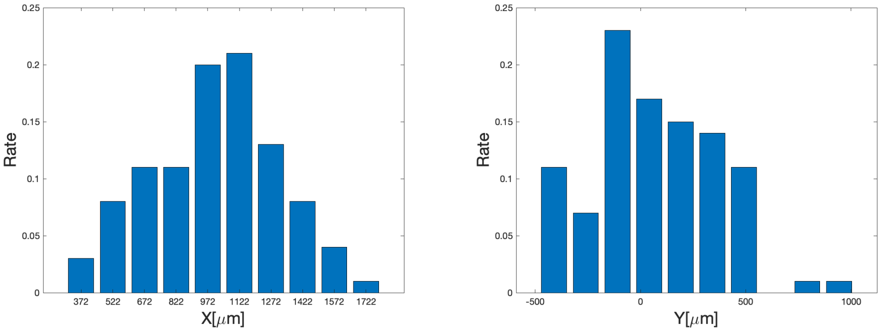

(a) x distribution (small)

(b) y distribution (small)

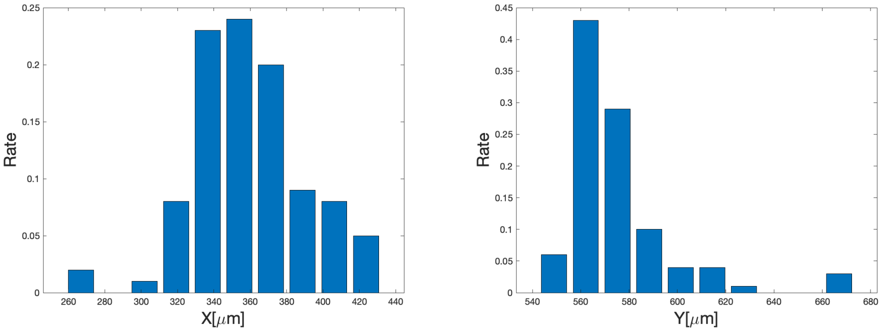

(c) x distribution (middle)

(d) y distribution (middle)

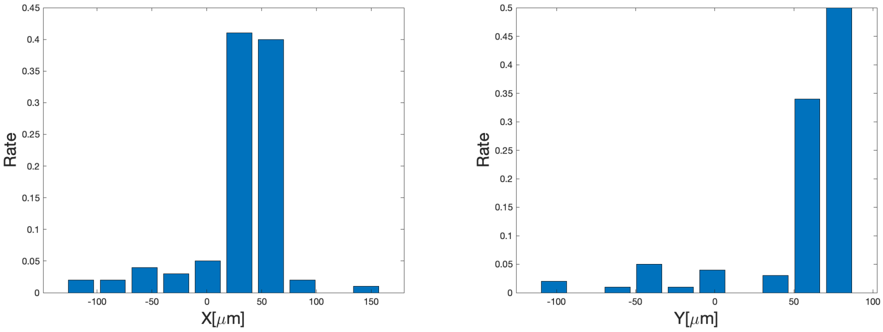

(e) x distribution (big)

(f) y distribution (big)

Fig. 4.12 Probability distribution plot of the beam spot positions. Three models of different sizes are tested for comparison: large (8.5 cm), medium (5.5 cm), and small (2.5 cm) triangle side lengths.

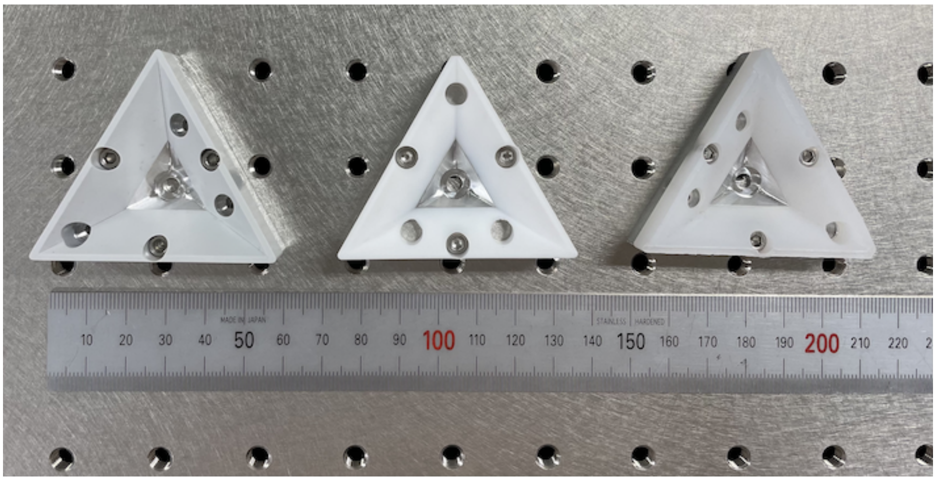

Fig. 4.13 Three candidate materials for the mirror base. From left to right are TX-PET, PTFE, and PE.

platform to move at the desired speed. The linear stage used in the experiment was custom-made by *Nikkidenso* [82], and some important parameters are provided in Table 4.3. Here, we emphasize two of the parameters. The max load of the linear stage is 4 kg, which requires the vacuum tank as well as the interferometer inside to be made compact and light. The position resolution of the linear stage is designed to be 0.1 μm. With this precision level, it is believed that the mirror release method described in the following text would be functional.

Table 4.3 Some designed parameters of the linear stage.

Parameter	Value
Size	457 mm×1440 mm×91 mm
Rated thrust	200 N
Maximum motor velocity	3 m/s
Maximum load	4 kg
Resolution	0.1 μm

Here, we demonstrate our method to realize the free-falling process. To start with, the mirror on top of the base is set on the linear stage platform, and then the up and down motion begins with the activation of the linear stage. Each moving cycle consisted of five steps:

1. The mirror is accelerated upwards together with the linear stage.
2. Upon reaching the midpoint, the linear stage is decelerated with a deceleration $a > g$, causing the mirror to separate from the base due to inertia.

3. The mirror undergos a free-falling motion, and the linear stage speed is controlled to follow the mirror's motion, while maintaining a constant distance between the mirror and the mirror base.

4. When returning to the midpoint again, the linear stage is decelerated, allowing the mirror to fall back into the base.

5. The mirror and linear stage are decelerated together and returned to the initial position.

In Figure 4.14, the solid and dashed lines represent the motion of the linear stage and that of the mirror, respectively. The interval from 0.25 s to 0.75 s corresponds to the free-falling phase of the mirror. For clarity, the gap between the stage and the mirror in the Figure is magnified, while in the actual experiment, this gap was less than 5 mm.

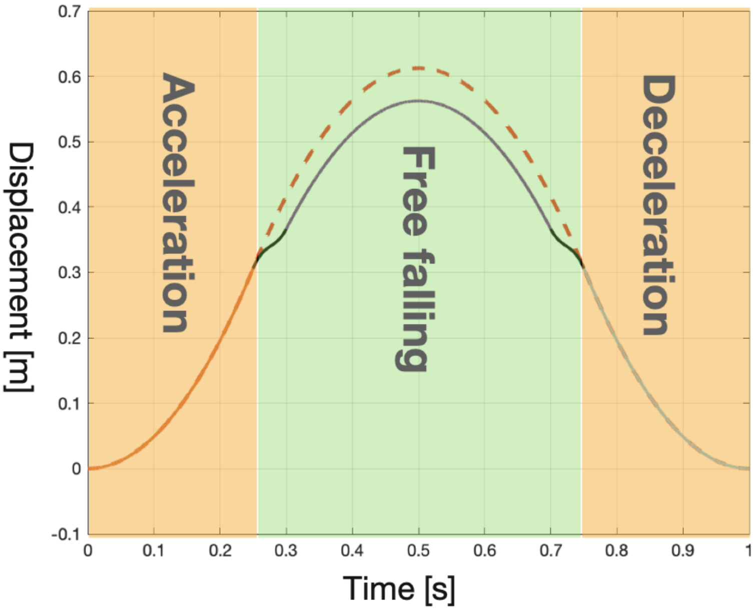

Fig. 4.14 One cycle movement of the linear stage and the mirror. The dashed line shows the mirror movement and solid line shows the linear stage movement. Here one cycle is set to be 1 s. The mirror is released at 0.25 s and returned at 0.75 s. The gap between the mirror and the linear stage is magnified in the figure for clarity.

4.4 Details of other devices

4.4.1 Vacuum tank

From Figure 4.4b, it is shown that the free-falling mirror is placed inside a vacuum tank. In fact, the mirrors (commonly referred to as test masses) of other earth-based laser interferometric gravitational wave detectors are also placed in a vacuum. The use of a vacuum environment is primarily aimed at reducing the Residual Gas noise.

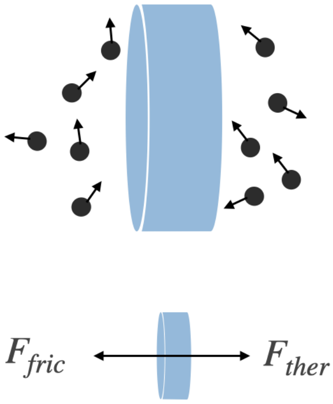

Fig. 4.15 Illustration of the forces exerted on a mirror by air molecules. The two forces are related to the thermal movement of the molecules and friction.

Residual Gas noise is generated by the gas remaining in the vacuum tank. Gas molecules randomly hit the mirror due to the thermal movement, causing the mirror to deviate from its equilibrium position. Meanwhile, the friction between air molecules and the mirror dissipates the mirror's kinetic energy, as shown in Figure 4.15. This process follows the Fluctuation-Dissipation Theorem [5]. The frictional force that hinders the mirror's motion is proportional to its velocity v and acts in the opposite direction:

$$F_{fric} = -bV = -\frac{1}{4}nA\mu\bar{v}v, \tag{4.7}$$

where A is the area of the mirror, $\mu = 28.9634\,\mathrm{g/mol}$ is the molar mass of air, and $\bar{v} = 4\sqrt{\frac{k_bT}{2\pi\mu}}\,\mathrm{m/s}$ is the average velocity of the air, with $K_b = 1.38\times10^{-23}\,\mathrm{J/K}$ the Boltzmann's constant. $n = \frac{P}{K_bT}$ is the number of molecules of gas per unit volume, where P is the pressure of gas and T is the temperature. The force on the mirror caused by the thermal movement of the molecules is denoted by F_{ther} and its power spectrum can be calculated according the Fluctuation-Dissipation Theorem [5]:

$$F_{ther}(f) = \sqrt{4k_BT\mathscr{R}(Z(f))}, \tag{4.8}$$

where the function $Z(f) = b + i\omega m$ is called the impedance, where b is the coefficient in Equation 4.7, ω is the angular frequency of the mirror's oscillation, and m is the mass of the

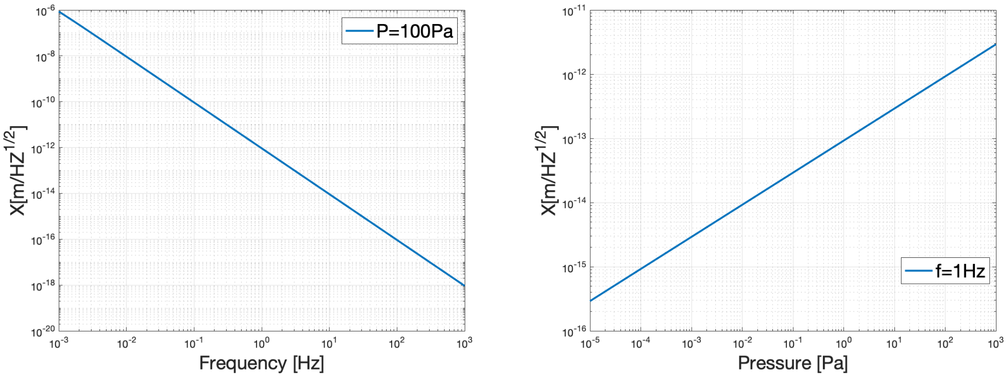

(a) Pressure fixed and frequency changing (b) frequency fixed and pressure changing

Fig. 4.16 Residual gas noise under the Fluctuation-Dissipation Theorem. The Temperature is 15 ^{o}C, the mirror mass is 0.03 kg, and mirror radius is 0.5 inch in the calculation.

mirror. The sign $\mathscr{R}$ means taking the real part. Then the equation of motion of the mirror in this system is:

$$m\ddot{x} = F_{ther} - F_{fric}, \tag{4.9}$$

where x is the mirror displacement and $\ddot{x}$ is the acceleration of the mirror under the two external forces. Substituting Equation 4.7 and Equation 4.8 into Equation 4.9 and conducting the Laplace transform, we obtain the power spectrum of the mirror displacement, which is also known as the residual gas noise:

$$x(f) = \frac{4k_B T b}{\omega^4 m^2 + \omega^2 b^2}. \tag{4.10}$$

Figure 4.16 shows the calculation results using Equation 4.10. We can see that x is inversely proportional to the square of the frequency and proportional to the square of air pressure, which means a lower pressure at higher frequency gives lower residual gas noise. Our experiment is conducted at a pressure level of approximately several hundreds pascals, which correspond to a residual gas noise of around $1 \sim 5 \times 10^{-12}\,\mathrm{m}/\sqrt{\mathrm{Hz}}$. This noise level is apparently not enough for gravitational wave detection but is enough for our principle verification experiment to illustrate the importance of vacuum implementation.

The vacuum tank design is shown in Figure 4.17. Acrylic was chosen as the material in order to see the interior as well as for its lighter mass. The size of the vacuum is also relatively compact, with a height of 100 mm and an inner diameter of 168 mm. The two valves on

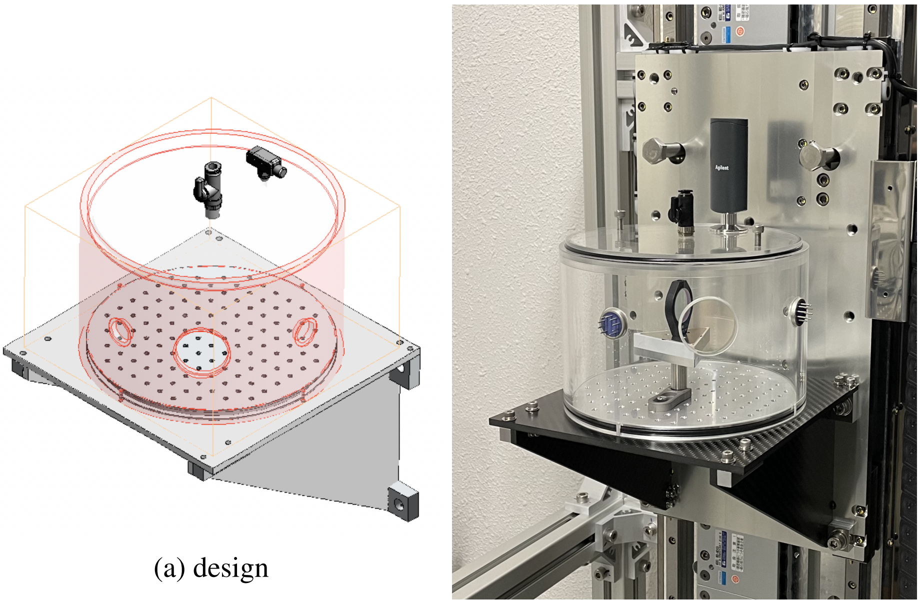

(a) design

(b) manufactured

Fig. 4.17 Vacuum tank and the platform. Acrylic is chosen for the vacuum tank in order to see the interior as well as for its low density. CFRP is chosen for the platform for its high strength and also low density.

top of the lid of the vacuum tank are connected to the vacuum pump and vacuum meter, respectively. The platform, on which the vacuum tank is placed, is made by CFRP (Carbon-fiber-reinforced polymers) and this material is also chosen for its comparable strength to Aluminum but with only one-third of the density.

When a mirror together with the mirror holder and base is placed inside the vacuum tank, it takes approximately 15 minutes to evacuate the tank from atmospheric pressure to 100 Pa. After closing the valve, the vacuum can be maintained at several hundred pascals for up to 24 hours. Since our equipment is not specifically designed for vacuum use, the outgassing from the components may affect the maintenance of vacuum level. However, as mentioned earlier, maintaining a vacuum level of several hundred pascals during the experimental process is already sufficient for the current step of this experiment.

4.4.2 Quadrant photon detectors

Quadrant photodiode (QPD) is used in this experiment for laser readout, as shown in Figure 4.4b. The sensitive area of the QPD is divided into four segments. By detecting the changes in light intensity in each segment, we can infer the movement of the light spot and determine the rotation of the mirror.

Due to the limited load capacity of the linear stage and the limited space inside the vacuum tank, we chose to place only the sensor head of the QPD inside the vacuum tank and connect it to the circuit through wires. The working principle of the photodetector is based on the excitation of electrons by photons, thereby converting the light energy into an electrical signal. The designed QPD operating circuit for this experiment is illustrated in Figure 4.18a. D1 $\sim$ D4 represent the four light-sensitive semiconductor diodes of the 4 segments of the QPD. The generated electrical signals pass through a low-pass filter composed of an operational amplifier (OP27), a 100 nF capacitor, and a 1.5 kΩ resistor to filter out signals above 1 kHz. Based on this circuit diagram, the board we soldered and used in the following experiment is shown in Figure 4.18b.

The spectrum of the laser intensity was measured using this QPD, as shown Figure 4.19. It can be observed that the four segments exhibited consistent performance, and when there was no laser incidence, the output of the QPD matched the background noise of the data logger. The spikes observed at 60 Hz and its harmonics are attributed to the current noise (This experiment is conducted in Nagoya where the 60-Hz AC power is used).

When measuring the laser output intensity using a photodetector, sometimes we observed spikes with a time duration of approximately 5 to 20 ms, as shown in Figure 4.20. Initially, we suspected that these spikes were due to temporally shorts of the circuits. However, similar spikes were detected using a commercial photodetector (*Thorlabs* PDQ30C), see Figure 4.20b. Furthermore, there were also occasions when one PD detected a spike while the other did not (see in Figure 4.20c and 4.20d), although they were conducting the measurement simultaneously. Additionally, when we replaced the laser or used an oscilloscope instead of a data logger to monitor the data, similar spikes were still observed. We were unable to identify the exact source of these spikes in the end. Fortunately, the occurrence frequency of these spikes is approximately once every few tens of seconds, which minimally impacts the data acquisition during our test.

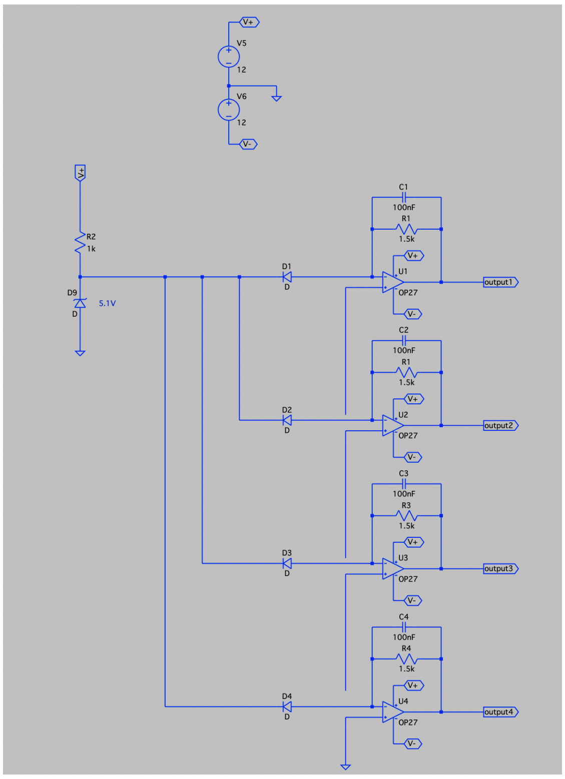
V+
V5
12
V6
12
V-
V+
R2
1k
D9
D
5.1V
D1
D
C1
100nF
R1
1.5k
V+
U1
OP27
V-
output1
C2
100nF
R1
1.5k
V+
U2
D2
D
OP27
V-
output2
C3
100nF
R3
1.5k
V+
U3
D3
D
OP27
V-
output3
C4
100nF
R4
1.5k
V+
U4
D4
D
OP27
V-
output4

(a) Designed operating circuit for QPD.

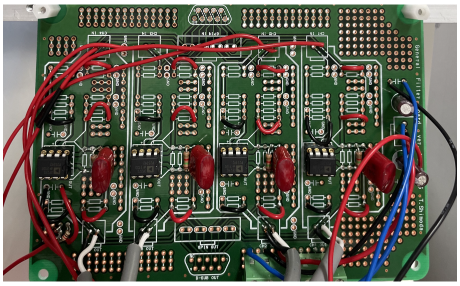

(b) Soldered board.

Fig. 4.18 Operating circuit for QPD. Each segment is connected to a 1 kHz low-pass filter before output.

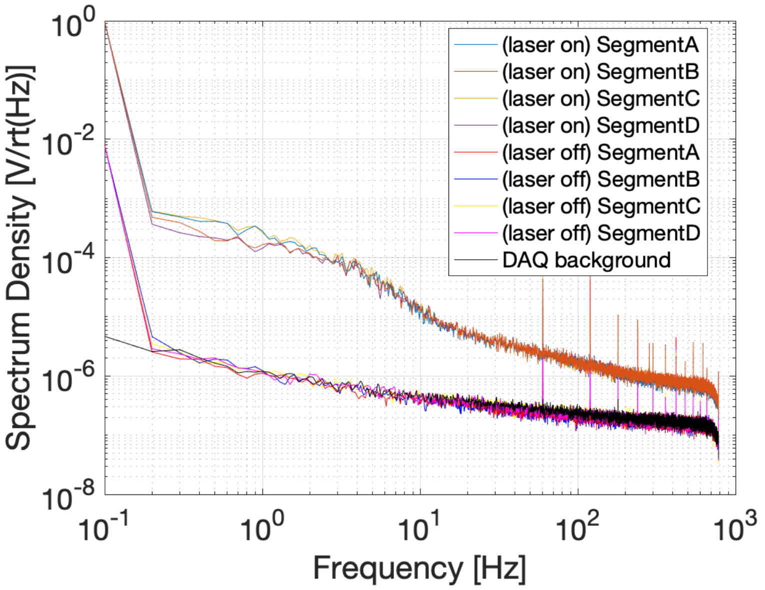

Fig. 4.19 Laser intensity spectrum measured with the four segments of the QPD. The lower lines are measured when the laser is off, indicating the background noise. The upper lines are measured when the laser is on. The sampling rate is 1.5k pnt/s.

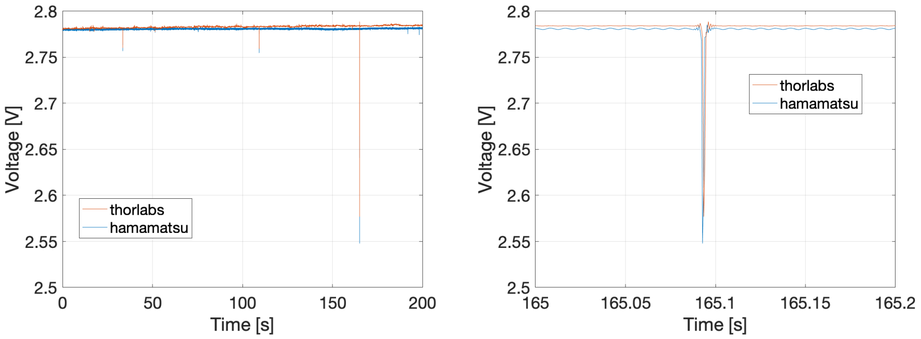

(a) full data (b) zoom in around t=165 s

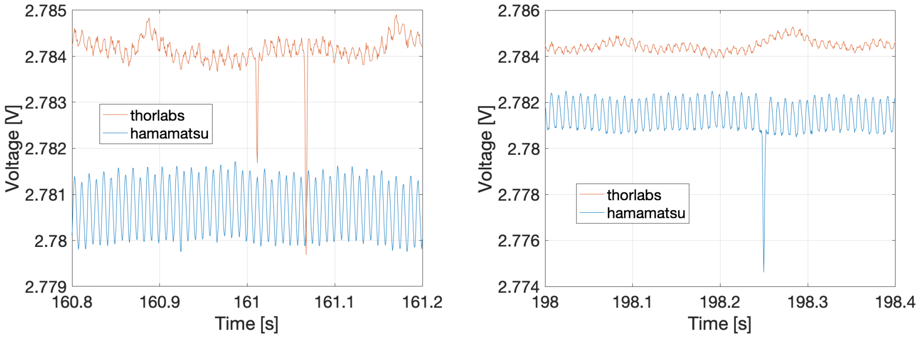

(c) zoom in around t=198 s (d) zoom in around t=161 s

Fig. 4.20 Unidentified spikes from the QPD outputs. Two photodetectors are used to measure the laser output simultaneously. (a), The spikes occur in the outputs of the photodetectors. (b), A spike occurs in the outputs of both at the same time. (c) and (d), Spikes measured at different time by different photodetectors.

Chapter 5

Main results and possible solutions for the disturbances

5.1 Linear stage movement

In Section 4.3.3, we mentioned that we need to control the moving speed of the linear stage to achieve the release and return of the mirror. Therefore, it is important to first ensure that the linear stage can successfully execute the desired motion as specified. Figure 5.1 presents the test results of the linear stage trial run, with the set values on the top and a comparison between the actual measured values and the set values on the bottom. The programmed moving pattern consists of three parts: 1. Accelerating upwards to the middle position, acceleration $a = -g$, with g the gravitational wave acceleration; 2. Ascending to the top and then descending, acceleration $a = g$; 3. Decelerating to zero reaching the bottom, acceleration $a = -g$. The duration of one cycle is set to 1s.

From the zoomed-in view on the right side of Figure 5.1, we find that the position control accuracy of the linear stage is worse than what was stated in the performance specifications (Table 4.3), with an error reaching the level of 10 micrometers. This may have an impact on the stability of the mirror during release. Meanwhile, it can be observed that the position signal of the linear stage exhibits a saw-tooth pattern. This is caused by the setting where the internal signal reading frequency of the linear stage is nearly twice the signal update frequency of the oscilloscope. The signal update interval is 8×10^{-4} s, while the signal reading time is approximately 4.4×10^{-4} s. As a result, the displacement signals at two adjacent time points are the same.

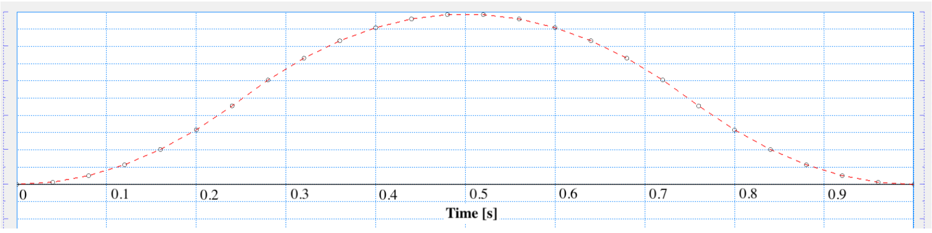

(a) setting data

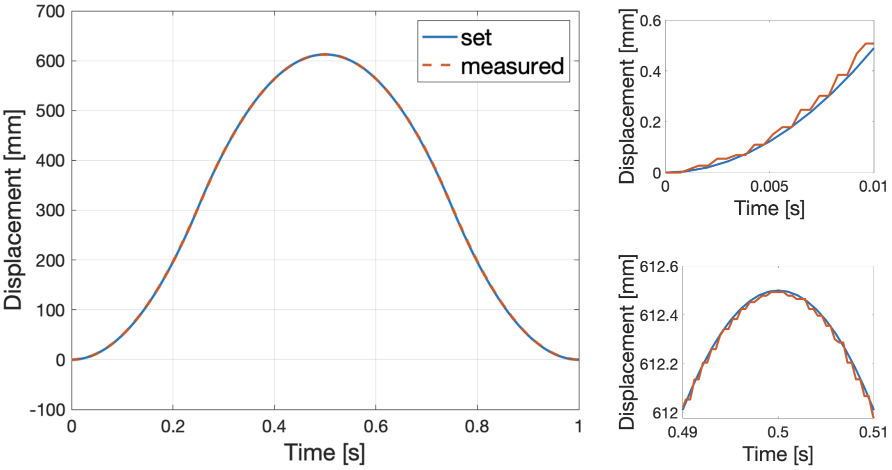

(b) measured data

Fig. 5.1 Linear stage trial run result. (a) Time-displacement coordinates set in the control program, forming an *acceleration* - *free fall* - *deceleration* motion process. (b) The results of the linear stage movement according to the programmed settings in (a). The two smaller plots on the right depict the zoomed-in views around the starting position and the peak. The error between the set values and the measured values is on the order of 10 micrometers.

5.2 Mirror release

5.2.1 Mid-release method

We first tried the method described in Section 4.3.3 to release the mirror, following the sequence of *acceleration* - *free fall* - *deceleration*. The expected result was that the mirror be released at the intermediate height during the motion, then go through free fall, finally return to the base and decelerate together with the linear stage until stop. This moving pattern is called the *mid-release* method. During the free fall of the mirror, the velocity of the linear stage was controlled to maintain a constant distance of 3 mm away from the mirror. For clarity, displacement-time graph of the desired motion is presented in Figure 5.2.

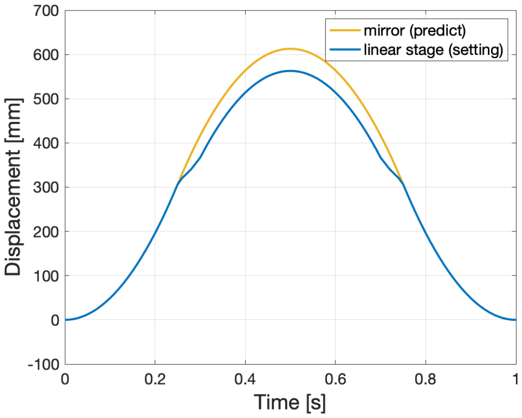

Fig. 5.2 Target movement of the *mid-release* method for the mirror and linear stage to realize the mirror free falling. The mirror is released at 0.25 s and returned at 0.75 s. The gap between the mirror and the linear stage is magnified in this figure for clarity.

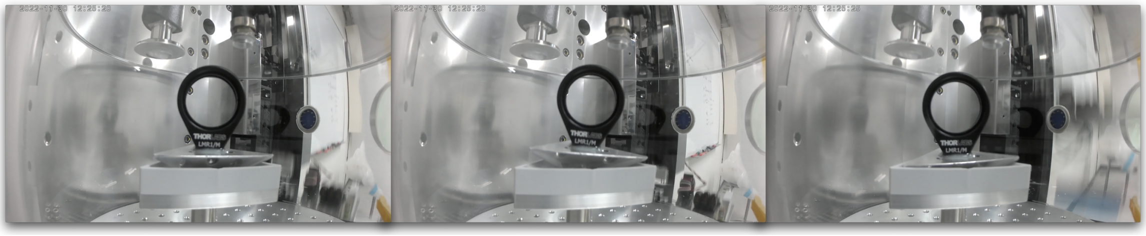

Fig. 5.3 Obvious tilting of the mirror using the *mid-release* method introduced in Section 4.3.3 and Figure 5.2.

The photographs capturing the motion of the mirror during the experiment using the *mid-release* method are presented in Figure 5.3. Obvious tilting of the mirror can be observed.

By reviewing the mirror motion videos, it was determined that the instability of the mirror was primarily caused by uneven forces acting on its three surfaces during the release process.

5.2.2 Top-release method

To achieve more stable release, adjustments were made as illustrated in Figure 5.4. The mirror is first moved together with the linear stage to the top position, then the linear stage is controlled to descent with an acceleration slightly greater than the gravitational acceleration g, causing the base separate from the mirror. This modified moving pattern is called the *top-release* method. In this scheme, the free-falling time of the mirror is reduced to half of the *mid-release* method, with only a quarter-second interval from 0.5 s to 0.75 s.

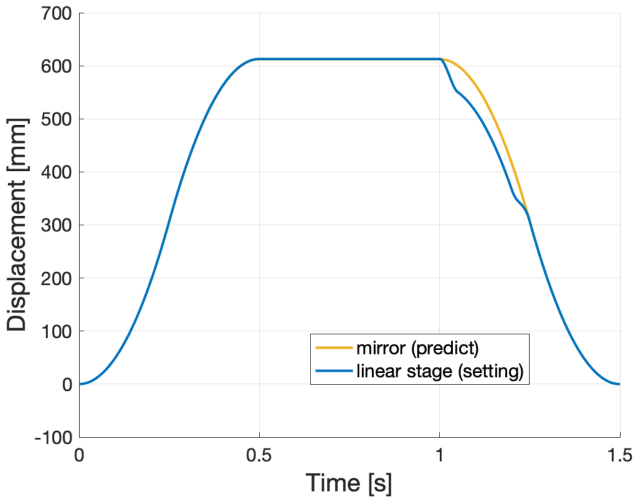

Fig. 5.4 Target movement of the *top-release* method for the mirror and linear stage to realize mirror free falling. The mirror is released at 0.5 s and returned at 0.75 s. The gap between the mirror and the linear stage is magnified in this figure for clarity.

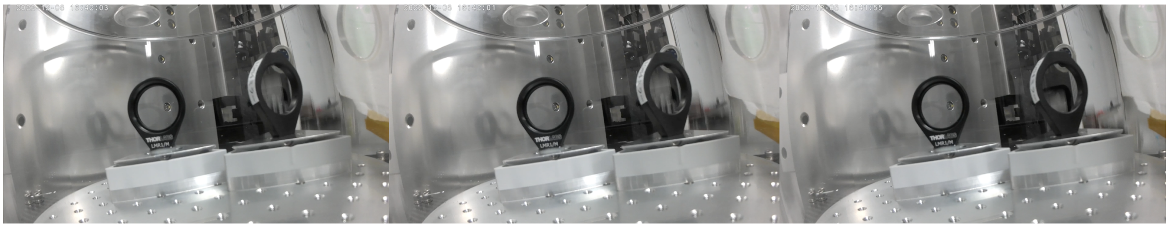

Fig. 5.5 Successfully released the mirrors with no obvious tilt using the *top-release* method. Two mirrors are placed in the vacuum tank to confirm whether the difference in position affects the release of the mirrors.

The photographs capturing the motion of the mirror during the experiment using the *top-release* method are presented in Figure 5.5. We can see that this time the mirror was successfully released and no obvious tilt is observed. The *top-release* method is consistently conducted in our subsequent tests.

There is one additional detail to mention regarding the testing of the *top-release* method. The principle of achieving mirror release involves controlling the linear stage to have a slightly greater acceleration than the gravitational acceleration g. This is achieved in the control program by setting the gap between the mirror and the stage, as well as the time taken to reach this gap (release time). However, an excessively large acceleration can overload the linear stage, while too small an acceleration can hinder the release of the mirror. After a series of testing, a gap size of 1 mm and a release time of 30 ms are selected as the optimal releasing parameters.

5.3 Device performance characterizing

Next, we used the laser and QPDs to observe the movement of the mirror more precisely and then analyze the sources of noise that affect the stability of the output signal.

5.3.1 Testing without free-falling mirrors

Firstly, without using a reflection mirror, we directly measured the intensity of the laser using the QPDs at distances of $\sim$5 cm and $\sim$15 cm from the light source. The measurement results are shown in Figure 5.6 (left: overall motion, right: zoomed-in view). The red curve represents the motion of the linear stage, which initially remains stationary, then ascends and descends at a constant velocity, followed by repeated cycles. Based on Figure 5.4, the following conclusions can be drawn:

- During the linear motion phase with constant velocity (12 - 24) s, oscillations with a frequency of approximately 1 Hz and an amplitude of about 2 mV were observed in the dark-blue line. This can be attributed to the vibration mode of the entire vacuum tank. Additionally, significant variations in light intensity and ringdown effects were observed when the linear stage changes moving directions. This ringdown is mainly originated from the vibration of the fiber output and can be explained by Figure 5.7. We tapped the post, on which the fiber is fixed, and compared the laser output fluctuation, which also shows a ringdown curve, with the ringdown observed during the movement. Similar frequency is found in the two curves, which suggests that they are originated from a common source.

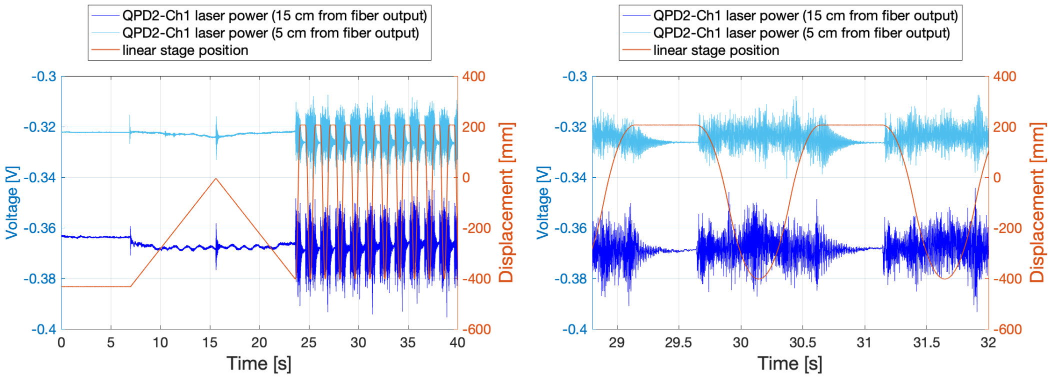

(a) overall (b) zoom in

Fig. 5.6 Directly incident laser beam on the QPD. The red line shows the linear stage's movement. The light-blue plot represents the measured output from one segment of the QPD when the QPD is ∼5 cm away from the fiber output port, and the dark-blue plot represents the measured output from the same segment when the QPD is ∼15 cm away from the fiber output port. Both of them are the output from one segment. Figure (b) is the zoomed-in view of Figure (a) from 29 s to 32 s.

However, there are other frequencies and other oscillations mixed in the output when the linear stage is moving, indicating that there are other sources needed to be clarified.

- During the *top-release* cycles (after 24 s), the dark-blue line is found to have greater noise than the light-blue line, which can be attributed to the vibrations of the fiber and the vacuum tank, since the light-blue line is measured near the fiber output port, and therefore has less differential oscillation with the fiber output port. During the 0.5-second stationary period at the top, the laser intensity experienced a ringdown before stabilizing. It can be observed that the laser intensity after each release cycle does not have obvious change, indicating that the mirror returned to its initial position, consistent with the testing conducted in Chapter 4.

5.3.2 Detecting transmitted and reflected light from a beam splitter

Next, we fix a beam splitter on the mirror holder and let it move together with the linear stage. We then measured the reflected and transmitted light passing through the beam splitter using the QPD. The experimental setup is illustrated in Figure 5.8. The pressure inside the vacuum tank was set to be 100 Pa. Before the movement, the laser beam was centered on the QPD. The output difference between the four segments was within 20 mV. Specifically the outputs of segment A, B and D are ∼ 180 mV and the output of segment C is ∼20 mV lower than the others. Figure 5.9 shows the variation in the reflected light intensity for each segment

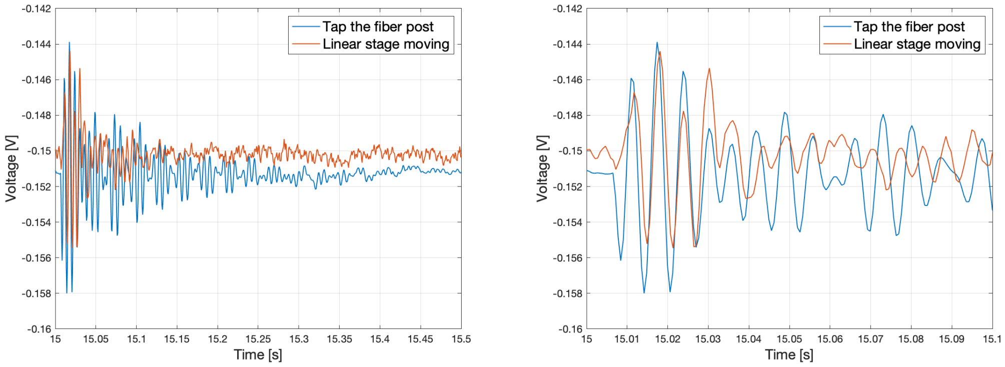

(a) (b)

Fig. 5.7 Ringdown of the QPD output. The red line represents the measured output from one segment of the QPD when the linear stage is moving, and the blue line represents the measured output from the same segment when the fiber post is tapped. Similar ringdown frequency is found in the two curves.

as the linear stage moves and two zoomed-in plots on the right are shown as examples. By examining this figure, we observed the following:

- When the mirror is released and free falling, it undergoes tilt, resulting in the movement of the beam spot on the QPD. In the bottom right plot in Figure 5.9, the mirror is release around 28.75 s and after the release, the output of segments A and B increased, while the outputs of segments C and D decreased. This suggests that the beam is moving towards the left side of the QPD. To be more precise, Segment D's output changes from -180 mV to -55 mV, indicating a movement distance of approximately two-thirds of the beam radius. Giving the beam radius (R = 0.65 mm) and the distance between the QPD and the beam splitter (L = 50 mm), we can calculate that the maximum rotation angle of the mirror, around the yaw-axis, reaches $\theta = R \times \frac{2}{3}/50 \sim 8\times10^{-3}$ rad. In some other cases, such as the one on the upper right in Figure 5.9, the beam spot movement is relatively small, which is approximately one-tenth of the beam radius. The maximum tilt angle is estimated to be around 1.3×10^{-3} rad, which is close to the upper limit calculated in Section 4.3.1. But further stabilization is still needed. Also, although the rotation around the pitch-axis is relatively smaller compared with the yaw-axis, giving the evidence that the output difference of segment A and B is changing within 10$\sim$30 mV, it is still needed to be stabilized.

- When the mirror is in the air, the output light exhibits both high-frequency and low-frequency oscillations. From the two zoomed-in plots in Figure 5.9, we can see that high-frequency oscillation is approximately 200 Hz, which is believed to originate from the overall vibration of the linear stage. The low-frequency oscillation is approximately 10 Hz, which is suspected to be caused by the vibration of the platform, on which the vacuum tank is placed. However, these two oscillation sources still need further verification.

5.3.3 Vacuum level and mirror release

So far, the influence of residual gas noise calculated in Section 4.4.1 on our experiment has been significantly smaller than the instability observed when the mirror is released. However, this experiment still requires a certain level of vacuum, as explained in the following.

If the mirror is well released, the output of the QPD would be like the two plots on the right in Figure 5.9. During the free-falling region, the power of each segment should change continuously with some small oscillations caused by the vibration of the experimental system and there will not be sharp decrease or increase. In order to see how the vacuum level influences the mirror release, We conducted mirror release tests at pressure levels of 100 Pa, 300 Pa, 500 Pa, and 1000 Pa. The measured result is shown in Figure 5.10 and the data shown here is obtained from one of the mirror release cycle. The thick red solid line represents the position of the linear stage, with the time interval from 33.80 s to 34.05 s indicating the setting time for the mirror to be released and undergo free fall. The thinner solid lines show variations in reflected light intensity from the mirror under different pressure conditions, with significant fluctuations indicating substantial oscillation when the mirror returns to the base. It can be observed that at 100 Pa and 300 Pa, the output is changing continuously during the free-falling period. The mirror's return time aligns closely with the set time, precisely 0.25 seconds of free fall starting from the separation at 33.80 s. However, for the case of 500 Pa and 1000 Pa, there are sharp increase and decease in the QPD output, which means that the mirror is not well released. And to be more precisely, it can be seen that at 500 Pa, the mirror's return time is noticeably advanced by approximately 0.05 s, and at 1000 Pa, the mirror returns to the base in less than 0.1 s with significant shaking afterwards. Therefore, our current experimental requirements dictate a pressure of at least 300 Pa or lower. To determine the required vacuum level more precisely, a need for further investigations on the quantitative criteria remains.

5.4 Main disturbances and possible solutions

Using the *top-release* method, we have successfully achieved the release of the mirror and maintained its stability to some extent during free fall. However, there are still several issues that need to be addressed to achieve better stability and maintain alignment. The factors currently affecting the stability of the mirror during free fall primarily originate from two

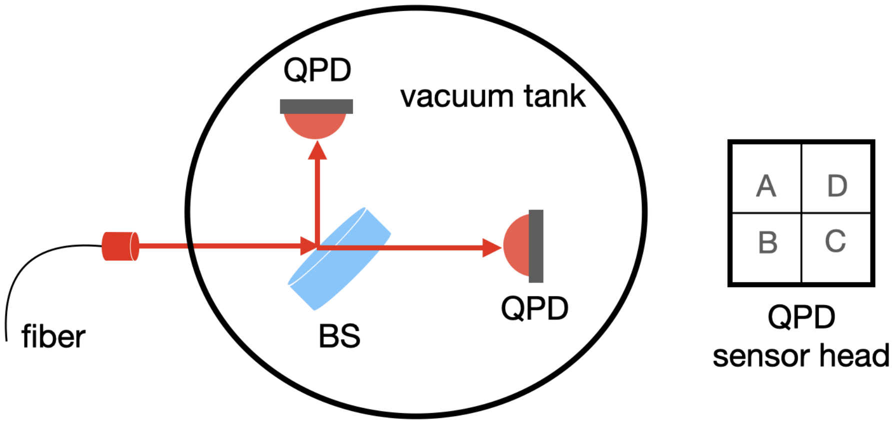
QPD
vacuum tank
fiber
BS
QPD
A
D
B
C
QPD
sensor head

(a) design setup

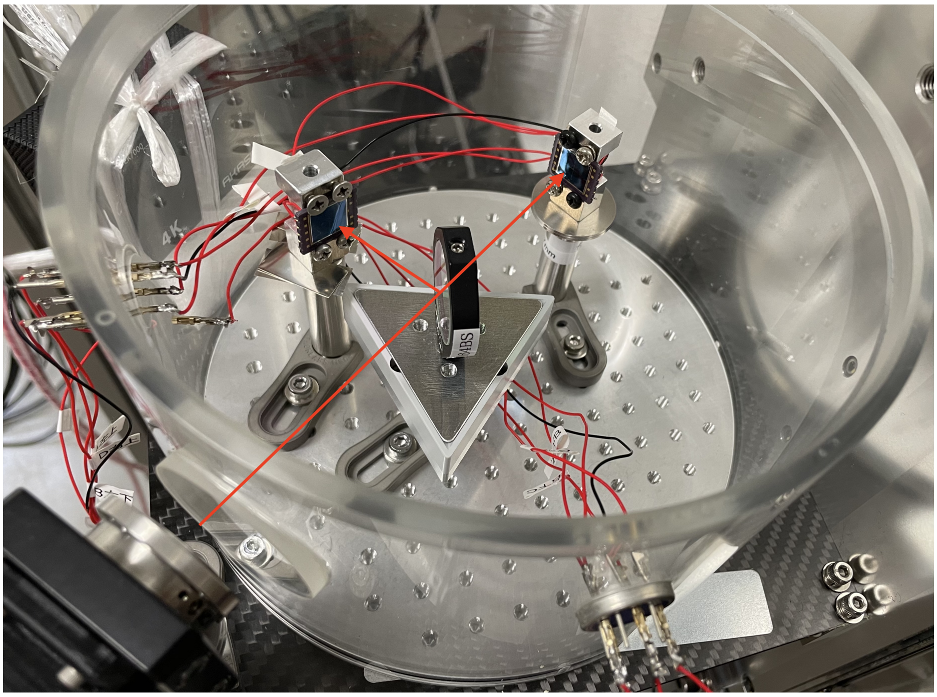

(b) actual setup

Fig. 5.8 Detecting transmitted and reflected light from a beam splitter.

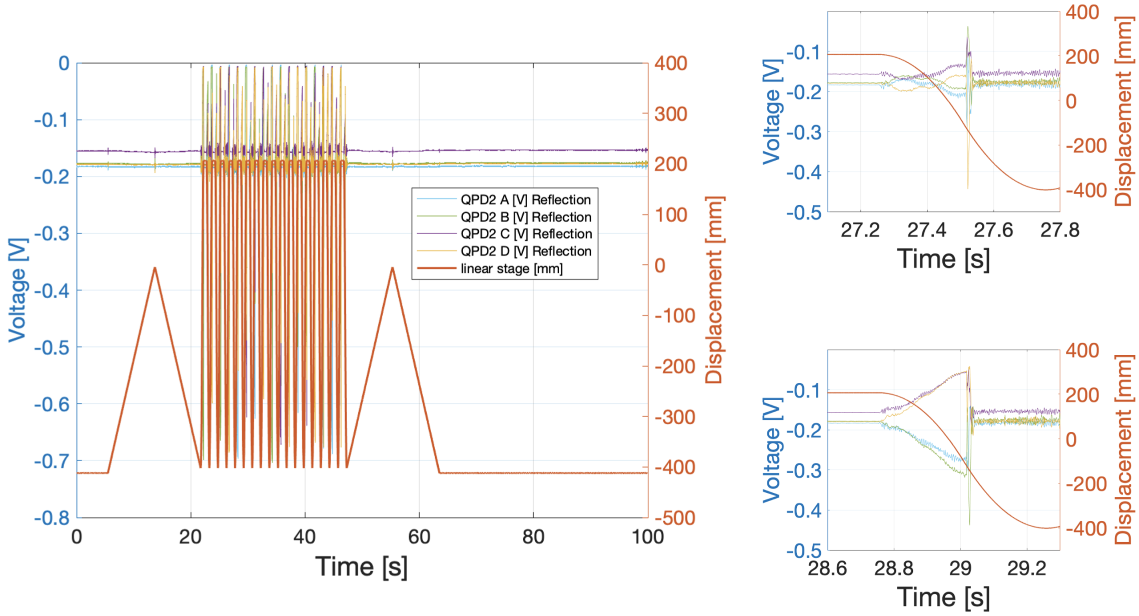

Fig. 5.9 Reflected light intensity for each segment of the QPD as the linear stage moves. The two zoomed-in plots on the right shows the intensity change details when the mirror is released.

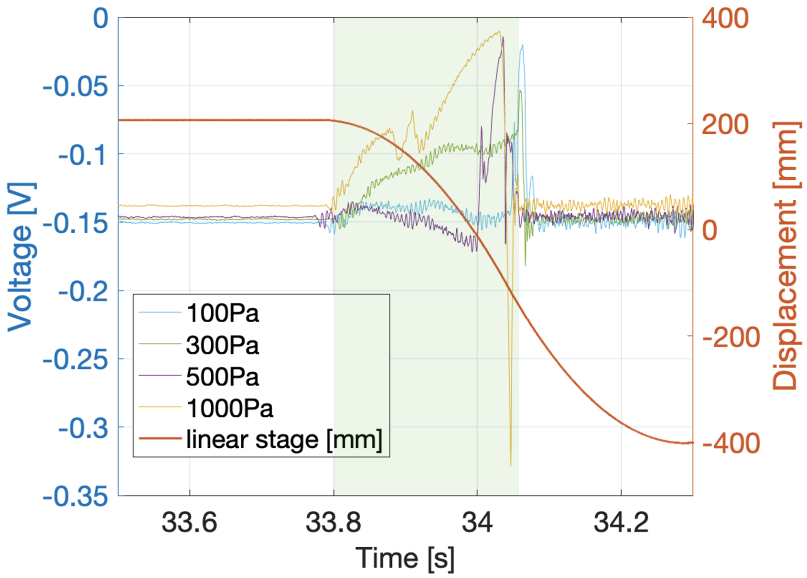

Fig. 5.10 Variation of reflected light with the movement of the linear stage under different pressure conditions. Significant fluctuations in light intensity indicate substantial oscillation when the mirror returns to the base. Pressure levels below 300 Pa are necessary to ensure that the mirror experiences 0.25 seconds of free fall, which is the setting in the control program.

aspects: the vibration of the linear stage during its motion, which leads to oscillation of the fiber and vacuum tank, and the uneven forces exerted on the mirror during release, resulting in tilt of the mirror. To address these disturbances, solutions are proposed in the following.

5.4.1 Linear stage vibration

The vibration of the linear stage couples to the fiber and the vacuum tank. Firstly, we have utilized a clamp at the fiber output to mitigate the fiber dithering. The implementation of the clamp has reduced the output fluctuation by approximately half, see in Figure 5.11. The clamp is also employed in the testing described in section 5.3.

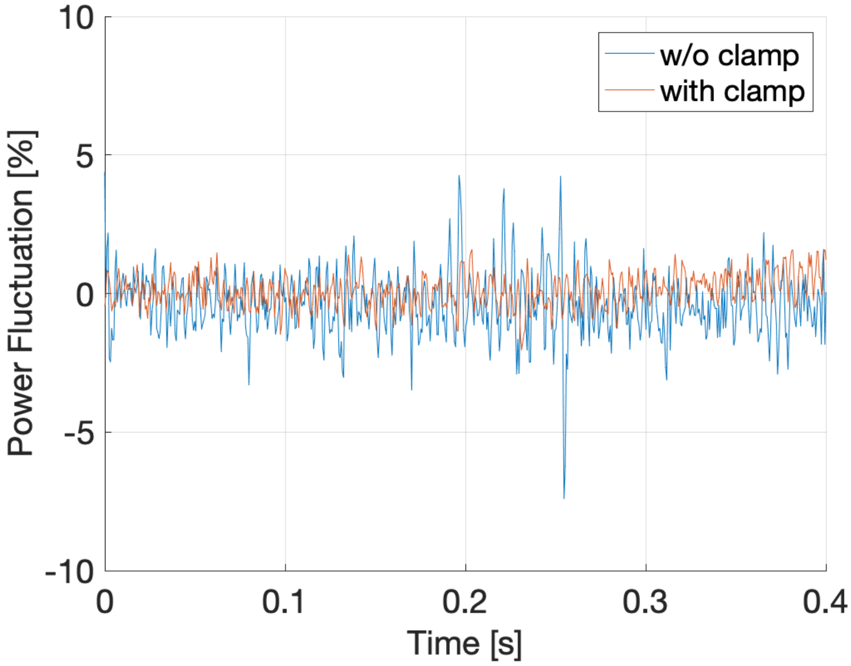

Fig. 5.11 Laser power fluctuation when linear stage is moving. The vertical axis shows the power fluctuation, which is the proportion of the intensity variation to the total intensity. With a clamp on the fiber output port, the fluctuation decrease is substantial.

To further mitigate fiber dithering, the laser beam can be injected to a mode cleaner before entering the interferometer. The fiber's dithering can cause beam displacement, resulting in the introduction of higher-order modes (such as Hermite Gaussian 01 or Hermite Gaussian 10 modes) in the optical cavity. The mode cleaner helps removing these higher-order modes and thus eliminating the effects from laser's dithering. However, as this dithering originates from the linear stage, in order to prevent it from coupling into the mode cleaner, the mode cleaner itself should also be released for free fall during data acquisition. Also, the build-up time for the mode cleaner should be much smaller than the mirror free-falling time. Here, we take the mode cleaner of Advanced LIGO as an example [13]. The designed input mode cleaner round trip length of Advance LIGO $L = 32.9$ m and the finesse $F = 500$. Then the build-up time is $t = LF/c = 5.48 \times 10^{-6} s$, which is small enough to be ignored. Here, c represents the speed of light. It is important to note that the fiber's deformation due to vertical motion can induce changes in laser intensity and polarization, which is temporarily disregarded in this experiment since they are not dominant at the current stage.

Secondly, the overall vibration of the vacuum tank can also be addressed through the use of a mode cleaner and free falling not only the mirrors but also the photodetectors. This approach effectively isolates the light source and interferometer from the vacuum tank during the free-falling cycle. However, we have not considered the excitation of eigenmodes of the mirror. If such vibration becomes prominent in the noise, it could potentially be mitigated by installing dampers.

5.4.2 Mirror movement caused by release

Mirror movement include displacement and tilt. Mirror displacement caused by the release is discussed in 2.2, and can be dealt with using the detrend method. To decrease mirror tilt during the free-falling cycle, the release method should be updated. The utilization of piezoelectric ceramics (PZT) could help to achieve more precise control. By installing PZTs on the base of the mirror, the release can be achieved by the contraction of the PZT, which can be accurately controlled based on the voltage applied at its two ends.

After the implementation of PZT, if there is still small amount of mirror tilt, there are two ways to deal with it. On one hand, the mirror tilt can be measured individually by extra QPDs and subsequently subtracted from the final data, as illustrated in Figure 5.12. The transmitted light power from M1, measured by P5, indicated the tilt of the beam splitter. Then the reflected power from the beam splitter's surface is measured by P3 and P4. Subtracting P5 from P3 and P4, the tilt signal of the two end mirrors can be obtained. Finally, the mirror tilt effects can be extracted from the interference results (P1 and P2). The gravitational wave signal is reserved together with the mirror initial displacement, which can be solved by the detrend method.

Additionally, by combining modulation-demodulation techniques, it may be possible to obtain the mirror's tilt information from the interferometer. Then the mirror tilt can be subtracted from the measured interfered signal or used as a feedback control signal to calibrate the tilt of the mirror.

Here, we consider the tilt of two end mirrors as two modes: differential mode θ_d and common mode θ_c, with differential modes representing the opposite tilt directions of the two

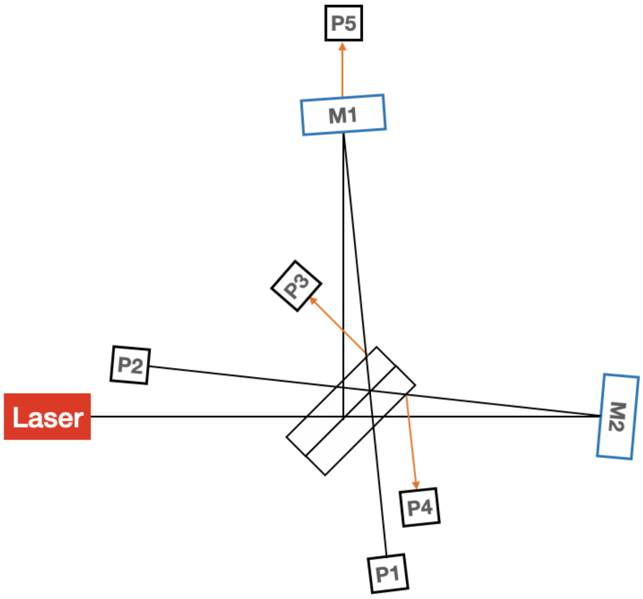

Fig. 5.12 Five QPDs used to obtain mirror tilt information. P5 gives the tilt of the beam splitter. (P3−P5) and (P4−P5) then give the tilt information of the two end mirrors.

mirrors (one tilting clockwise while the other tilting counterclockwise) and common mode representing the same tilt direction of both mirrors. The common mode and differential mode of the end mirrors result in displacement and misalignment of the spot on the photodetector, as shown in Figure 5.13. To facilitate distinction, red and yellow colors are used here to represent the two beams reflected back from the end mirrors.

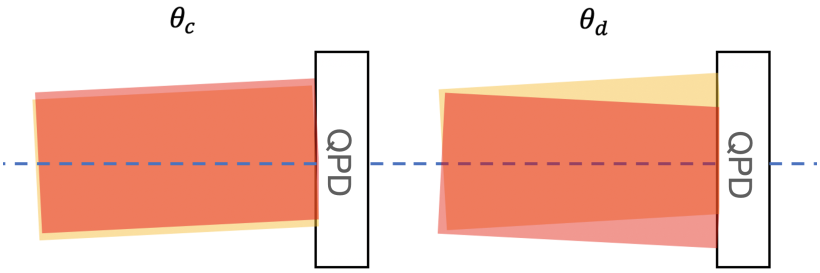

Fig. 5.13 Tilt beams resulting from mirror tilt. θ_c on the left is produced by the common mode tilt of the mirrors and θ_d on the right is produced by the differential mode tilt of the mirrors. To facilitate distinction, red and yellow colors are used here to represent the two beams and a slightly misalignment is introduced in θ_c to show two beams.

When the tilt of both mirrors is in the common mode, the spot on the QPD undergoes displacement, producing the x-diff signal ($P_{\mathrm{x-diff}}$), which represents the difference in light intensity between the left and right sides of the QPD. When the tilt of both mirrors is in the differential mode, the phase difference of the reflected light's wavefront changes, which would result in the interference status change. Near the middle fringe, this leads to half of the spot becoming brighter while the other half becomes darker, thereby generating $P_{\mathrm{x-diff}}$ signal. However, near the bright fringe, both sides of the spot simultaneously become darker, resulting in no $P_{\mathrm{x-diff}}$ signal. Combining both cases, we observe that the $P_{\mathrm{x-diff}}$ signal near the bright fringe reflects the displacement of the spot, i.e., the common mode of the two mirrors.

To observe the differential mode, we can analyze the modulation-demodulation signal. Here, we utilize the phase-intensity diagram of the interference light for better understanding. As analyzed in Chapter 2, the variation in interference light follows a cosine curve, while the modulation-demodulation signal follows a sine curve, as shown in Figure 5.14. Near the bright fringe, the slope of the interference light signal is zero, while the slope of the modulation-demodulation signal is at its maximum, indicating that the difference in modulation-demodulation signal between the left and right sides of the QPD ($V_{\mathrm{x-diff}}$) can reflect the differential mode.

Similarly, near the middle fringe, the slope of the modulation-demodulation signal is zero, indicating insensitivity to the differential mode. Therefore, $V_{\mathrm{x-diff}}$ near the middle fringe reveals the common mode of the mirror. The differential mode at this point needs to be considered in combination with $P_{\mathrm{x-diff}}$. The summarized conclusions are presented in Table 5.1.

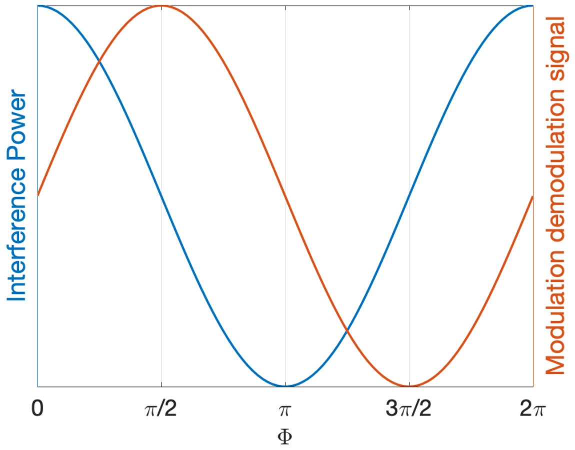

Fig. 5.14 Fringe intensity and modulation-demodulation signal changing with phase. The fringe intensity follows a sine curve and the modulation-demodulation signal follows a cosine curve.

Table 5.1 Extraction of mirror tilt signal from QPD signals. "+" means signal can be measured and "0" indicates absence of signal. Around the bright fringe, P_{x-diff} shows the common mode θ_c and around the middle fringe, V_{x-diff} shows the common mode.

	@ Bright fringe	@ Middle fringe
common mode θ_c		
$P_{\mathrm{x-diff}}$	+	+
$V_{\mathrm{x-diff}}$	+	+
differential mode θ_d		
$P_{\mathrm{x-diff}}$	0	+
$V_{\mathrm{x-diff}}$	+	0

Chapter 6

Conclusions and future works

Based on the insight of improving the sensitivity of the earth-based gravitational wave detectors at lower frequencies (0.1< f <10 Hz), JIFO proposes the repeated release of the test masses to achieve free-falling movement. This design can totally decouple the test masses of the detector from the seismic noise and suspension thermal noise, which are dominant noises for the earth-based gravitational wave detectors at lower frequencies.

This thesis investigates the concept and data features of a JIFO, develops the data readout method, and discusses data analysis method with regard to the data features. Based on the improvement in the sensitivity by utilizing the "juggled" technique, several promising science cases for JIFO are discussed, which are of valuable insight into cosmology and the gravity theory. The first JIFO prototype was built from scratch without prior experience in this research. The mirror release method was developed and tested using a linear stage and other specially designed devices. Finally, the disturbances of the prototype are evaluated, and a series of feasible improvements are proposed.

6.1 Conclusions

In Chapter 1 of this thesis, the basic theory of gravitational waves and their detection are introduced, followed by some details of the noise in the detectors. It is pointed out that mitigating seismic noise and suspension thermal noise is the key to improving the sensitivity of the detectors, and JIFO is one of the novel types of gravitational wave detectors that deal with these two sources of noises.

In Chapter 2, the basic configuration and data features of JIFO are discussed. Compared with a standard interferometric gravitational wave detector, JIFO utilizes repeatedly free-falling test masses, and thus obtains discontinuous data with different initial effects for each free-falling cycle. The detrend method, which subtracts a linear fitting from the measured data, as well as the templates used for matched filtering, could solve the problem of different initial effects. On the other hand, since it is hard to do fringe locking of the interferometer, while the test masses are free falling, we present a data readout method for JIFO, which uses both the interference laser power and modulation-demodulation signal to form a complex function. This method allows for obtaining the mirror displacement signal of the interferometer independent of the fringe, resulting in a fringe-independent SNR equivalent to half of that around the dark fringe. As for the additional Newtonian noise introduced by the up-and-down motion of the interferometer, it is calculated that an inhomogeneity in the mass distribution of less than 10 mg within 1 m is required to mitigate its impact. Meanwhile, the Newtonian noise as well as gravitational wave signals at much lower frequencies can be upconverted to the sidebands of the interferometer motion frequency. This feature offers a possibility for the JIFO to serve as a Newtonian noise meter and to detector low-frequency gravitational wave signals in the sidebands at higher frequencies. Further investigations in this area are necessary in the future.

The promising science cases are presented in Chapter 3. Assuming a JIFO with identical displacement noise as ET, it is found that the sensitivity of JIFO surpasses ET significantly at frequencies lower than $\sim$2.5 Hz, owing to the free-falling test masses. This sensitivity improvement enables the detection of the following gravitational waves signals.

1. Quasi-normal modes from massive black holes, which are an important step for the merger of binary black holes. It is calculated that black holes weighing around $10^4 \sim 10^5 \mathrm{M}_\odot$ at a distance z=1 can produce quasi-normal modes with a central frequency below 2 Hz. These gravitational wave signals can be detected by JIFO, while they cannot be detected by ET.

2. Gravitational waves from BH-NS binaries below 2 Hz, which can be used to test BD theory. Our calculation using the expected sensitivity of JIFO gives a lower bound for the BD parameter $\omega_{BD} > 8.8 \times 10^4$.

3. Gravitational waves, originating from density fluctuations in the early stage of the universe, which give a hint for primordial black hole – dark matter scenarios. This thesis adopts an assumption that the primordial perturbation is a delta function and calculates the related primordial gravitational waves peaking at 1 Hz. This signal can be detected by JIFO with a 1-year correlation but is still beyond the ET's detection ability.

In Chapter 4, the work on principle verification experiment is introduced. A linear stage is used to achieve the up-and-down motion of the interferometer. To avoid moving the laser, the laser beam is coupled into the fiber in advance with a coupling efficiency of $\sim$64%. A triangle-shaped mirror holder is designed and tested to ensure that the mirror can be released by controlling the acceleration of the linear stage and return to its initial position automatically. After a series of tests, a model with a side length of 5.5 cm, made of TX-PET material, was determined as the final design. Due to the load limitations of the linear stage, the mirrors are set inside a vacuum tank with a diameter of 16.8 cm. Also, to save space inside the vacuum tank, the self-made operating circuit board for the QPDs is placed outside the tank.

Chapter 5 presents the main results of the experiment and discusses some possible solutions to overcome the current problems. The *top-release* method, in which the linear stage stops at the top position and then is controlled to move downwards, is verified in releasing the mirrors successfully while maintaining a certain tilt angle of the mirror in the air. However, from the measurement results, even the smaller rotation angles reach 1×10^{-3} rad, which is ten times larger than the requirement for a clear interference fringe contrast. Since it is not easy to improve the control accuracy of the linear stage, we may need to update the mirror holder design to realize a more stable release. Meanwhile, the oscillation of the linear stage coupled to the vacuum tank and the fiber is recognized to be the main reasons of the fluctuations of the laser output. This also needs to be addressed in the future works.

6.2 Future works

The future works include the following:

- Data analysis method. In the discontinuous data of JIFO, there is unwanted linear component caused by the initial position and velocity of each free-falling cycle. The detrend method is developed to subtract this linear component from the data, but at the same time, a linear part of the gravitational wave signals buried in the data are also subtracted. In the future work, we can explore two possible approaches. First, the matched filtering method can be applied using detrended gravitational waveform templates to show its effectiveness with the detrended data. Alternatively, a re-trend method can be developed to restore the detrended gravitational wave signals back to the original state before the detrending process.

- Signal upconversion of JIFO. Due to the cyclic movement of the JIFO ($f = f_c$), the mirror's displacement signal ($f = f_m$) can be converted to sidebands around f_c, which is $f_c \pm f_m$. This gives a chance to detect low-frequency noises, such as Newtonian noise, or low-frequency gravitational wave signals at higher frequencies, where the detectors have better sensitivity. This approach requires further quantitative studies. For example, based on the sensitivity curve of the ET, it is of interest to calculate the intensity of a 1-Hz Newtonian noise upconverted to 100±1 Hz. This calculation helps determine whether the upconverted noise can be detected and provide the resulting SNR. Similar calculations are needed for gravitational wave signals at low frequencies.

- Experiment update. In the principle verification experiment, the mirror release was not stable enough. To mitigate the mirror tilt after release, we are considering connecting the mirror holder with PZTs and realizing the mirror release by controlling the length of the PZTs. By free falling not only the mirrors but also the photodetectors and utilizing a mode cleaner can decouple the linear stage vibration from the output. Furthermore, the residual noises can be monitored by extra QPDs and be compensated with a feedback control method or subtracted from the raw data. In addition to the update aimed to stabilize the output during mirror's free-falling motion, there is another perspective, which is to shorten the free-falling time so that all the displacement signals are small enough. This can be achieved by utilizing high-speed PZTs to kick the mirrors, and the free-falling time can be limited to be millisecond scale.

As a final conclusion, it is demonstrated that significant advancements in scientific achievements can be achieved by the juggled interferometer, and the technical challenges of the juggled interferometer are identified and a path towards realization is presented.

References

[1] Albert Einstein. Approximative integration of the field equations of gravitation. *Sitzungsber.Preuss. Akad. Wiss. Berlin (Math. Phys)*, pages 688–696, 1916.

[2] LIGO Scientific Collaboration and Virgo Collaboration. Observation of gravitational waves from a binary black hole merger. *Phys. Rev. Lett.*, 116:061102, Feb 2016.

[3] Brady P.R. Bailes M., Berger B.K. and others. Gravitational-wave physics and astronomy in the 2020s and 2030s. **Nat Rev Phys**, 3:344–366, 2021.

[4] Éanna É Flanagan and Scott A Hughes. The basics of gravitational wave theory. *New Journal of Physics*, 7(1):204, sep 2005.

[5] Peter R Saulson. *Fundamentals of interferometric gravitational wave detectors*. World Scientific, 1994.

[6] Andrzej Krolak and Mandar Patil. The first detection of gravitational waves. *Universe*, 3:59, July 2017.

[7] Peter Aufmuth and Karsten Danzmann. Gravitational wave detectors. *New Journal of Physics*, 7(1):202, sep 2005.

[8] LIGO Scientific Collaboration. https://www.ligo.org/science/GW-Sources.php.

[9] J. Weber. Evidence for discovery of gravitational radiation. *Phys. Rev. Lett.*, 22:1320–1324, Jun 1969.

[10] M. E. Gertsenshtein and V. I. Pustovoit. On the Detection of Low Frequency Gravitational Waves. *Sov. Phys. JETP*, 16:433, 1962.

[11] K. Danzmann. Laser interferometric gravitational wave detectors. In *13th Conference on General Relativity and Gravitation (GR-13)*, pages 3–19, 1993.

[12] D. Buskulic and I. Mandel. LIGO and Virgo Gravitational-wave Detectors and Their Science Reach. *Acta Phys. Polon. B*, 44(12):2413–2446, 2013.

[13] LIGO Scientific Collaboration. Advanced LIGO. *Classical and quantum gravity*, 32(7):074001, 2015.

[14] LIGO Lab. https://www.ligo.caltech.edu/.

[15] Duncan Ross Lorimer and Michael Kramer. *Handbook of pulsar astronomy*, volume 4. Cambridge university press, 2005.

[16] Verbiest et al. The International Pulsar Timing Array: First data release. *Monthly Notices of the Royal Astronomical Society*, 458(2):1267–1288, 02 2016.

[17] Kevork N. Abazajian et al. Cmb-s4 science book, first edition, 2016.

[18] Li Hong et al. Probing primordial gravitational waves: Ali CMB Polarization Telescope. *National Science Review*, 6(1):145–154, 02 2018.

[19] Keck Array and BICEP2 Collaborations. Constraints on primordial gravitational waves using *planck*, wmap, and new bicep2/*keck* observations through the 2015 season. *Phys. Rev. Lett.*, 121:221301, Nov 2018.

[20] A M Cruise. An electromagnetic detector for very-high-frequency gravitational waves. *Classical and Quantum Gravity*, 17(13):2525, jul 2000.

[21] Maxim Goryachev and Michael E. Tobar. Gravitational wave detection with high frequency phonon trapping acoustic cavities. *Phys. Rev. D*, 90:102005, Nov 2014.

[22] L. P. Grishchuk. Electromagnetic generators and detectors of gravitational waves, 2003.

[23] Fang Zhen-Yun Li Fang-Yu, Wen Hao. High-frequency gravitational waves having large spectral densities and their electromagnetic response. *Chin. Phys. B*, 22(12):10402, 2013.

[24] Hulse R.A and Taylor J.H. Discovery of a pulsar in a binary system. *Astrophysical Journal*, 195:L51–L53, January 1975.

[25] LIGO Scientific Collaboration and Virgo Collaboration. Gw170817: Observation of gravitational waves from a binary neutron star inspiral. *Phys. Rev. Lett.*, 119:161101, Oct 2017.

[26] The LIGO Scientific Collaboration and the Virgo Collaboration. A gravitational-wave measurement of the hubble constant following the second observing run of advanced ligo and virgo. *The Astrophysical Journal*, 909(2):218, mar 2021.

[27] BP Abbott, R Abbott, TD Abbott, et al. Ligo scientific and virgo and 1m2h and dark energy camera gw-e and des and dlt40 and las cumbres observatory and vinrouge and master collaborations. *Nature*, 551(7678):85, 2017.

[28] The LIGO Scientific Collaboration, the Virgo Collaboration, and the KAGRA Collaboration. Gwtc-3: Compact binary coalescences observed by ligo and virgo during the second part of the third observing run, 2021.

[29] Clemente Smarra et al. The second data release from the european pulsar timing array: Vi. challenging the ultralight dark matter paradigm, 2023.

[30] Daniel J. Reardon et al. The gravitational-wave background null hypothesis: Characterizing noise in millisecond pulsar arrival times with the parkes pulsar timing array. *The Astrophysical Journal Letters*, 951(1):L7, jun 2023.

[31] Heng Xu et al. Searching for the nano-hertz stochastic gravitational wave background with the chinese pulsar timing array data release i. *Research in Astronomy and Astrophysics*, 23(7):075024, jun 2023.

[32] The NANOGrav Collaboration. The nanograv 15 yr data set: Evidence for a gravitational-wave background. *The Astrophysical Journal Letters*, 951(1):L8, jun 2023.

[33] F Acernese, M Agathos, K Agatsuma, D Aisa, N Allemandou, A Allocca, J Amarni, P Astone, G Balestri, G Ballardin, et al. Advanced Virgo: a second-generation interferometric gravitational wave detector. *Classical and Quantum Gravity*, 32(2):024001, Dec 2014.

[34] Kentaro Somiya et al. Detector configuration of KAGRA–the Japanese cryogenic gravitational-wave detector. *Classical and Quantum Gravity*, 29(12):124007, jun 2012.

[35] B Willke et al. The geo 600 gravitational wave detector. *Classical and Quantum Gravity*, 19(7):1377, mar 2002.

[36] C. S. UNNIKRISHNAN. IndIGO AND LIGO-INDIA: SCOPE AND PLANS FOR GRAVITATIONAL WAVE RESEARCH AND PRECISION METROLOGY IN INDIA. *International Journal of Modern Physics D*, 22(01):1341010, jan 2013.

[37] Eric Chassande-Mottin, LIGO Scientific Collaboration, and Virgo Collaboration. Data analysis challenges in transient gravitational-wave astronomy. In *AIP Conference Proceedings*. AIP, 2013.

[38] Einstein telescope web page. http://www.et-gw.eu/.

[39] Lisa web page. http://www.gravity.uwa.edu.au/.

[40] Naoki Seto, Seiji Kawamura, and Takashi Nakamura. Possibility of direct measurement of the acceleration of the universe using 0.1 hz band laser interferometer gravitational wave antenna in space. *Phys. Rev. Lett.*, 87:221103, Nov 2001.

[41] Wen-Rui Hu and Yue-Liang Wu. The Taiji program in space for gravitational wave physics and the nature of gravity. *National Science Review*, 4(5):685–686, 10 2017.

[42] Jun Luo et al. TianQin: a space-borne gravitational wave detector. *Classical and Quantum Gravity*, 33(3):035010, jan 2016.

[43] C J Moore, R H Cole, and C P L Berry. Gravitational-wave sensitivity curves. *Classical and Quantum Gravity*, 32(1):015014, dec 2014.

[44] Jean-Michel Courty, Antoine Heidmann, and Michel Pinard. Quantum locking of mirrors in interferometers. *Phys. Rev. Lett.*, 90:083601, Feb 2003.

[45] Carlton M. Caves. Quantum-mechanical radiation-pressure fluctuations in an interferometer. *Phys. Rev. Lett.*, 45:75–79, Jul 1980.

[46] Savas Dimopoulos, Peter W. Graham, Jason M. Hogan, Mark A. Kasevich, and Surjeet Rajendran. Gravitational wave detection with atom interferometry. *Physics Letters B*, 678(1):37–40, 2009.

[47] Savas Dimopoulos, Peter W. Graham, Jason M. Hogan, Mark A. Kasevich, and Surjeet Rajendran. Atomic gravitational wave interferometric sensor. *Phys. Rev. D*, 78:122002, Dec 2008.

[48] Masaki Ando, Koji Ishidoshiro, Kazuhiro Yamamoto, Kent Yagi, Wataru Kokuyama, Kimio Tsubono, and Akiteru Takamori. Torsion-bar antenna for low-frequency gravitational-wave observations. *Phys. Rev. Lett.*, 105:161101, Oct 2010.

[49] Seiji Kawamura and Yanbei Chen. Displacement-noise-free gravitational-wave detection. *Phys. Rev. Lett.*, 93:211103, Nov 2004.

[50] Yanbei Chen and Seiji Kawamura. Displacement- and timing-noise-free gravitational-wave detection. *Phys. Rev. Lett.*, 96:231102, Jun 2006.

[51] Atsushi Nishizawa, Shoki Iwaguchi, Yanbei Chen, Taigen Morimoto, Tomohiro Ishikawa, Bin Wu, Izumi Watanabe, Yuki Kawasaki, Ryuma Shimizu, Hirohiko Shimizu, Masaaki Kitaguchi, Yuta Michimura, and Seiji Kawamura. Neutron displacement noise-free interferometer for gravitational-wave detection. *Phys. Rev. D*, 105:124017, Jun 2022.

[52] D Friedrich, M Nakano, H Kawamura, Y Yamanaka, S Hirobayashi, and S Kawamura. Juggled interferometer for the detection of gravitational waves around 0.1–10 hz. *Classical and Quantum Gravity*, 31(24):245006, nov 2014.

[53] M Punturo et al. The third generation of gravitational wave observatories and their science reach. *Classical and Quantum Gravity*, 27(8):084007, apr 2010.

[54] Hild S and others. Sensitivity studies for third-generation gravitational wave observatories. *Classical and Quantum Gravity*, 28(9):094013, apr 2011.

[55] Benjamin J. Owen and B. S. Sathyaprakash. Matched filtering of gravitational waves from inspiraling compact binaries: Computational cost and template placement. *Physical Review D*, 60(2), jun 1999.

[56] Eric D. Black. An introduction to Pound–Drever–Hall laser frequency stabilization. *American Journal of Physics*, 69(1):79–87, 2001.

[57] John Miller, Matthew Evans, Lisa Barsotti, Peter Fritschel, Myron MacInnis, Richard Mittleman, Brett Shapiro, Jonathan Soto, and Calum Torrie. Damping parametric instabilities in future gravitational wave detectors by means of electrostatic actuators. *Physics Letters A*, 375(3):788–794, Jan 2011.

[58] Takashi Usuda, Marek Dobosz, and Tomizo Kurosawa. Evaluation method for frequency characteristics of linear actuators in the sub-m stroke range using a modified michelson-type interferometer. *Nanotechnology*, 9(2):77–84, jun 1998.

[59] Bin Wu, Tomohiro Ishikawa, Shoki Iwaguchi, Ryuma Shimizu, Izumi Watanabe, Yuki Kawasaki, Yuta Michimura, Shuichiro Yokoyama, and Seiji Kawamura. Conceptual design and science cases of a juggled interferometer for gravitational wave detection. *Phys. Rev. D*, 106:042007, Aug 2022.

[60] Kostas D Kokkotas and Bernd G Schmidt. Quasi-normal modes of stars and black holes. *Living Reviews in Relativity*, 2, sep 1999.

[61] Olaf Dreyer, Bernard Kelly, Badri Krishnan, Lee Samuel Finn, David Garrison, and Ramon Lopez-Aleman. Black-hole spectroscopy: testing general relativity through gravitational-wave observations. *Classical and Quantum Gravity*, 21(4):787–803, jan 2004.

[62] Emanuele Berti, Vitor Cardoso, and Andrei O Starinets. Quasinormal modes of black holes and black branes. *Classical and Quantum Gravity*, 26(16):163001, Jul 2009.

[63] Fernando Echeverria. Gravitational-wave measurements of the mass and angular momentum of a black hole. *Phys. Rev. D*, 40:3194–3203, Nov 1989.

[64] Chiara M. F. Mingarelli, Stephen R. Taylor, B. S. Sathyaprakash, and Will M. Farr. Understanding $\omega_{\rm gw}(f)$ in gravitational wave experiments, 2019.

[65] LIGO Scientific Collaboration. LIGO Algorithm Library - LALSuite. free software (GPL), 2018.

[66] C. Brans and R. H. Dicke. Mach's principle and a relativistic theory of gravitation. *Phys. Rev.*, 124:925–935, Nov 1961.

[67] Kent Yagi and Takahiro Tanaka. DECIGO/BBO as a Probe to Constrain Alternative Theories of Gravity. *Progress of Theoretical Physics*, 123(6):1069–1078, 06 2010.

[68] Kent Yagi and Takahiro Tanaka. Constraining alternative theories of gravity by gravitational waves from precessing eccentric compact binaries with lisa. *Phys. Rev. D*, 81:064008, Mar 2010.

[69] Curt Cutler and Jan Harms. Big Bang Observer and the neutron-star-binary subtraction problem. *Phys. Rev. D*, 73:042001, Feb 2006.

[70] L. Iess B. Bertotti and P. Tortora. A test of general relativity using radio links with the Cassini spacecraft. *Nature*, 425(374), 2003.

[71] Xing Zhang, Jiming Yu, Tan Liu, Wen Zhao, and Anzhong Wang. Testing brans-dicke gravity using the einstein telescope. *Phys. Rev. D*, 95:124008, Jun 2017.

[72] B. J. Carr and S. W. Hawking. Black Holes in the Early Universe. *Monthly Notices of the Royal Astronomical Society*, 168(2):399–415, 08 1974.

[73] Stephen Hawking. Gravitationally Collapsed Objects of Very Low Mass. *Monthly Notices of the Royal Astronomical Society*, 152(1):75–78, 04 1971.

[74] A. D. Dolgov. Massive primordial black holes, 2019.

[75] Bernard Carr, Kazunori Kohri, Yuuiti Sendouda, and Jun'ichi Yokoyama. Constraints on primordial black holes. *Reports on Progress in Physics*, 84(11):116902, nov 2021.

[76] Juan Garcí a-Bellido. Massive primordial black holes as dark matter and their detection with gravitational waves. *Journal of Physics: Conference Series*, 840:012032, may 2017.

[77] Harry Poulter, Yacine Ali-Haïmoud, Jan Hamann, Martin White, and Anthony G. Williams. CMB constraints on ultra-light primordial black holes with extended mass distributions. 7 2019.

[78] Hiroko Niikura et al. Microlensing constraints on primordial black holes with Subaru/HSC Andromeda observations. *Nature Astron.*, 3(6):524–534, 2019.

[79] Ryo Saito and Jun'ichi Yokoyama. Gravitational-wave background as a probe of the primordial black-hole abundance. *Phys. Rev. Lett.*, 102:161101, Apr 2009.

[80] Kazunori Kohri and Takahiro Terada. Semianalytic calculation of gravitational wave spectrum nonlinearly induced from primordial curvature perturbations. *Phys. Rev. D*, 97:123532, Jun 2018.

[81] Rika Yamada, Yutaro Enomoto, Atsushi Nishizawa, Koji Nagano, Sachiko Kuroyanagi, Keiko Kokeyama, Kentaro Komori, Yuta Michimura, Takeo Naito, Izumi Watanabe, Taigen Morimoto, Masaki Ando, Akira Furusawa, and Seiji Kawamura. Optimization of quantum noise by completing the square of multiple interferometer outputs in quantum locking for gravitational wave detectors. *Physics Letters A*, 384(26):126626, 2020.

[82] Nikkidenso. https://www.nikkidenso.co.jp.